

---

# Advances in GPS based Time and Frequency Comparisons for Metrological Use

---

Von der Fakultät für Mathematik und Physik der  
Gottfried Wilhelm Leibniz Universität Hannover

zur Erlangung des Grades

Doktor der Naturwissenschaften  
Dr. rer. nat.

genehmigte Dissertation

von

Dipl.-Phys. Thorsten Feldmann  
geboren am 11. Juli 1977 in Duisburg

2011

Referent: PD Dr. Ekkehard Peik  
Korreferent: Prof. Dr. -Ing. Steffen Schön  
Tag der Promotion: 29.06.2011

# Abstract

The global satellite navigation system GPS is the main tool for remote time and frequency comparisons of atomic timescales and oscillators. The comparisons are realized by referring the local timescales at both sites to the atomic clocks in the satellites or to a common reference time by measuring a binary code transmitted by the satellites and exchanging the data afterwards. Besides measuring the code modern GPS receivers are also capable to track the phase of the carrier frequency, but with an unknown initial number of cycles of this frequency between receiver and satellites. By combining these carrier-phase measurements with the code measurements and correction data calculated from a worldwide network of reference stations, the positions and the time offsets of the receivers can be estimated with high accuracy within a process called Precise Point Positioning (PPP).

The main issues of this work are to provide a highly precise frequency at any location, which can be used for other scientific applications, and the precise calibration of operational time links. In this context, the mathematical models and the GPS receiver hardware are examined in detail from the viewpoint of time and frequency comparisons.

Based on a passive hydrogen maser and a state-of-the-art time and frequency transfer receiver a highly precise mobile frequency reference was realized at PTB. It was carried to the Institute of Quantum Optics (IQO) at the Leibniz Universität Hannover (LUH) and is used as the reference source in the framework of developing optical clocks. The evaluation of the performance of the passive maser at PTB and at LUH is shown. Due to PPP the maser located at LUH can be referenced to PTB's primary standards at an averaging time of  $10^4$  s with the help of PPP at a relative frequency instability of better than  $10^{-14}$ .

GPS time and frequency comparison is a one-way technique, since signals are only transmitted by the satellites and received on the ground. Thus, physical influences occurring along the signal path and relativistic effects on the satellite clocks have to be corrected by mathematical models. Different PPP software packages are analyzed in view of all parameters which have to be estimated. The influence of the models is studied in detail by using only the carrier-phase measurement on baselines with different lengths. This is possible, if the ambiguous carrier-phase measurement does not deviate too much from the code measurement.

Subsequently, different receivers are analyzed in view of long and short term stability. The requirements on the equipment for time and frequency transfer are outlined and new concepts for improvements are proposed. The first GPS

common-clock measurement between the remote sites PTB and IQO is shown. The local clocks at PTB and IQO are canceled out by comparing the GPS data to the measurements using an optical fiber which is operated for frequency transfer between these institutes.

Finally, calibrations of operational GPS links used by the International Bureau for Weights and Measures (BIPM) for the realization of the international atomic time scale (TAI) by means of a traveling GPS receiver are demonstrated. An uncertainty at the level of 1 ns was achieved thanks to employing a state-of-the-art receiver. Based on such a receiver and a time interval counter a new setup for link calibration was realized at PTB, which further reduces the uncertainty.

**Keywords:** Time Comparisons, Frequency Comparisons, GPS

# Zusammenfassung

Das globale Satellitennavigationssystem GPS ist das wichtigste Instrument zum Vergleich entfernter atomarer Zeitskalen und Oszillatoren. Der Vergleich wird realisiert durch die Referenzierung der lokalen Zeitskalen auf beiden Seiten zu den Atomuhren in den Satelliten oder zu einer gemeinsamen Referenzzeit, indem ein von den Satelliten ausgesendeter binärer Code gemessen wird und die Messdaten anschließend ausgetauscht werden. Neben der Codemessung können moderne GPS-Empfänger auch die Trägerphase nachverfolgen, allerdings ohne die anfängliche Zahl der Zyklen dieser Phase zwischen Satelliten und Empfänger zu kennen. Indem diese Trägerphasenmessung mit der Codemessung und Korrekturdaten eines weltweiten Netzwerkes von Referenzstationen kombiniert wird, können die Positionen und die Zeitbasis der Empfänger mit hoher Genauigkeit bestimmt werden. Dieser Prozess wird "Precise Point Positioning" (PPP) genannt.

Die Hauptfragestellungen dieser Arbeit sind die Bereitstellung einer hochpräzisen Frequenz an jedem beliebigen Ort, die für Forschungszwecke genutzt werden kann, sowie die präzise Kalibrierung von Zeitverbindungen. In diesem Zusammenhang werden auch die mathematischen Modelle und die GPS Empfänger vom Standpunkt der Zeit- und Frequenzvergleiche her analysiert.

Aufbauend auf einem passiven Wasserstoffmaser und einem modernen Zeit- und Frequenzempfänger wurde an der PTB eine hochpräzise transportable Frequenzreferenz realisiert. Diese wurde zum Institut für Quantenoptik (IQO) an der Leibniz Universität Hannover (LUH) gebracht und dient dort als Referenz bei der Entwicklung optischer Uhren. Die Ermittlung der Betriebseigenschaften des passiven Masers an der PTB und an der LUH wird gezeigt. Mit Hilfe des PPP-Verfahrens kann der Maser an der LUH mit einer Mittelungszeit von  $10^4$  s an die primären Frequenznormale der PTB angebunden werden.

GPS Zeit- und Frequenzvergleiche sind eine Einwegtechnik, da Signale nur von den Satelliten ausgesendet werden und am Boden empfangen werden. Daher müssen physikalische Einflüsse auf den Signalweg und relativistische Effekte auf die Satellitenuhren durch mathematische Modelle korrigiert werden. Verschiedene PPP-Softwarepakete werden im Hinblick auf alle zu bestimmenden Parameter untersucht. Der Einfluss der Modelle wird detailliert untersucht, indem nur die Trägerphasenmessung auf Basislinien verschiedener Länge benutzt wird. Dies ist möglich, wenn die mehrdeutige Trägerphasenmessung nicht zu sehr von der Codemessung abweicht.

Anschließend werden verschiedene Empfänger im Hinblick auf Kurz- und Langzeitstabilität untersucht. Die Anforderungen an die Geräte im Rahmen von Zeit- und Frequenzvergleichen werden deutlich gemacht und neue Konzepte zur Verbesserung werden vorgeschlagen. Das erste GPS-Experiment mit gemeinsamer Referenz zwischen den entfernten Orten PTB und LUH wird vorgestellt. Die Einflüsse der lokalen Uhren an der PTB und an der LUH werden durch den Vergleich der GPS-Daten mit den Messungen einer optischen Faser, die zur Frequenzübertragung zwischen diesen Instituten dient, beseitigt.

Schlussendlich wird die Kalibrierung von GPS Verbindungen, die vom internationalen Büro für Maß und Gewicht zur Realisierung der internationalen Atomzeit TAI ausgewertet werden, mithilfe eines reisenden GPS Empfängers gezeigt. Durch die Verwendung eines modernen Empfängers liegt die Unsicherheit im Bereich von 1 ns. Basierend auf einem solchen Empfänger und einem Zeitintervallzähler wurde an der PTB ein neuartiger Aufbau entwickelt, mit dem die Unsicherheit weiter reduziert werden kann.

**Stichworte:** Zeitvergleiche, Frequenzvergleiche, GPS

# Contents

List of Acronyms . . . . .	vii
<b>1. Introduction</b>	<b>1</b>
<b>2. State-of-the-Art in remote Time and Frequency Comparisons</b>	<b>5</b>
2.1. Characterization of Frequency Instabilities . . . . .	5
2.2. Today's remote Time and Frequency Comparison Methods . . . . .	7
2.3. GPS and Time and Frequency Transfer . . . . .	8
2.3.1. Brief GPS System Overview . . . . .	9
2.3.2. Coordinate Systems and Satellite Motion . . . . .	13
2.3.3. Observation Model . . . . .	14
2.3.4. Time and Frequency Transfer Receivers . . . . .	15
2.4. Signal Delays and Correction Models . . . . .	20
2.4.1. Atmospherical Corrections . . . . .	20
2.4.2. Relativistic Corrections . . . . .	22
2.4.3. Multipath . . . . .	23
2.4.4. Site Displacement . . . . .	24
2.4.5. Other Delay Sources . . . . .	25
2.5. The International GNSS Service (IGS) . . . . .	25
2.6. Precise Point Positioning . . . . .	29
2.7. GPS and UTC Generation . . . . .	31
<b>3. A Highly Precise Mobile Frequency Reference</b>	<b>34</b>
3.1. Motivation . . . . .	34
3.2. Equipment . . . . .	34
3.3. Performance of the passive Hydrogen Maser . . . . .	36
3.4. Performance of the GTR50 Time and Frequency Transfer Receiver .	39
3.5. Installation of the Frequency Reference at the IQO . . . . .	40
<b>4. Software Assessment</b>	<b>44</b>
4.1. Common-Clock quasi zero Baseline Experiments . . . . .	44
4.2. Discontinuous measurement data and drifts . . . . .	47
4.3. Clock comparisons and PPP parameters . . . . .	49
4.3.1. Software and Experimental Setup . . . . .	49
4.3.2. Time Scale Comparisons . . . . .	52

4.3.3.	Position Estimates . . . . .	54
4.3.4.	Troposphere Zenith Path Delay Estimates . . . . .	56
4.4.	Code free Carrier-Phase Frequency Comparisons . . . . .	58
4.4.1.	Description of the Method . . . . .	59
4.4.2.	Application to different Baselines . . . . .	62
<b>5.</b>	<b>Hardware Experiments</b>	<b>67</b>
5.1.	Performance of Receivers . . . . .	67
5.1.1.	Instability of Time and Frequency Receivers . . . . .	68
5.1.2.	QUEST Experimental Receivers . . . . .	70
5.1.3.	Temperature Sensitivity . . . . .	72
5.2.	Suggestions for Improvements in Frequency Transfer . . . . .	73
5.2.1.	Phase Comparator Measurements . . . . .	73
5.2.2.	Stabilization of Cables . . . . .	74
5.3.	The first Long Baseline Common-Clock Experiment . . . . .	76
<b>6.</b>	<b>Relative Calibration of TAI links</b>	<b>80</b>
6.1.	Motivation . . . . .	80
6.2.	Description of the Calibration Procedure . . . . .	81
6.2.1.	CV versus AV . . . . .	83
6.2.2.	Code Based Time Transfer and Position Errors . . . . .	86
6.2.3.	PPP and Antenna Phase Center Corrections . . . . .	88
6.2.4.	Data Processing . . . . .	89
6.3.	Uncertainty Estimation . . . . .	90
6.4.	PTB's Calibration Set-up . . . . .	95
6.5.	METAS-PTB Calibration . . . . .	98
6.6.	USNO-PTB Calibration . . . . .	107
6.7.	Suggestions for further Reductions of the Uncertainty . . . . .	115
<b>7.</b>	<b>Summary and Outlook</b>	<b>117</b>
<b>Appendix</b>		<b>119</b>
A.	Mathematical Description of the Coordinate Systems . . . . .	119
B.	Mathematical Description of the Satellite Motion . . . . .	121
C.	CGGTTS Data . . . . .	123
D.	RINEX Data . . . . .	124
E.	P3 linear combination . . . . .	125
F.	Brief Derivation of Relativistic Corrections . . . . .	127
G.	Estimation of the Ephemerides of Sun and Moon . . . . .	129
H.	BIPM's Circular T . . . . .	132
<b>Bibliography</b>		<b>134</b>



# List of Acronyms

<b>1 PPS</b>	one pulse per second signal
<b>ADEV</b>	Allan Deviation
<b>AV</b>	all-in-view
<b>BIPM</b>	Bureau international des poids et mesures
<b>C/A-code</b>	coarse/aquisition code
<b>CCD</b>	common-clock difference
<b>CCTF</b>	Consultative Committee for Time and Frequency
<b>CGGTTS</b>	CCTF Working Group on GPS and GLONASS Time Transfer Standards
<b>CV</b>	common-view
<b>dCCD</b>	difference between two CCDs
<b>DMTD</b>	dual mixer time difference technique
<b>FR</b>	fixed receiver
<b>GLONASS</b>	Global Navigation Satellite System, Russian GNSS system
<b>GNSS</b>	Global Navigation Satellite System
<b>GPS</b>	Global Positioning System, US GNSS system
<b>IERS</b>	International Earth Rotation and Reference Systems Service
<b>IfE</b>	Institut für Erdmessung, geodetic institute at the LUH
<b>IGS</b>	International GNSS Service
<b>ITRF</b>	International Terrestrial Reference Frame
<b>IQO</b>	Institute of Quantum Optics at the LUH
<b>LUH</b>	Leibniz Universität Hannover
<b>METAS</b>	Swiss Federal Office of Metrology, operating the timescale UTC(CH)

<b>MDEV</b>	Modified Allan Deviation
<b>NICT</b>	Japanese National Institute of Information and Communications Technology, operating the timescale UTC(NICT)
<b>MJD</b>	Modified Julian Day
<b>NRCan</b>	Natural Resources Canada
<b>ODEV</b>	Overlapping Allen Deviation
<b>ORB</b>	Observatoire Royal de Belgique, operating the timescale UTC(ORB)
<b>P-code</b>	precision code
<b>PPP</b>	Precise Point Positioning
<b>PRN</b>	pseudorandom noise
<b>PTB</b>	Physikalisch-Technische Bundesanstalt, operating the timescale UTC(PTB)
<b>PZ-90</b>	Russian Earth parameter system 1990
<b>QUEST</b>	Centre for Quantum Engineering and Space-Time Research
<b>RINEX</b>	Receiver Independent Exchange Format
<b>ROA</b>	Real Instituto y Observatorio de la Armada, Spanish institute operating the timescale UTC(ROA)
<b>SD</b>	standard deviation
<b>TAI</b>	temps atomique international
<b>TDEV</b>	Time Deviation
<b>TR</b>	travelling receiver
<b>TIC</b>	time interval counter
<b>TWSTFT</b>	Two-Way Satellite Time and Frequency Transfer
<b>UFE</b>	Czech Institute of Photonics and Electronics, operating the timescale UTC(TP)
<b>USNO</b>	United States Naval Observatory, operating the timescale UTC(USNO)
<b>UTC</b>	Coordinated Universal Time
<b>WGS84</b>	World Geodetic System 1984

# 1. Introduction

Precise time and frequency are of paramount importance in technology and science [1, 2]. Typical technical applications for accurate and/or stable frequencies are for instance the steering of electrical power grids and modern digital telecommunication networks [3]. Accurate timing is for instance the basis of navigation using Global Navigation Satellite Systems (GNSS), like the US Global Positioning System (GPS) [4, 5]. Also industrial processes have to be steered with high precision and accuracy. In science the applications range from test of general relativity and Earth science to atomic spectroscopy and elementary particle physics. Furthermore, for many activities in the modern society an authoritative time reference is mandatory.

The unit of time, the second, is a fundamental unit of the international system of units (SI) [2, 6]. Since the unit of length, the meter, is defined via the velocity of light, it is also derived from a precise frequency.

In order to establish reliable standards, many countries in the world maintain a national time and frequency laboratory where atomic clocks serve as the national standards. Such a laboratory is PTB. The dissemination of legal time and of the unit of time and frequency is one of the prominent tasks of PTB. The transmission of standard frequency (77.5 kHz) and coded time informations is the most popular service of PTB [7].

An atomic clock uses an atomic transition to lock an electronic oscillator to it. The output frequency is mostly 10 MHz or 5 MHz and is shared in the laboratory by a distribution system. Special electronic generators undertake the task of counting the frequency zero crossings and generate a pulse signal with fast rising time every second (1 PPS signal).

Different types of clocks with different levels of accuracy are available commercially and primary frequency standards based on caesium are developed by the time laboratories [1, 2, 8].

The atomic clocks are compared locally with each other. These comparisons can either be done with frequency comparators using the dual mixer time difference (DMTD) technique [9] or with time interval counters (TICs) which measure the difference between two 1 PPS signals by counting the accumulated phase of a reference frequency. The latter technique is less precise due to a higher noise level induced by the electronics, but each pulse can be unambiguously related to a certain event.

Additionally, the timescales of the national time and frequency laboratories are compared with each other. The combination of local and remote comparisons enables the intercomparison of all atomic clocks and the generation of a world-wide reference timescale, the Coordinated Universal Time (UTC). The UTC calculation is done by the Bureau international des poids et mesures (BIPM) in France. The UTC is published on a five day basis as UTC-UTC(k) in the Circular T [2, 10]. Here "k" stands for the different time laboratories. Details are given in Section 2.7.

In the early days of atomic time and frequency comparisons the standards of the time and frequency laboratories were compared by using portable caesium clocks [11] since no adequate transmission technology was available. With the advances in the technology two methods for remote comparisons were available. One of these methods made use of the signals of the Long Range Navigation (LORAN) system, an Earth based system originally developed for navigation at sea consisting of long wave radio station chains along coastlines transmitting pulse series steered to atomic clocks [12]. The second method used the synchronization signals of the color subcarrier of a television signal [13]. Today, remote time and frequency comparisons are mainly done by using satellites [14].

Two complementary methods for satellite based remote time and frequency comparisons exist. The so-called Two-Way Satellite Time and Frequency Transfer (TWSTFT) utilizing geostationary telecommunication satellites, and the comparisons using the signals of the satellites of a GNSS system. TWSTFT is a point to point technique, since both sites are receiving as well as transmitting a signal. In contrast, the GNSS technique is a one-way method. In principle an unlimited number of sites everywhere on Earth can receive the satellites' signals and compare their local times and frequency to it. The comparison between the remote labs is established only by the exchange of the measurement data. However, corrections to the measurement data are necessary since propagation effects do not cancel out in this one-way technique. A short overview is given in Section 2.2.

The main issues of this work are to provide a highly precise frequency at any location, which can be used for other scientific applications, and the precise calibration of operational time links. In this context, the mathematical models needed in the framework of GPS and the GPS receiver hardware are examined in detail from the viewpoint of time and frequency comparisons.

The usage of the signals of a GNSS system, namely of GPS, is the main tool for time and frequency comparisons. The functionality and the current status of this technique is outlined in Section 2.3.

After the overview of the current status of the remote time and frequency comparisons with GNSS systems this work comprises of four main parts. The first is the description and evaluation of a new mobile frequency reference, which allows to provide a highly stable frequency at any desired location by making use of the GPS technology. Then data analysis methods for high precision GPS time and frequency comparisons and mathematical correction models are studied in detail.

---

After this the hardware for GPS based time and frequency comparisons is examined. Finally the calibration of operational time links by means of GPS, including a new hardware concept for the reduction of the uncertainty, is demonstrated on two examples. In the following some more details on these chapters is given.

As mentioned above, GPS allows comparing frequency standards at every location on the Earth. In this context, a mobile frequency reference consisting of a passive hydrogen maser (an atomic clock producing a stable frequency in the short term) and a state-of-the-art GPS receiver was developed. Thus, a frequency which is referenced to PTB's primary standards can be provided at any location and be used for scientific applications requiring highest accuracy and stability. This mobile frequency reference is currently operated at the Institute of Quantum Optics (IQO) at the Leibniz University Hanover (LUH) as part of the involvement in the Center for Quantum Engineering and Space-Time Research (QUEST). The experimental setup, local test of the equipment, and results of the measurements between Hanover and PTB are subject of Chapter 3.

The usual GPS observable is the measurement of the signal transmission time between satellite and receiver based on a binary code emitted by the satellites. The accuracy of these measurements is limited by the chip rate of the code. However, modern receivers can also measure the microwave carrier frequency of this transmission with high accuracy. A combination of the code and the carrier frequency measurement is used within an analysis strategy called Precise Point Positioning (PPP) [15]. PPP was used to evaluate the data of the mobile frequency reference in order to obtain frequency differences between the remote clocks at PTB and LUH with superior accuracy.

The PPP method was originally developed for geodetic science in order to determine a position with sub-centimeter accuracy. It is a post-processing approach, where correction data calculated from networks of globally distributed GPS receivers are combined with the measurement data. Different software concepts exist which use different solution algorithms and different correction models. Several of these software packages were evaluated with regard to all relevant parameters and their capabilities for time and frequency comparison were tested. The results are outlined in Chapter 4. In Section 4.4 a simple algorithm for frequency comparisons, which uses only the carrier-phase observable, is demonstrated and compared to the PPP method.

For highly accurate and stable frequency comparisons not only the data analysis strategy is important, but also the involved hardware. In Chapter 5 different GPS receivers are used to assess their capability for remote frequency comparisons. Some of these receivers were provided by and operated in cooperation with the IQO and Institut für Erdmessung (IfE) at the LUH. To characterize time and frequency transfer GPS receivers, two or more devices are usually connected to the same time and frequency source (common-clock setup) and the antennas are installed

nearby each other, such that error influences originating from the GPS signal path are minimized (short baseline).

By using an optical fiber, which was operated between PTB and the IQO in the framework of QUEST, it was possible to obtain frequency differences between the two remote clocks with an accuracy superior to any GNSS measurement [16] and the influence of the remote clocks could be eliminated. The results of this first common-clock long baseline experiment are shown in Section 5.3.

In contrast to pure frequency comparisons, in the framework of time and timescale comparisons it is necessary to relate distinct events with each other, in other words, to compare 1 PPS signals. Hence it is important to have a knowledge about the internal delays of the time transfer equipment involved in such comparisons. For the evaluation of the links used for the UTC generation by the BIPM, this knowledge is mandatory. This requires the calibration of the equipment or of the complete link. Recently, with the use of new GPS receivers, an uncertainty of less than 2 ns for a relative link calibration between the Royal Spanish Naval Observatory (Real Instituto y Observatorio de la Armada, ROA) and PTB performed in 2008 has been reported [17]. The further reduction of the uncertainty due to a revised concept including hardware improvements developed in the context of this work is demonstrated in Chapter 6.

## 2. State-of-the-Art in remote Time and Frequency Comparisons

Before the techniques for remote time and frequency comparisons and the GPS system are explained, a few words on the analysis of the instabilities of clocks and time and frequency links are necessary. Subsequently the different techniques for remote time and frequency comparisons are briefly introduced. Then the functionality of the GPS system as the primary tool for time and frequency comparisons is described. Recent techniques to improve the performance are outlined. Finally, the importance of GPS time comparisons in UTC generation by the BIPM and the need for accurate calibration of the time links involved is explained.

### 2.1. Characterization of Frequency Instabilities

Variances over samples of frequency data are used to characterize the instability. Very often it is not appropriate to use the common standard deviation (SD) for this task, because it is non-convergent for some noise types found in frequency measurements [18,19]. A better approach is to use the so-called Allan Deviation (ADEV) or two-sample variance [20]. It is defined as

$$\sigma_y^2(\tau) = \frac{1}{2(M-1)} \sum_{i=1}^M (\bar{y}_{i+1}(\tau) - \bar{y}_i(\tau))^2, \quad (2.1)$$

where  $\bar{y}_i$  is the  $i$ th of  $M$  relative frequency averages, averaged over the sampling interval  $\tau$  from frequency data  $y(t)$  [19]. The smallest averaging value  $\tau_0$  can never be smaller than the spacing of the data. The frequency data can be calculated from phase data  $x(t)$  according to

$$y(t) = \frac{x(t) - x(t - \Delta t)}{\Delta t}, \quad (2.2)$$

where  $\Delta t$  is the spacing of the data.

The Allan variance is usually calculated for a few sampling intervals and then depicted in a double logarithmic plot. With the help of the slope of the data points

it is possible to distinguish between the noise types affecting the data. By applying theoretical statistical considerations, confidence intervals can be calculated, which appear as error bars in the plot [19].

In order to improve the confidence and the ability to distinguish between different noise types, more averaging processes have been introduced which led to the Overlapping Allan Deviation (ODEV) and the Modified Allan Deviation (MDEV). Details can be found in the references [18, 19]. Furthermore, to characterize the time error, the Time Deviation (TDEV), which is defined as  $(\tau/\sqrt{3})\text{MDEV}(\tau)$ , was invented. Table 2.1 shows the slopes of a double logarithmic plot corresponding to different noise types for ADEV, MDEV, and TDEV [18]. The TDEV is defined

**Table 2.1.:** The slope of the different deviations depending on the noise type. White frequency noise can also be denoted as random walk phase noise, random walk frequency is also known as white frequency aging.

Noise	ADEV	MDEV	TDEV
white phase	-1	-3/2	-1/2
flicker phase	-1	-1	0
white frequency	-1/2	-1/2	1/2
flicker frequency	0	0	1
random walk frequency	1/2	1/2	3/2

in a way that it is equal to the SD in the case of white phase noise. Only in this case the slope of the double logarithmic plot is negative. The minimum of the double logarithmic plot indicates the averaging interval at which this type of Gaussian distributed noise can be removed from the data without losing other relevant information.

Although the deviations are defined for evenly spaced data, they can also be used in the case of missing measurements if the data gap is not too big and  $\tau_0$  is replaced by an effective average value. Details are explained in the references [18, 19].

In the framework of time and frequency metrology it is typical that the timestamps of measurement data are related to the Modified Julian Day (MJD). It is a continuous numbering of the days starting at November 17, 1858. The January 1st, 2011 was MJD 55562.



## 2.2. Today's remote Time and Frequency Comparison Methods

The *TWSTFT method* is an active technique where respective ground stations are transmitting and receiving signals that are referenced to the local clock signals. The difference between the two clock signals can be calculated from the difference of the signal propagation delays (Figure 2.1) measured on both sites. This requires expensive and labor intensive ground installations.

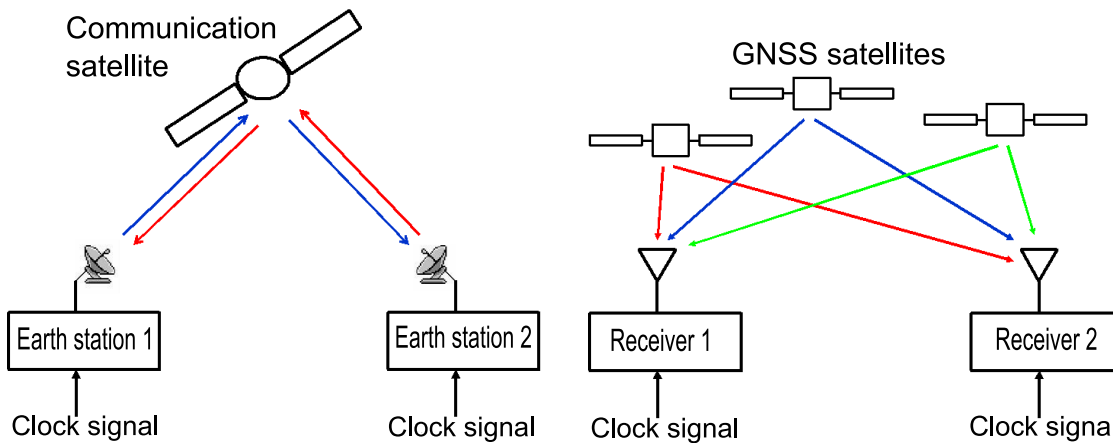


**Figure 2.1.:** TWSTFT (left) and GNSS time and frequency transfer (right).

In contrast, the Earth installations in the framework of *GNSS time and frequency transfer* are only consisting of receivers. Each GNSS satellite is transmitting signals which contain information about its position and the offset of its internal clock with respect to a common system time. Thus, each receiver can perform a signal propagation time measurement with respect to the satellite's clock or to the common system time, referenced to the local clock connected to the receiver. The link between the local clock signals at two sites is calculated afterwards by exchanging the measurement data. Thereby the satellite clocks cancel out.

A GNSS link can in principle either be evaluated in common-view (CV) or in all-in-view (AV) mode. CV means that first the difference between two receivers is calculated for each satellite seen by both receivers independently at each epoch and that the mean value is calculated afterwards. In the AV mode a solution is at first independently calculated for each receiver with respect to the GNSS system time including all tracked satellites, and differences are made based on the averages [21,22]. For a CV comparison in principle the signal of one single satellite is sufficient.

In Table 2.2 the typical operational distances of the different time and frequency link techniques are listed. Since the CV method requires that the satellites are

commonly visible at both sites the operational distance is limited, similar as for TWSTFT. Due to referencing each station to the common time reference in AV mode, clocks located at the opposite sites of the Earth can be compared, but noise of the GNSS system time is partially transferred to the time comparison results.

**Table 2.2.:** Typical operational distances of the different time and frequency comparison techniques.

Technique	Distance
GPS AV	20000 km
GPS CV	10000 km
TWSTFT	10000 km
Optical fiber	300 km

The advantage of the TWSTFT method is that signals are propagating simultaneously in both directions and errors due to the atmosphere of the Earth cancel out to the first order. However, GNSS time transfer is less cost and labor intensive, because only receiving equipment is needed. A GNSS receiver can in principle be operated everywhere on the Earth. There is no signal emission, just reception.

New methods of comparing two remote clocks by an optical signal that is sent through an optical fiber have recently been developed. Mainly experiments have been done to compare remote experimental optical frequency standards [16]. First experiments related to time transfer via optical fibers using a two-way technique have also been performed [23, 24]. However, time and frequency transfer using an optical fiber is a point-to-point technique, currently just applicable for short distance links, and a very expensive method compared to GPS.

### 2.3. GPS and Time and Frequency Transfer

Currently the US Global Positioning System (GPS) is the main tool used for time and frequency transfer between remote sites. A second system is operated by Russia and named Global Navigation Satellite System (GLONASS). Unfortunately the constellation was incomplete during many years and the usage was restricted to military users. Thus, this system did not become very popular and currently few receivers are on the market. Additional systems are planned, like the European Galileo system or the Chinese COMPASS, but these systems are currently all in the development phase.

In this work the focus is on the GPS system. Most statements made in this Section are in principle also valid for the GLONASS system, except some technical details.

### 2.3.1. Brief GPS System Overview

The nominal GPS system consists of a constellation of at least 24 satellites orbiting the Earth in 6 orbital planes. The orbits are approximately circular and equally spaced around the equator at a  $60^\circ$  separation with an inclination relative to the equator of  $55^\circ$ . The mean distance of a satellite to the center of mass of the Earth is about 26600 km [4]. Figure 2.2 gives an artist impression of the GPS satellite constellation, which is also called the space segment of the GPS system [4]. Due to this constellation, far in the north and in the south regions exist where the satellites are never visible in the zenith for an observer on the Earth. This is the so-called "north hole" or "south hole", respectively.

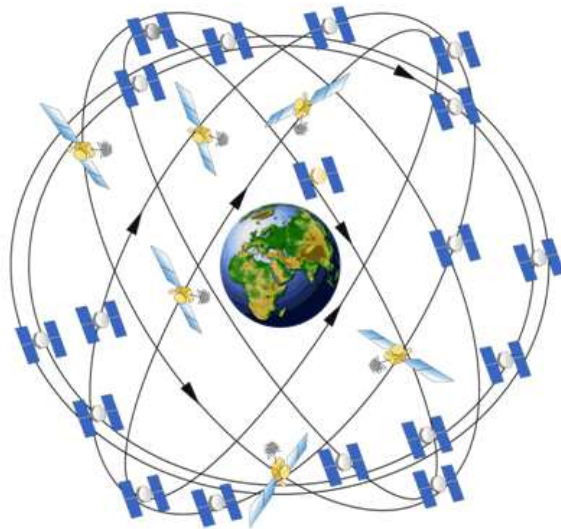


**Figure 2.2.:** The GPS satellite constellation. This image is by courtesy of the US government.

On board of each satellite atomic clocks are operated. The type of atomic clocks (caesium, rubidium) depends on the satellites within a specific production series. The nominal output frequency of the clocks is  $f_0 = 10.23$  MHz. From this fundamental frequency the two microwave frequencies  $f_1 = 1575.42$  MHz and  $f_2 = 1227.60$  MHz are derived by multiplying  $f_0$  by 154 and 120, respectively. These two frequencies are the carrier frequencies on the L1 and the L2 band. Since they are below 2 GHz no directional antenna is needed to receive the signal.

Before being transmitted by an antenna array the two carriers are phase modulated with pseudorandom noise codes, the so-called PRN-codes. These are binary codes with a chip rate of 1.032 MHz on the  $f_1$  frequency, named coarse/acquisition (C/A) code, and a binary code with 10.23 MHz chip rate on both frequencies, called precision (P) code. These codes are unique for each satellite, continuously repeated, and used for the identification and the tracking of the satellites by a

correlation process performed by a receiver. All satellites transmit their signals on the same frequencies. This technique is called Code Division Multiple Access (CDMA). To suppress cross-correlation between the PRN-codes, so-called Gold codes are used. Mathematical details and details on the signal generation are outlined in reference [4]. The term chip is used instead of bit, because these codes contain no additional data information. The modulation is a Bi-Phase Shift Key (BPSK) modulation [4].

An additional 50 bits per second binary code is superimposed to the PRN-codes by a binary addition modulo 2 (exclusive-or process). This code is called the navigation message and contains information about the status of the individual satellite as well as of the constellation as a whole, the satellites' positions (ephemeris data), the offset of the satellites' clocks with respect to a common reference timescale (the GPS system time), and information about the ionosphere [25].

The P-code and the C/A code signal are modulated to the carrier frequency in a way that there is a phase shift between the two codes of  $90^\circ$ . Due to the satellite antenna array the signals are right-handed circular polarized to suppress Faraday rotation in the ionosphere.

The satellites are controlled and monitored by the so-called ground segment, consisting of several monitor stations, a few uplink stations, and a master control station which is located at Schriever Air Force Base near Colorado Springs, USA. Here the satellite ephemerides are forecasted, the offset of the individual clocks with respect to the system time is calculated, and clock steering commands are sent to the satellites, if necessary. The system time is an ensemble timescale of all clocks in the satellites and the ground stations. It is kept in close agreement with the time scale of the United States Naval Observatory (USNO), UTC(USNO). Since there is more than one atomic clock in each satellite, the master control station also decides which clock is used for the signal generation depending on the clock performance.

All systems which are capable of receiving the GPS signal form the user segment. Since the transmitting power of the GPS satellites is less than 40 W, the signal is below the thermal noise on the Earth. As mentioned before, the signal reception and demodulation is done with the help of a correlation process. The receiver generates a local copy of the PRN-code derived from its internal oscillator. This local copy is electronically shifted in time and multiplied with the incoming antenna signal. If the received satellite PRN-code, which is hidden in the noise, and the replica signal coincide, the result of the multiplication, called the correlation function, is at a stable maximum and the receiver's tracking loops can lock to the satellite. It is obvious that this process also requires a local replica of the received carrier-frequency. The carrier replica has to be shifted in frequency, because the received satellite carrier frequency is affected by the Doppler effect.

Figure 2.3 shows the correlation principle exemplarily for one chip of the code. The black rectangular function is the incoming code chip. If the local copy (blue

rectangle) is in phase with the incoming code chip, the correlation function is at its maximum (blue arrow), as depicted in the right picture. In the left picture the replica code is  $1/4$  code chip too early.

In fact, a GPS receiver uses two additional replica codes to detect the maximum of the correlation function. One of them is earlier (green rectangle) than that which should be in phase with the incoming code and one is later (red rectangular) with a fixed offset (0.5 code chips in Figure 2.3). Consequentially, the additional copies of the code are called early and late replica, respectively, while the copy that should be in phase with the incoming signal is called prompt replica. If late and early correlation function (green and red arrow, respectively) are in agreement, the maximum correlation of the prompt replica is accomplished. Thus, the receiver searches for the zero crossing of the difference of early and late correlation function. This process has to be done in several receiver channels simultaneously in order to allow the receiver to track the signals of multiple satellites at the same time. The length of the code chips determines the width of the correlation function and thus the achievable precision.

The correlation process allows the receiver to measure the phase of the satellite code with respect to its local clock. The length of one PRN C/A-code is 1023 code chips and the repetition rate is 1 ms. Thus, these measurements have to be aligned to the GPS system time by the help of the navigation message in order to get an unambiguous measurement. This is possible with the help of a 20 ms data sequence in the navigation message, the so-called handover word, which is periodically repeated and allows for aligning one of the 20 C/A-code sequences within this message to the GPS system time, as transmitted by the satellite. With this information and the correlation measurement the receiver is able to calculate the apparent signal propagation time between satellite and receiver. Multiplying this propagation time with the speed of light yields the range between receiver and satellite. However, there are propagation errors on the signal path and the clocks are not perfectly synchronized. For this reason the measured quantity is called "pseudorange".

The correlation and the demodulation of the signals is usually done by a micro-processor. The antenna signal is converted to an intermediate frequency (IF) by mixing it with a frequency derived from the receiver's local oscillator, as done in an ordinary radio, but then the IF is directly sampled and converted to a digital stream. The receiver channels and the correlators are only virtually existing. A good explanation of the details of the correlation measurement, the demodulation of the navigation message, and technical details of GPS receivers are given in reference [4]. The structure and the contents of the navigation message are described in the documentation [25].

It has to be outlined here that the P-code has a repetition rate of one week and that its PRN sequence is encrypted. Thus a direct tracking of the P-code is restricted to authorized users with a special key. However, modern receivers can

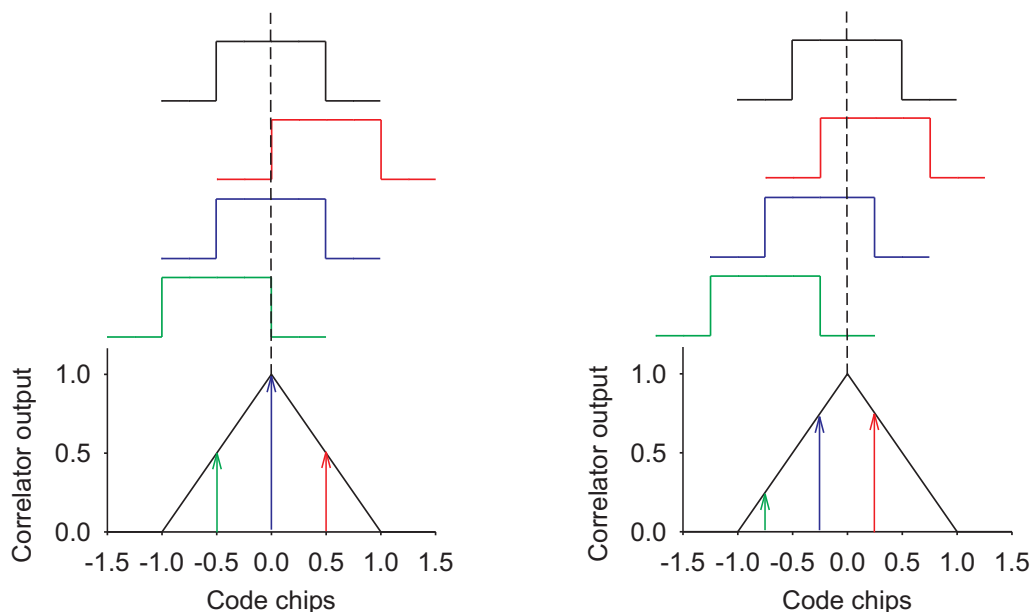


**Figure 2.3.:** The correlation principle for one code chip. The code chips are symbolized by the rectangular functions. The black function depicts the incoming code chip, the green, blue, and red functions are the early, prompt, and late replicas, respectively. The triangular function is the correlation function. The arrows show the correlator output related to the distinct replica. The left picture shows a situation in which the prompt replica is in phase with the incoming signal, while in the right picture the replicas are  $1/4$  code chip too early. This figure is similar to the figure given on page 148 of reference [4].

track the P-code on both frequencies after locking to the C/A-code by performing a cross-correlation between the signals on the two frequencies. As explained later, receiving a signal on both frequencies has the advantage of providing a correction of the signal path delays induced by the ionosphere. Receivers which are tracking the P-code with the help of the C/A-code show the same measurement noise as ordinary C/A-code receivers. They cannot benefit from the narrower correlation peak due to the higher chipping rate of the P-code providing a higher precision, because the C/A-code is always needed to keep the replica carrier frequency and the cross-correlators in the correct phase relationship.

Since the receiver needs to lock on the carrier frequencies of the satellites, it can provide a measurement of the phase of the received signal with an ambiguity of multiples of cycles of the carrier frequency. Modern receivers can do this with a precision of better than 1% of the wavelength [5], but the initial phase cannot be related to the GPS system time and is always ambiguous.

In principle the operation of GLONASS is similar to that of GPS, but GLONASS uses the same PRN code on all satellites. Instead, the satellites use different carrier frequencies. This technique is called Frequency Division Multiple Access (FDMA). The advantage is that if there is an interfering signal on one of the frequencies not the complete system will fail to operate. The disadvantage is that different frequencies have different delays within the analog part of the receiver which makes it much more difficult to calibrate a GLONASS receiver. The GLONASS space segment consists only of three orbital planes. and the satellites are controlled by a master control station nearby Moscow in Russia. A description of GLONASS and its frequencies is summarized in the reference [4].

All GNSS systems planned for the future will use the CDMA technique. Hence they can provide some of their signals on the same frequencies as GPS and a modern receiver in principle just needs an update of the internal processing software to be able to track the new satellites.

In addition to the GNSS system local augmentation systems based on geostationary satellites exist. These systems mostly transmit signals on the  $f_1$  frequency. However, these systems are not used for time and frequency comparisons and are not subject of this work.

### 2.3.2. Coordinate Systems and Satellite Motion

In this subsection the nomenclature and the satellite motion used throughout the remainder of the work (e.g. in Chapter 4) are explained. Basic relations for the coordinate systems and the transformations between them are given in Appendix A. A short mathematical description of the satellite motion is outlined in Appendix B. It is needed later in Chapter 4

The position of the receiver's antenna and also the position of the satellites can be represented in a right-handed Cartesian coordinate system  $(x, y, z)$  with the origin located at the center of mass of the Earth. The  $x$ -axis is pointing to the Greenwich meridian in the meridian plane, while the  $z$ -axis coincides with the rotational axis of the Earth. Thus the  $(x, y)$ -plane rotates along with the Earth. The position of a receiver located at a fixed point on the Earth surface does not change with time in these Earth Centered Earth Fixed (ECEF) coordinates, neglecting very small effects at the cm/year level due to continental drifts and tidal effects on the solid Earth surface induced by the gravitational force of the Moon.

The ECEF system can be expressed with the geodetic coordinates  $\varphi$ ,  $\theta$  and  $h$ , representing the geodetic latitude, longitude and height, respectively. The flattening of the Earth has to be taken into account.

Different realizations of the ECEF system with different parameters for the flattening of the Earth are in use. The ECEF reference frame used by the GPS control segment to predict the ephemeris data broadcasted with the navigation message is the World Geodetic System 1984 (WGS 84), while the frame used by GLONASS is

the PZ-90 system [4]. To improve the precision of position estimates and/or time and frequency comparison results ephemeris data provided by a different source are often employed in post-processing applications. The reference frames of this ephemeris data can differ from the reference frames broadcasted by the satellites, e.g. the frame used by the International GNSS Service (IGS) is the International Terrestrial Reference Frame (ITRF) which is in agreement with the conventions of the International Earth Rotation Service (IERS). The IGS and the usage of its data are described in Section 2.5.

The motion of a satellite around the Earth can be described in a right handed coordinate system using the Earth's center as the origin. A convenient choice is the so-called Earth-Centered Inertial Coordinate System (ECI) with the  $x$ -axis pointing to the vernal equinox and the  $z$ -axis defined as the Earth's rotational axis on January 1st 2000, 12:00 UTC [5]. The satellite motion is very well approximated by Newtonian mechanics. The ECI system is e.g. needed to derive relativistic effects (see Appendix F).

The azimuth and the elevation of the satellite are defined in a local left-handed coordinate system with the receiver antenna's being located at the origin.

### 2.3.3. Observation Model

The observation model, connecting the measurements of a receiver to the geometry and delays induced by physical influences are essential to understand the functionality of GNSS system. Thus, they are introduced briefly in the following.

The geometric range between one satellite  $s$  at the time of signal emission  $t_s$  and the receiver's antenna at the time of signal reception  $t_r$  is given by

$$\rho_s(t_s, t_r) = \sqrt{(x_s(t_s) - x_r(t_r))^2 + (y_s(t_s) - y_r(t_r))^2 + (z_s(t_s) - z_r(t_r))^2}, \quad (2.3)$$

and the observation model for the code measured pseudorange  $C_s$  (in units of meters) is given by [5]

$$C_s(t_s, t_r) = \rho_s(t_s, t_r) + (\delta t_r - \delta t_s)c + \Delta_C + \varepsilon. \quad (2.4)$$

Here  $C_s$  can stand for the measurement of the C/A-code as well as for the P1 and P2 code measurement, respectively, or for linear combinations of the data which are explained later.  $\delta t_r$  and  $\delta t_s$  denote the offset of the receiver and the satellite clock with respect to a common reference time (e.g. the GPS system time), respectively,  $\Delta_C$  summarizes all physical influences on the signal path and the satellite clock,  $\varepsilon$  denotes the noise of the measurement process, and  $c$  is the speed of light in vacuum. This equation is valid for all satellite navigation systems, including the Russian GLONASS.

The delay due to physical influences on the code measurement can be modeled as

$$\Delta_C = \delta_{\text{ion}} + \delta_{\text{tro}} + \delta_{\text{tide}} + \delta_{\text{mul}} + \delta_{\text{rel}}, \quad (2.5)$$



with  $\delta_{\text{ion}}$  and  $\delta_{\text{tro}}$  being the signal delays induced by the refractivity of the ionosphere and the troposphere,  $\delta_{\text{tide}}$  denoting variations due to deformation of the Earth's surface by the gravitational potential of the Moon and the Sun and ocean tides, and  $\delta_{\text{mul}}$  denoting multipath delays due to signal reflections at buildings, trees, and hard grounds nearby the receiver's antenna and diffraction effects.  $\delta_{\text{rel}}$  summarizes the relativistic effects.

The model for the carrier-phase measurement is given by

$$\lambda\Phi_s(t_s, t_r) = \rho_s(t_s, t_r) + (\delta t_r - \delta t_s)c + \lambda N_s + \Delta_\Phi + \varepsilon . \quad (2.6)$$

$\Phi_s$  is measured in cycles of the carrier frequency. As in equation (2.4), it can be the phase measurement on the  $f_1$  or  $f_2$  frequency or a linear combination of these measurements in cycles of the carrier frequency.  $\lambda$  is the corresponding wavelength. Since the initial number of carrier frequency cycles between satellite and receiver antenna are unknown,  $\lambda\Phi$  does not directly represent the pseudorange. This ambiguity is expressed by  $N_s$ .

For the carrier-phase measurement the respective delay due to physical influences reads

$$\Delta_\Phi = -\delta_{\text{ion}} + \delta_{\text{tro}} + \delta_{\text{tide}} + \delta_{\text{mul}} + \delta_{\text{rel}} + \delta_{\text{Ant}} + \delta_{\text{pwu}} . \quad (2.7)$$

In contrast to the code measurement the ionospheric error has the opposite sign, because the group velocity of the satellite signal is different from the phase velocity in the ionosphere, which is explained below.  $\delta_{\text{Ant}}$  is related to changes of the antenna phase center for different elevation angles of the incoming signal and  $\delta_{\text{pwu}}$  denotes phase wind up effects.

In terms of positioning, the equations (2.4) and (2.6) are usually solved by a linearization. After an expansion to a Taylor series either a least-square estimation algorithm [5], or, particularly in case of a moving receiver, a Kalman filter [26] is used. The measurements of at least four satellites are necessary in order to solve for the three coordinates and the receiver clock. In case of time and frequency comparisons, in principle the signals of one satellite are sufficient, since the receiver's antenna position is fixed and well known.

Depending on the desired precision more or less of the delays in (2.5) and (2.7) have to be removed by mathematical models, in terms of positioning as well as in terms of time and frequency comparisons.

### 2.3.4. Time and Frequency Transfer Receivers

In contrast to positioning, where the pseudorange observations (2.4) are used to determine the position of the receiver, the task in the framework of time and frequency comparisons is to solve for the receiver clock offset  $\delta t_r$ . The position of the antenna is usually static within the reference frame, neglecting the small variations mentioned above. For this account, GNSS receivers used for time and

frequency comparisons must allow for referencing the measurements to an external timescale physically provided by an 1 PPS signal.<sup>1</sup>

A typical timing receiver system used in a timing laboratory consists of the receiver itself, which is usually located in a temperature stabilized environment, and an antenna which is located outside, preferably at a site with minimum multipath effects. In case of some receivers additional computers to collect and process the measurement data are needed.

In the majority of cases the antenna and the antenna cable are not temperature stabilized and have to meet strict conditions to the stability. As outlined in reference [27] the delay of the antenna cable should vary less than 0.05 ps per degree per meter over the range  $-30^{\circ}\text{C}$  to  $+40^{\circ}\text{C}$  and the antenna should tolerate diurnal temperature changes of  $40^{\circ}\text{C}$ .

Two different basic design concepts for a time and frequency transfer receiver are possible. Figure 2.4 shows the more traditional set-up. The GPS measurements are at first referenced to the time of an internal oscillator. The internal oscillator can either be synchronized to an external frequency or to the frequency derived from the satellite's signals. The dashed lines indicate that in principle both synchronization methods can be utilized. The internal timescale is synchronized to the GNSS time. An external 1 PPS signal is compared to the 1 PPS signal generated from the internal oscillator with a TIC. Since the GNSS measurements are also referenced to the internal oscillator, it cancels out after the TIC and GNSS data are combined.

This design can be realized differently. For example, it is not necessary that the TIC and the computer that combines the GNSS and TIC data are integrated in the same housing together with the GNSS receiving and analyzing parts of the system. A system can be assembled from multiple devices.

Integrated time and frequency receivers of this type are available on the market since decades. Some older devices were so-called single-channel receivers. These receivers were capable to track only the C/A-code signals of one satellite at the same time, which is in principle sufficient for time transfer. For CV time comparisons between remote sites with these receivers, a schedule was needed to ensure that both sites track the same satellite at the same time. Such schedules are still provided by the BIPM for international timescale comparisons, but the usage of that kind of receivers diminishes.

Newer multi-channel receivers are capable to track several satellites at the same time [28]. Modern state-of-the-art time and frequency receivers which are constructed according to the set-up depicted in Figure 2.4 are usually based on geodetic receiver circuit boards. These boards are originally intended for precise positioning applications together with a post-processing of the output data, but output a 1 PPS signal derived from the internal clock. They are capable to track the C/A-

---

<sup>1</sup>If only a frequency comparison is desired, it is sufficient to reference the receiver's measurement to an external reference frequency with ambiguous phase.

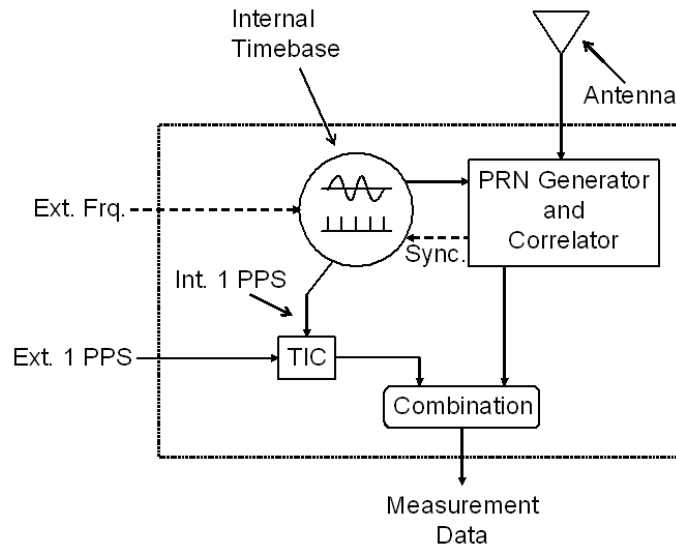


**Figure 2.4.:** Simplified schematic of a traditional time and frequency transfer receiver. All parts of the receiver which are analyzing and processing the GPS signal are summarized as "correlator".

code as well as the P-code on both frequencies and to measure the carrier-phase. The boards are integrated together with the TIC and a computer which combines the data.

While older receivers which are only tracking the C/A-code are pure GPS receivers, some of the modern geodetic receivers are capable of tracking the signals of the other GNSS systems. If the internal delays of receivers designed as shown in Figure 2.4 are well known, the 1 PPS input connector can be defined as the receiver's reference point to which all measurements are related.

Another design concept for time transfer based on geodetic receivers is depicted in Figure 2.5. Some of these receivers allow for synchronizing the internal timescale to an external 1 PPS. The internal timescale is thereby related to the first zero crossing which follows the external 1 PPS signal. Hence the 1 PPS signal and the reference frequency must be coherent, which means that both signals have to originate from the same source.

The advantage of a receiver designed according to Figure 2.5 is that no additional noise of a TIC affects the measurements. However, the definition of a reference point is more difficult, because in a timing laboratory the relation between 1 PPS signal and reference frequency is a priori not fixed. It depends on the cable lengths and the delays of the signal distribution equipment. Thus an additional measurement is required which must be repeated every time the setup is changed.

The delay between the 1 PPS and the zero crossing of the frequency can directly be measured using an oscilloscope or a fast TIC. If the result is applied to all

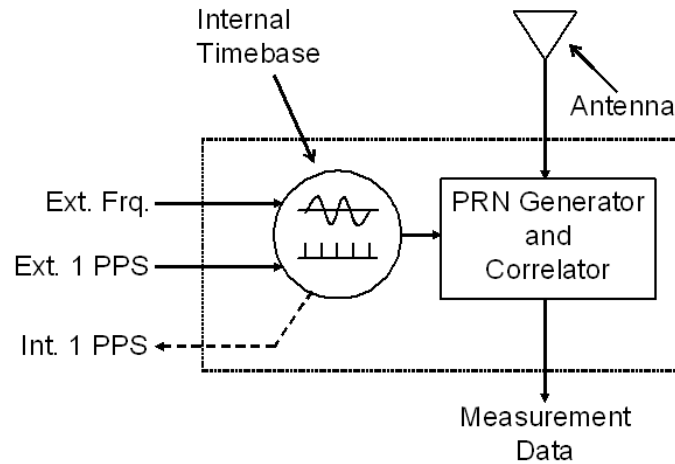


**Figure 2.5.:** Simplified schematic of a typical time and frequency transfer receiver based on geodetic technologies.

measurements, the 1 PPS input connector of the receiver can such be considered as the reference point. Alternatively, the delay between the input 1 PPS and the output 1 PPS can be measured with a TIC if the receiver provides an 1 PPS output. In this case the GPS measurements are related to the output 1 PPS.

In both design concepts the internal delays of the system should be well defined and provided by the manufacturer, as well as the delay of the antenna cable and the antenna. This includes the signal propagation time difference between the two frequencies inside a modern receiver. The value of the trigger level of the 1 PPS input detection should be known or adjustable [27].

According to the recommendations of the Consultative Committee for Time and Frequency (CCTF) a time receiver provides its code based measurements in the so called CGGTTS standard [29]. The data are given in 16 min intervals for each satellite and are computed using pseudorange measurements recorded in 1 s intervals. A detailed description of the CGGTTS file can be found in the reference [29]. The relevant parameters are the time differences between the satellite clock and the receiver timescale, which is related to the external timescale, and between the GNSS system time and the receiver timescale, respectively. A cutout of a typical CGGTTS file is shown in Appendix C.

The internal processing software of the receiver reduces the data by applying quadratic fits to 15 successive measurements. These 15 s averages are corrected for the atmospherical delays and the clock corrections taken from the navigation message in order to get access to the GNSS system time. The known internal delays of the receiver, the antenna delay, and the delay of the reference signal are applied. The geometric range between the antenna and the satellite (2.3) is calculated by

using the broadcast ephemeris data and a fixed position for the antenna which is manually entered into the processing software.

The final results are obtained by a linear fit to 52 successive 15 s averages. Thus, the total averaging time is 780 s. The gap of 3 minutes between the 16 minute data spacing and the averaging time is inherited from the use of old single-channel receivers which needed this time to detect and lock to a signal of a new satellite.

Besides the CGGTTS data a second data standard is used within the framework of time comparisons. Originally defined for geodetic applications, modern receivers record their measurement data in the Receiver Independent Exchange Format (RINEX) [30]. For each satellite in view the raw measurement data of the C/A, P1, P2 pseudoranges in meters and the cycles of the carrier-phase on both frequencies are recorded in the RINEX observation file. Some receivers provide additional information, like the Doppler effect on the signal, the signal-to-noise ratio, or the pseudorange measurements of a regional satellite based augmentation system.

The spacing of the data is not prescribed in the RINEX standard [30]. Usually 30 s intervals are used. The timetags can be related either to the GPS or the GLONASS timescales, but mostly the GPS time is utilized as receiver time scale. The timetags are given as year, month, day, hour, minute, and second. The broadcast satellite ephemeris and clock data are recorded in a separate file, the RINEX navigation file. The observation data of a multi-system receiver contain the measurement data of all GNSS systems, while the navigation files are generated separately for GPS and GLONASS. A cutout of a typical 30 s GPS RINEX file is shown in Appendix D.

The original idea of the RINEX definition was to enable post-processing of the measurement data for high precision positioning applications and network solutions, independent from the hardware and correction models favored by the hardware manufacturer.

A lot of geodetic receivers designed as depicted in Figure 2.5 do not provide CGGTTS data, because the CGGTTS standard is used in the timing community only, which is small compared to the geodetic community. Thus, a software called RINEX2CGGTTS was developed at the Royal Observatory of Belgium (Observatoire Royal de Belgique, ORB) which allows for generating standard CGGTTS files from daily 30 s RINEX observation data by combining it with two days of data of the navigation files [31]. The fixed antenna position must be entered to the this software. The internal delays, the antenna delay, and the reference delay have also to be entered to the software, because they are usually not applied to the RINEX data since they are of no interest in positioning applications.

## 2.4. Signal Delays and Correction Models

The GNSS technique, in terms of positioning as well as in the framework of time and frequency comparisons, is a one-way technique. Thus, all signal delaying effects and influences on the clocks in the transmitting satellites are affecting the results, if they are not removed by models or technical tricks.

In the following the different effects are briefly introduced and explained. All correction models which are studied in detail within a simple frequency transfer algorithm developed at PTB (Section 4.4) are explicitly outlined as mathematical expressions. Further informations are given in the appendix.

### 2.4.1. Atmospherical Corrections

The propagation of the satellite signals is affected by the ionosphere, which is the region of the atmosphere between about 70 km and 1000 km above the Earth surface [4], and the troposphere, which is in terms of satellite navigation the complete region of the atmosphere below the ionosphere [5].

The change of the apparent length of the path of a signal in a medium with refractivity  $n$  compared to a signal propagating in the vacuum reads

$$\Delta r = \int_{\text{Path}} (n - 1) ds . \quad (2.8)$$

Since the troposphere affects the satellite signals by the presence of neutral atoms and molecules [5], the troposphere is a non-dispersive medium for frequencies below 15 GHz [4], which means that the effect is the same on all GNSS frequencies. The group and phase velocity of the signals are equal.

The refractivity of the troposphere is usually rescaled by  $N = 10^6(n - 1)$  and sometimes separated into wet and dry parts  $N = N_w + N_d$ . Thus equation (2.8) for the troposphere becomes

$$\delta_{\text{tro}} = \text{Tro} = 10^{-6} \int_{\text{Path}} N ds = \int_{\text{Path}} N_w ds + \int_{\text{Path}} N_d ds = \text{Tro}_w + \text{Tro}_d . \quad (2.9)$$

The wet part of the troposphere is the region below 10 km and contributing with about 10 % to (2.9), while the remaining 90 % are due to the dry part of the troposphere.

The integration is usually done along the zenith path and aligned to the signal path by a mapping function afterwards. The mapping function is depending on the satellite elevation.

The most commonly used solutions for (2.9) are the Saastamoinen [32] and the Hopfield [33] model. Sometimes a simplified model is sufficient [34], depending on

the desired precision. Together with the related mapping functions it can be given by

$$\text{Tro}_{z,w} = 0.1 \text{ m} , \quad \text{Tro}_{z,d} = 2.31e^{-h/7000 \text{ m}} \text{ m} , \quad F_w = F_d = 1/\sin(el) , \quad (2.10)$$

where the index  $z$  denotes the tropospheric delay in the zenith direction.  $F_w$  and  $F_d$  are the mapping functions.  $h$  is the geodetic altitude of the receiver's antenna, and  $el$  is the satellite's elevation.

In contrast to the troposphere, the ionosphere affects the satellite signals by free electrons caused by ultraviolet radiation from the sun which ionizes gas molecules. Usually a GPS receiver uses forecasted parameters broadcasted in the GPS navigation message to correct for this delay. Details of this model can be found in the references [5, 25]. The GLONASS navigation message does not include such parameters [35]. Modern receivers which are capable to receive both systems simultaneously can use the parameters in the GPS navigation message also for the correction of the GLONASS signals.

The ionosphere is a dispersive medium, group velocity and phase velocity are influenced with opposite sign. This property can be used, if the receiver is capable to receive signals on both frequencies  $f_1$  and  $f_2$ , to remove the ionospheric delay from the observation equations in first order by a linear combination. If P1 is the P-code pseudorange on  $f_1$  and P2 the P-code pseudorange on  $f_2$ , the linear combination is given by

$$\text{P3} = \frac{f_1^2 \text{P1} - f_2^2 \text{P2}}{f_1^2 - f_2^2} . \quad (2.11)$$

A brief derivation is given in Appendix E.

Equation (2.11) is called the ionosphere free linear combination since the higher order effects are marginal under normal conditions. Small significant effects occur only in the case of high ionosphere activity due to solar storm events [36].

Inserting the GPS frequencies the combination (2.11) can be written as

$$\text{P3} = \frac{154^2 f_0^2 \text{P1} - 120^2 f_0^2 \text{P2}}{f_0^2 (154^2 - 120^2)} = \frac{154^2 \text{P1} - 120^2 \text{P2}}{9316} . \quad (2.12)$$

For the carrier-phase measurement one can define  $L1 = \lambda_1 \Phi1$  and  $L2 = \lambda_2 \Phi2$ , with  $\Phi1$  being the measurement at the frequency  $f_1$  with respect to one satellite and  $\Phi2$  being the measurement at the frequency  $f_2$  with respect to the same satellite.  $\lambda_1$  and  $\lambda_2$  are the corresponding wavelengths. Then a ionosphere free linear combination can also be constructed for the carrier-phase measurements:

$$\text{L3} = \frac{f_1^2 L1 - f_2^2 L2}{f_1^2 - f_2^2} . \quad (2.13)$$

With the assumption that the pseudorange measurements P1 and P2 are affected by independent additive noise with variances [37]

$$\text{Var} [\text{P1}] = \text{Var} [\text{P2}] = \varepsilon^2 , \quad (2.14)$$

the variance of the P3 combination is

$$\text{Var} [\text{P3}] = \text{Var} \left[ \frac{f_1^2 \text{P1} - f_2^2 \text{P2}}{f_1^2 - f_2^2} \right] = \frac{f_1^4 + f_2^4}{(f_1^2 - f_2^2)^2} \varepsilon^2, \quad (2.15)$$

according to the calculation rules of variances. After inserting the values of the GPS frequencies the P3 variance becomes

$$\text{Var} [\text{P3}] = 8.87 \varepsilon^2, \quad (2.16)$$

with the standard deviation

$$\varepsilon_{\text{P3}} = 2.98 \varepsilon. \quad (2.17)$$

Equation (2.15) is also valid for the L3 combination (2.13). The benefit of canceling out the ionosphere error in first order due to the usage of (2.11) and (2.13) has to be paid for with increased noise.

It has to be noted that higher order contributions to the ionospheric refractivity, which are neglected in (E.19) and (E.20), can only be removed by using more than two frequencies or model values for the Earth magnetic field. In terms of a future modernization of the GPS system the transmission of a signal on a third frequency  $f_3 = 115f_0$  is planned [5] and all newly developed GNSS systems will broadcast signals on more than two frequencies.

### 2.4.2. Relativistic Corrections

Relativistic effects arise due the gravitational potential of the Earth, the motion of the satellite and the rotation of the Earth.

From the point of view of a user on the Earth the satellite clocks are shifted by general relativistic effects due to the mean gravitational potential of the Earth and the mean velocity of the satellite on its orbit. This correction has not to be taken into account by the user, because it is already applied in the design of the GPS satellites. The clocks in the satellites are adjusted to provide an output frequency of about 10.22999999543 MHz. An observer on the Earth geoid thus observes the nominal frequency of 10.23 MHz [4, 5, 38].

Since the satellite orbits are not perfect circles but ellipses, the gravitational potential and the velocity undergo variations. Thus, also the frequency observed by a user on the Earth varies. This effect can be modeled approximately as

$$\Delta t_e = \frac{2}{c^2} \vec{r}_s \cdot \vec{v}_s. \quad (2.18)$$

It is called the eccentricity correction [4, 38].

A second effect that has to be corrected by the user is the so-called Sagnac effect. It is related to the rotation of the Earth. A possible approximation is

$$\Delta t_S = \frac{1}{c^2} \vec{\omega}_E \cdot [\vec{r}_R \times (\vec{r}_R - \vec{r}_T)], \quad (2.19)$$



with the angular velocity vector of the Earth  $\vec{\omega}_E$  and  $\vec{r}_R$  and  $\vec{r}_T$  the receiver's and satellite's position at reception and transmission time, respectively. For many applications it is sufficient to estimate  $\vec{r}_R - \vec{r}_T$  from the pseudorange measurement (2.4).

Appendix F outlines a brief derivation of the three corrections introduced above.

### 2.4.3. Multipath

The multipath delay is one of the most difficult to predict delay sources [4, 5]. The satellite signal could be reflected at objects nearby the antenna. These could be buildings, trees, hard grounds, or mainly metal objects, respectively. The reflected signal and the direct signal interfere with each other at the antenna phase center and the correlation measurement, and thus the pseudorange measurement is affected. These delays are geometry, site, and time dependent. It is obvious that this delay cannot be corrected with a mathematical model. But it can be minimized with some technical tricks.

A first reduction is achieved due to the right-handed circular polarization of the satellite signals. The receiving antenna attenuates the reflected signal, because it is designed for right-handed polarization and the polarization has likely changed after the reflection.

Further reduction is accomplished by using choke ring antennas or so-called "pin-wheel" antennas [39]. The former are antennas equipped with vertical metal rings aligned concentrically around the receiving part. These rings are connected to electrical ground and signals with negative elevation angles are attenuated. The latter are based on a commercial patent-registered design consisting of a phase array of aperture-coupled spiral slots optimized for right-handed circularly polarized signals.

Modern receivers can minimize the impact of multipath on the correlation measurement by using the concept of "narrow correlators" [40]. The reflected signals have at most 1/3 of the signal strength compared to the direct signals [5]. A superposition of the direct and the reflected signal deforms the resulting correlation function [4], as depicted in Figure 2.6.

The receiver's tracking loops are thus unable to find the correct maximum, if the spacing between early and late correlator is too big. For smaller spacing this effect could partially be compensated. This requires a higher bandwidth of the receiver, as demonstrated in reference [40]. Since the correlation process is usually done completely digital, this means a higher sampling rate and the capability of the receiver processor to analyze a high amount of data, which has become possible only through the progress in modern microelectronics.

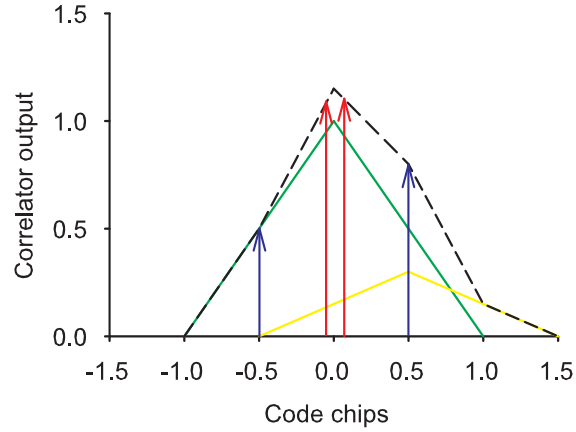


**Figure 2.6.:** The deformation of the correlation function due to multipath. The green line shows the correlation function for the direct received signal, the yellow line is the multipath signal correlation function, the black line is the superposition. The blue arrows depicts the correlator output for 1.0 chip early and late correlator spacing. The red arrows depict the correlator output for narrow early and late correlator spacing.

#### 2.4.4. Site Displacement

For high precision applications effects related to dynamical deformations of the Earth and forces on the satellites due to massive bodies in the solar system (mainly the Moon and the Sun) have to be considered. The knowledge of the latter is especially important within network applications, where the ephemerides of the satellites are to be determined with very high precision.

The deformation of the Earth surface is caused by the gravitational potential of the Moon and the Sun acting on the Earth's elastic body. The displacement of the station coordinates due to the changing gravitational force can be modeled and calculated from the positions of the Moon and the Sun. An approximation of the vector displacement  $\Delta\vec{r}$  of the station is given by [5]

$$\Delta\vec{r} = \sum_{n=1}^2 \frac{M_n a_E^4}{m_E R_n} \left\{ h_2 \hat{r} \left[ \frac{3}{2} (\hat{R}_n \cdot \hat{r})^2 - \frac{1}{2} \right] + 3l_3 (\hat{R}_n \cdot \hat{r}) \left[ \hat{R}_n - (R_n \cdot \hat{r}) \hat{r} \right] \right\}, \quad (2.20)$$

with  $a_E$  the equatorial radius of the Earth (semi-major axis of the Earth ellipsoid, cf. Appendix A),  $n = 1, 2$  indices for the Moon and the Sun, respectively,  $M_n$  the masses of the Moon and the Sun,  $m_E$  the mass of the Earth, and  $R_n$  the distances of Moon and Sun with respect to the center of mass of the Earth. The constants  $h_2 = 0.6078$  and  $l_2 = 0.0847$  are the so-called degree two Love and Shida numbers, respectively.  $\hat{R}_n$  are the unit vectors of the distance vectors of the astronomical

objects (Moon, Sun) with origin at the center of mass of the Earth, and  $\hat{r}$  is the unit vector of the antenna's position vector.

Since the antenna position is known in ECEF coordinates, also the positions of the Sun and the Moon have to be known in this coordinate system. In Appendix G it is explained how the positions of these astronomical bodies are estimated in the ECEF system. More details concerning the model and the calculation of the momentary position of Moon and Sun are given in reference [5]. In time transfer on long intercontinental baselines the Earth displacement has an impact of up to 3 ns if it is not modelled, as demonstrated in Section 4.4.

Another deformation of the solid Earth surface is caused by the falling and rising tides of the ocean, caused by the gravitational potential of the Moon. The periodical redistribution of the water masses causes periodic loading of the ocean bottom. Also the solid Earth deforms under this load. These ocean loading effect can be modeled, but are different at each location. Details of general models and the calculation of the coefficients are explained in the references [5, 41, 42]. The coefficients can be calculated for each station via an on-line program provided by the Onsala Space Observatory in Sweden [43].

#### 2.4.5. Other Delay Sources

For high precision orbit determination the perturbation of the gravitational potential seen by the satellites due to the forces of the Moon, the Sun, and other planets in the solar system can be corrected by a model. Furthermore, a model for the solar radiation pressure caused by the sunlight should be applied. GPS preprocessing analysis software often used algorithms to detect and remove phase wind-up effects. Details are extensively explained in reference [5].

Usually the ephemeris of a satellite are referenced to the center of mass of the satellite, but the pseudorange measurement is referenced to the phase center of the satellite's antenna array. Depending on the production series of the satellites the center of mass and the phase center do not coincide. This can be corrected by rotations, taking into account that the satellites' antennas are always pointing in the direction of the center of the Earth [5]. The variations of the receiver antenna are usually corrected by applying correction data, which is explained in the subsequent Section.

## 2.5. The International GNSS Service (IGS)

In kinematic GPS positioning the accuracy of the solution can be improved by using correction data from a fixed source with known position [4]. However, the accuracy of code based GPS applications is limited by the accuracy of the correlation measurement, which is determined by the chip rate of the PRN codes [4]. In order

to benefit from the carrier-phase measurements, which are up to 100 times more accurate than the code measurements [5], precise information about the satellite's ephemeris and the satellite's clocks are necessary. Otherwise the accuracy would be limited by the predicted broadcasted parameters. This can be achieved by operating the receiver as part of a network and solving the equations (2.4) and (2.6) for the complete set of measurements together with all relevant modeled corrections using an adjustment calculus [44]. Furthermore, correction data extracted from such a network can be used together with the measurements of a single receiver in a post-processing approach. Such a network is operated by the International GNSS Service (IGS).

The IGS is a voluntary federation of more than 200 institutes and agencies worldwide, collecting RINEX observation and navigation data of a worldwide network of reference stations [45]. Figure 2.7 shows the distribution of the stations. These stations are equipped with geodetic GNSS receivers and the data are uploaded to local data centers. Some of the receivers are combined GPS and GLONASS receivers. Furthermore, some stations are equipped with additional sensors providing meteorological data.

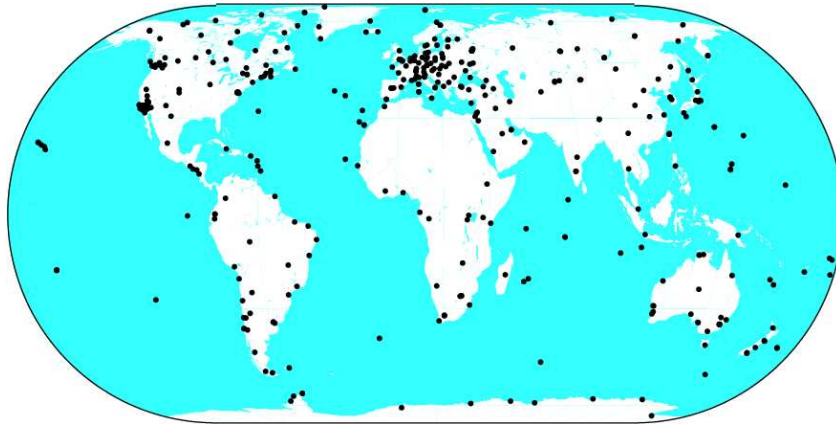


**Figure 2.7.:** The IGS network [46] in December 2010. Each dot indicates an IGS reference station.

Regional data centers collect the data from the local data centers, pass them to global data centers, and act as an archive for the data. Finally the GPS data are used by several analysis center for a precise determination of the satellite ephemeris, the satellite clocks, and the Earth orientation parameters. Each analysis center uses a different software package, applying the correction models introduced before and solving the equations (2.4) and (2.6) after linearization with an adjustment calculus for the satellite clocks, the ephemeris, and station positions and clocks, using the raw GNSS measurement data.

A set of stable sites, which have to comply with strict requirements, is used for the reference frame determination. The geodetic reference frame of the IGS is a realization of the ITRF [47] (see Subsection 2.3.2).

Finally a weighted average of the solutions of the analysis centers is calculated, with the weights depending on the quality of the solutions. In the context of the IGS these combined solutions are called "products", while the raw GNSS measurements are called "data". The products and data can be downloaded from the global analysis centers free of charge and can be used for high precision post-processing GNSS applications. In addition to the IGS products, some analysis centers also provide estimated ionosphere and troposphere parameters. Furthermore, the navigation data of the receivers are combined to global and regional RINEX navigation files, containing the broadcasted ephemeris of all satellites or of all satellites visible in a particular region of the Earth, respectively. A list of the data centers, the analysis centers, and the institutes participating in the IGS can be found in the reference [48], where the regional data centers are called "operational data centers". A description of the data formats used by the IGS is given in the reference [49].

The IGS provides the products in three different levels of precision. The Final Products (IGS) have the highest precision and internal consistency. The Final Products are the basis for the IGS reference frame. They are made available on a weekly basis with a latency of 12 days for the last day of the week. The Rapid Products (IGR) are available with a latency of 17 hours on a daily basis and their quality is nearly comparable to that of the IGS Final Products. For most positioning applications it is sufficient to use the IGR products. The Ultra Rapid Products (IGU) are updated four times a day at 03:00, 09:00, 15:00, and 21:00 UTC. They are intended for near real time applications with lower precision and are computed half with observed data and half on the basis of prediction. The latency of the IGS Final Products is mainly due to the latency of the observation data of several stations [15]. Thus the IGR Rapid Products are computed from a lower number of stations of the global network (Figure 2.7). For GLONASS only Final Products are available.

The IGS as well as the IGR products are computed on a daily basis, which means that the solutions for each day are calculated from the RINEX files provided by the IGS stations for this particular day. The orbit files contain the ephemeris data of each satellite in Cartesian ECEF coordinates within the IGS reference frame and the satellite clock with respect to the IGS timescale with low precision in 15 minute intervals time-tagged to the GPS time. The satellite's position represents the center of mass of the satellite. The clock files contain a daily realization of the IGS reference frame given as the positions of all contributing IGS stations and the high precision satellite and station clocks and their rates. In case of the IGS products, the clock file is available with 5 minute or 30 second intervals, while the IGR clock file is provided with 5 minute intervals only. IGU clock files are not available. GLONASS clock products are not yet provided by the IGS.

The IGS timescale is a weighted mean of the satellite clocks and the stations equipped with external frequency standards [50]. Stations connected to clocks with a good short term stability gain the highest weight, because the computation is done on a daily basis. The timescales of the IGS and IGR products can differ by several ten nanoseconds [50]. In the long term, the timescales are aligned to the broadcasted GPS system time.

Several of those stations that are connected to external frequency standards which are collocated at timing laboratories together with other GPS equipment. For example, at PTB the station "PTBB" is operated, consisting of an Ashtech Z12-T receiver, a meteorological sensor providing outside temperature, humidity, and pressure measurements, and the antenna installation. Since the PTBB receiver is connected to UTC(PTB), its data are provided to the BIPM in parallel, and CGGTTS P3 files are generated with the RINEX2CGGTTS software. In case of the P3 data the receiver is called "PT02". In principal the clock products can be used for a timescale comparison between the timing institutes in which an IGS station is located, but due to the daily analysis strategy the solution is affected by a phase discontinuity each day at midnight [50].

The satellite velocity is not included in the orbit product, but needed for the calculation of the relativistic eccentricity correction 2.18. Since the velocity  $\vec{v}_s$  at the epoch  $t$  is the derivative of the satellite position  $\vec{r}_s$

$$\vec{v}_s(t) = \frac{d\vec{r}_s(t)}{dt} \approx \frac{\vec{r}_s(t + \Delta t) - \vec{r}_s(t)}{\Delta t}, \quad (2.21)$$

it can be calculated from the ephemeris data. The position of the satellite can be interpolated from the 15 minute ephemeris data, for instance using the Lagrange interpolation [5]. The Lagrange polynomial is given by

$$x_n(t) = \sum_{j=0}^m \hat{x}_n(t_j) \prod_{k=0, k \neq j}^m \frac{t - t_k}{t_j - t_k}, \quad k \neq j, \quad n = 1, 2, 3, \quad (2.22)$$

with  $x_n(t)$  being on of the three component of the satellite position vector  $\vec{r}_s$  at the time  $t$  and  $\hat{x}_n(t_j)$  on of the three components of the satellite ephemeris data taken from the orbit file at the epoch  $t_j$ .  $m$  is the order of the polynomial and usually selected as 7 or 9 [5]. Also other interpolation techniques can be used, like Newton or Chebyshev polynomials.

Precise products with the same format that uses the IGS are also provided independently from the IGS by other institutes and agencies. For example, the US National Geospatial-Intelligence Agency (NGA) and the Russian Information-Analytical Center (IANC) provide such products. The NGA ephemeris data are referenced to the antenna phase center of the satellite, but no clock files are generated. The IANC data are with less precision, because only a few of the stations of the IGS network are included in the computation. In contrast to the IGS, the

NGA products include the satellite velocity and the IANC offers clock products for the GLONASS system. The products of other agencies are related to different reference frames and transformations according to equation (A.5) are necessary to enable comparability.

The advantage of using IGS products is that these products are the weighted average of several analysis centers, while the products of other agencies are usually done with one single processing strategy. Thereby errors are minimized and the reliability is increased. However, on the IGS data centers also the products of some of the participating analysis centers are available.

A further product of the IGS are files containing information about the Earth rotation and the polar motion, calculated from the network. This Earth rotation parameters can be used for the transformation between the ECI and the ECEF coordinate system (see Appendix A).

In addition, the IGS offers correction data for the antenna phase center of the satellites and for a variety of receiver antennas. The antenna phase center of the receiving antenna depends on the angle of the incoming signals and thus on the satellites' elevations.

## 2.6. Precise Point Positioning

Precise Point Positioning (PPP) is a post-processing method which was originally developed within the geodetic community to enable the determination of a position with sub-centimeter precision [15]. It makes use of the P3 code as well as of the carrier-phase measurements of a GPS receiver, taken from the RINEX data. The equations (2.4) and (2.6) are solved simultaneously together with all implemented correction models together with IGS like data after a linearization. For this purpose, either the least-square estimation method [5] or a Kalman filter [26] is used. The ambiguities of the phase of the carrier are estimated with the help of the P3 code. The code itself is weighted down in such a way, that the stability of the result is mainly that of the carrier-phase measurement. Different software concepts for the PPP method exist and are explained later in Chapter 4.

The PPP method can obviously be used for time and frequency comparisons, if the processing software outputs also the receiver clock estimations. In contrast to positioning of stationary antennas, where the solution can be improved by averaging over longer measurement data, for time and frequency transfer a solution for each epoch is needed. Since the ambiguities have to be estimated each time a PPP process is started, the clock estimates of continuous measurement data show a phase jump between the distinct independent PPP solutions, because the ambiguity can not be perfectly solved due to the noise of the code.

Figure 2.8 illustrates this discontinuity. Here the data of two receivers at PTB have been processed with the NRCAN-PPP software [26], which was developed

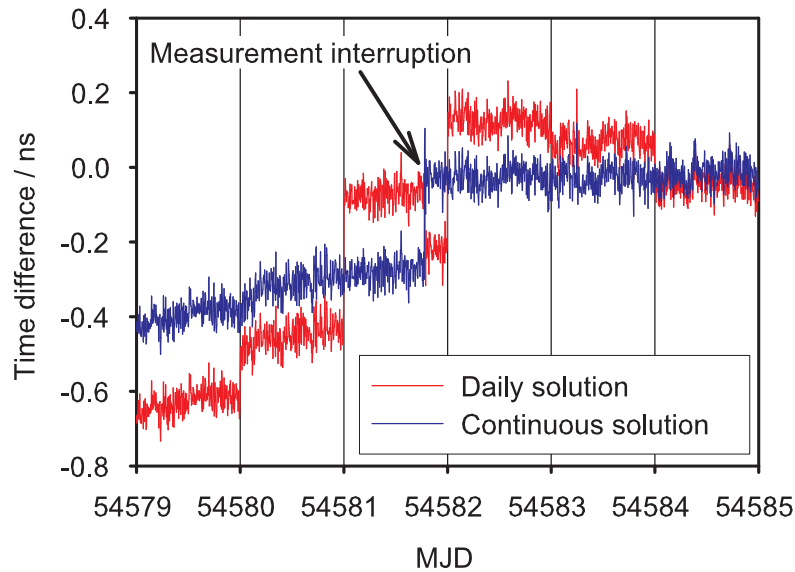


**Figure 2.8.:** Comparison between single day and multi day batch PPP processing. The daily solution shows daily phase discontinuities. The data are calculated from a comparison of two identical receivers which were connected to the same clock in a short baseline setup (distance between the antennas was just a few meters).

at the geodetic institute at Natural Resources Canada (NRCan). This software package is analyzed in detail in Chapter 4. Mostly the GPS receivers produce daily RINEX data with 30 s data spacing. If the PPP process is done independently for each daily file, the solutions can diverge from each other by a few hundred of picoseconds, although the receiver was continuously measuring. This is called the day-boundary phase jump.

The NRCan software allows for processing of longer periods than one day. One can assemble multiple RINEX files to a multi-day batch. The solution of the multi day batch shows a jump within MJD 54581, which is caused by a measurement discontinuity. The phase jump shows a different sign for the daily and the multi day processing. This shows that the phase jumps are statistically distributed. Despite of some weakness, PPP is currently the most stable method for time comparisons.

Geodetic GPS receiver models designed according to Figure 2.5, and only few time and frequency transfer receiver models apply the internal delays to the RINEX data, because the RINEX standard [30] was originally developed for geodetic applications where absolute phase values are not needed. The internal delays can be applied manually after the PPP processing. The total correction  $D$ , which has to be added to the PPP results, is given by

$$D = \frac{154^2 \cdot D_{P1} - 120^2 \cdot D_{P2}}{9316} + D_{Cab} - D_{Ref} \quad (2.23)$$



with the P1 and P2 delays  $D_{P1}$  and  $D_{P2}$ , respectively, the estimated antenna cable and antenna delay  $D_{Cab}$ , and the delay of the receiver's reference point with respect to the local UTC reference  $D_{Ref}$ . The frequency dependence of the antenna cable is absorbed in  $D_{P1}$  and  $D_{P2}$ .

Some receivers do not provide the P1-code. Then the differential code delay between the C/A-code and the P2-code has to be known.

Since PPP estimates the receiver clock independently for each receiver at any epoch, time and frequency comparisons using this method are always AV processes.

Besides using the PPP solution directly for time and frequency comparisons, PPP software could also serve to monitor the antenna positions used for the code based time transfer and for their periodical updating.

## 2.7. GPS and UTC Generation

The Coordinated Universal Time UTC is the world-wide reference timescale. Its generation and dissemination is one of the main tasks of the BIPM Time Department [10]. A physical realization of UTC is not existing. Instead, individual laboratories "k" realize an approximation to UTC, named UTC(k). The BIPM computes and publishes UTC-UTC(k) and its uncertainties [51] in five day intervals referenced to MJDs at 00:00 UTC in the monthly published Circular T (e.g. see Appendix H).

Figure (2.10) shows the international network of time links on April 2006. The timescales of the participating laboratories are compared to regional and global pivot laboratories using the TWSTFT and the GPS method. The a priori choice of the pivot laboratories (e.g. PTB as the global pivot laboratory) is arbitrary and could be by the BIPM if necessary. Few laboratories are equipped with TWSTFT stations. The main tool for international time comparisons is GPS. The use of GLONASS is in an experimental state, used only for the link between UTC(PTB) and the Russian timescale UTC(SU), and planned for the future [52].

By combining the results of the international time comparisons with the local clock intercomparison in the laboratories each clock can be compared with each other. The participating laboratories provide their GPS, TWSTFT, and clock comparison data to a central BIPM data storage. Usually more than one GPS receiver is operated in a time laboratory and different kinds of data (CGGTTS P3, CGGTTS C/A, RINEX) are available. For a link computation the BIPM uses the best available method. If data of an operational TWSTFT link are available, this method is preferred. The combination of GPS and TWSTFT is subject of studies [53].

To calculate the UTC timescale an algorithm called ALGOS is used by the BIPM [54]. It is a step-by-step algorithm. The link and the clock comparison data are filtered and cleaned from outliers. Single-frequency C/A-code data are

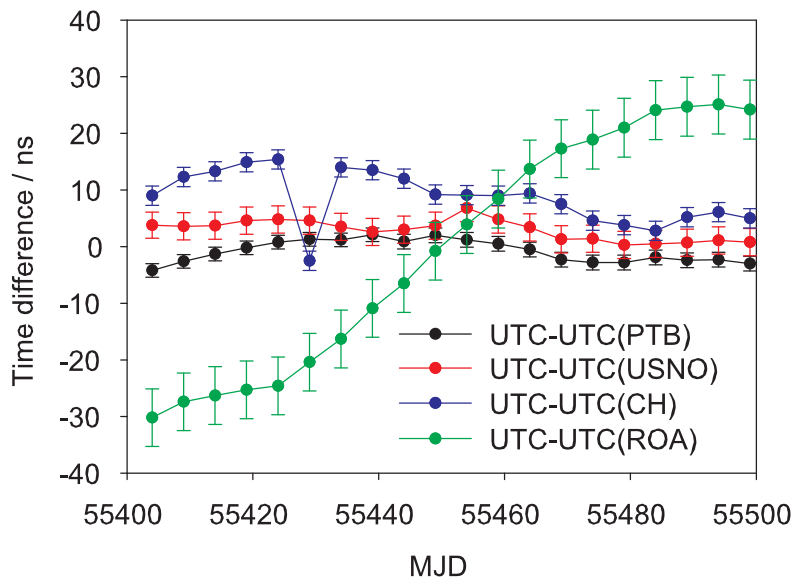


**Figure 2.9.:** Deviation from UTC of some selected timescales within 100 days in 2010, taken from the Circular T. UTC(PTB), UTC(USNO), UTC(CH), and UTC(ROA) are the local UTC realizations of the PTB, the USNO, the Swiss Federal Office of Metrology (METAS), and the Royal Spanish Naval Observatory (ROA), respectively. The uncertainty is represented by "error bars" and reflects the quality of time link calibrations (see Chapter 6).

corrected using ionospheric maps produced by the Center for Orbit Determination in Europe (CODE), which is one of the IGS analysis centers, located at the Astronomical Institute of the University Bern in Switzerland. Then the clocks are weighted depending on their instabilities and a free atomic timescale (Échelle atomique libre, EAL) is calculated as the weighted average of the more than 350 contributing clocks. Thereby the weighting procedure and the clock frequency prediction are chosen such that EAL is optimized for long-term stability. An upper limit for the weight of each clock is implemented [55]. By a comparison with the primary caesium clocks on a monthly basis a frequency steering is applied to EAL in order to ensure that the scale unit is close to the SI second on the geoid. The corrected timescale is called international atomic time (Temps atomique international, TAI). Finally, UTC is obtained by adding leap seconds to TAI as directed by the International Earth Rotation and Reference Systems Service (IERS). UTC is thus kept in agreement with the astronomical time UT1 within  $\pm 0.9$  s.

Besides publishing the difference UTC-UTC(k) for each participating laboratory together with the related uncertainty in the Circular T, the BIPM also provides the weights of the participating clocks and their rates with respect to TAI.

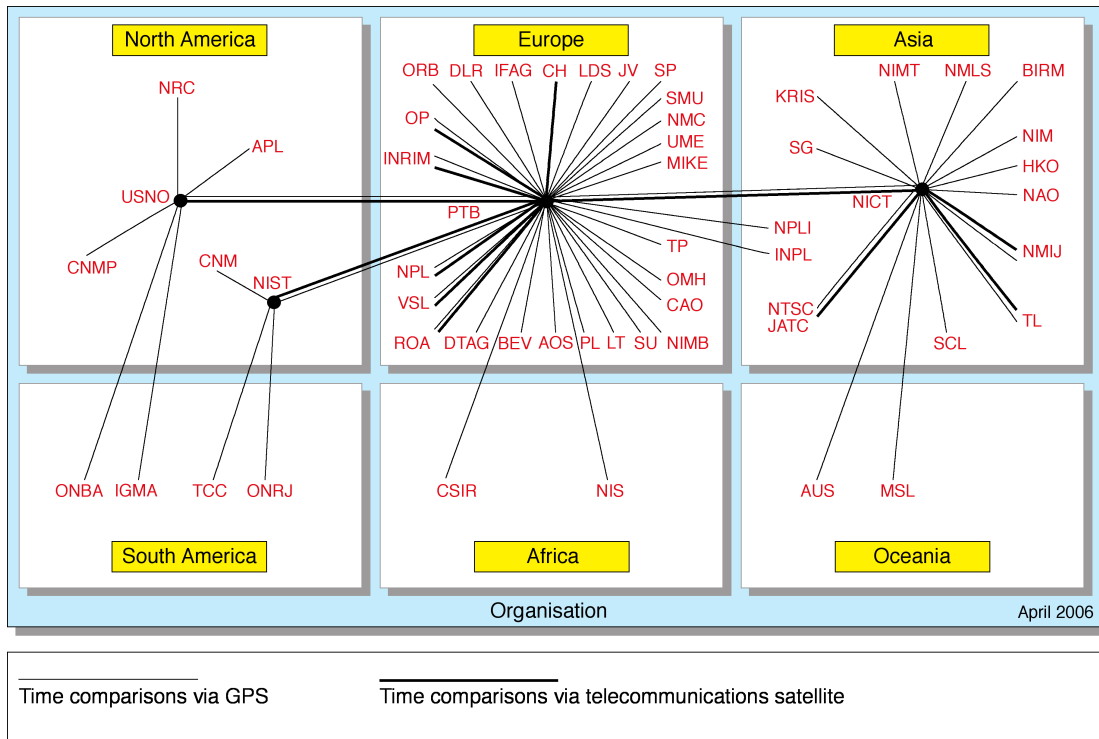


**Figure 2.10.:** The BIPM international network of time links in April 2006. This image is by courtesy of the BIPM.

The calculation of  $UTC-UTC(k)$  and its uncertainties requires the knowledge of the internal delays of the time transfer equipment involved or the uncertainty of the calibration of the time links. Up to now, operational links have been calibrated either by cost and labor intensive two-way satellite time and frequency transfer (TWSTFT) calibration campaigns, reaching the uncertainty of 1 ns [56], or by more easy to handle circulations of traveling GPS receivers [57]. The uncertainty of the latter has been estimated to be 5 ns, based on BIPM's long-term experience during the past decades.

The concept of BIPM GPS calibrations is explained in detail in Chapter 6. Advances based on experiments carried out with the ROA are shown. Here a further reduction of the uncertainty due to a revised concept including hardware improvements developed at PTB is demonstrated later in Chapter 6.

# 3. A Highly Precise Mobile Frequency Reference

## 3.1. Motivation

The PTB disseminates a standard frequency (77.5 kHz) and coded time information via the long wave transmitter DCF77 located at Mainflingen nearby Frankfurt/Main [7]. However, this service is not capable to provide a sufficiently stable and accurate reference for many scientific applications.

The absolute measurement of optical frequencies requires a highly precise reference frequency with relative uncertainty of measurement ideally far below  $10^{-14}$  at one day averaging time. Such experiments are e.g. carried out at the LUH in the framework of the Center for Quantum Engineering and Space-Time Research (QUEST). A sufficiently stable transportable reference frequency standard and the possibility of comparisons to PTB's primary frequency standards are helpful in these activities.

On that account a mobile frequency reference based on a passive hydrogen maser was constructed in PTB. The connection to PTB is established by using GPS PPP as described in Section 2.6.

## 3.2. Equipment

The passive hydrogen maser VCH-1006 manufactured by the Russian company "Vremya-Ch" was chosen. A Maser (Microwave amplification by stimulated emission of radiation) uses dissociated (atomic) hydrogen gas in a microwave cavity and the 1420,405 MHz ground state hyperfine transition. They are available as passive and active devices. In active devices the cavity system oscillates by itself and an electronic circuit is steered to the cavity output signal. A passive maser's cavity system does not oscillate by itself. Instead of that, a 1420,405 MHz interrogation signal is needed to lock a quartz oscillator frequency to the atomic line. Thereby the frequency accuracy is degraded but passive masers could be made smaller and lighter than active devices which are typically not mobile.

In Figure 3.1 PTB's maser room is shown. The four active masers are all manufactured by "Vremya-Ch". The masers H4 and H5 are of the type series VCH-1005

and H6 and H8 are of VCH-1003A. It is clearly visible that these bulky devices cannot be used for mobile applications. Although the commercial caesium clocks are small and portable, they do not fulfill the requirements on the short term stability required for optical frequency measurements.

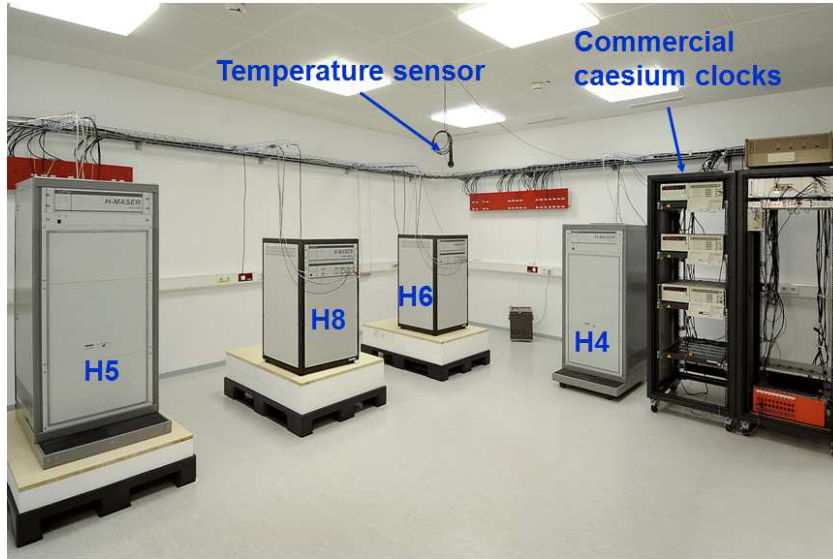


**Figure 3.1.:** PTB's maser room with four active masers and three commercial caesium clocks.

On the left photo in Figure 3.2 the VCH-1006's front view is visible. The device is just a little bit larger than a commercial caesium clock. It weights about 30 kg. With the help of a small keyboard the clock time of the display can be adjusted and the output frequency generated by a digital synthesizer can be changed in relative steps of  $10^{-15}$  within  $10^{-10}$ .

The right photo shows the electrical connections on the back side. Power can be provided both as 220 V AC and 27 V DC, so that a continuous operation can be guaranteed. Via RS232 interface a computer can monitor important operational parameters like molecular hydrogen pressure, ion pump current, and signal level voltages in a fixable interval. In case of any malfunction these parameters are useful to localize the source of the problem. We decided for a normal notebook PC, as it is simply transportable and offers its own uninterrupted power supply due to its accumulator. If it is connected to the internet, other computers can monitor the maser all over the place.

As GPS receiver the Dicom GTR50 time and frequency transfer receiver was chosen (left Photo of Figure 3.3). The receiver module is included in the case of an industrial personal computer that is operating on common Linux system software. It can be controlled by a web interface or directly by connecting monitor, keyboard, and mouse. As depicted in the photo, all connections (1 PPS, antenna)



**Figure 3.2.:** Maser VCH-1006: The left photo shows the front view, the right photo points out the multiplicity of 1 PPS and frequency outputs. The signals can be distributed to the GPS receiver and a measuring system without additional amplifiers.



**Figure 3.3.:** GPS-receiver GTR50 and notebook: The left photo shows the GTR50. The notebook is placed on top receiver on the right photo.

are accessible from the front panel. CGGTTS, L3P, and RINEX files can be created at the same time in adjustable intervals. The main advantage is that the GPS receiver module is heated to a stable operating temperature at  $45^{\circ}\text{C}$ . As antenna the Novatel GPS-702 GG together with a 50 m FSJ1 cable is used.

### 3.3. Performance of the passive Hydrogen Maser

In a first step the passive maser was characterized at PTB by comparing it to different frequency standards. In Figure 3.4 in the left plot the frequency instability in terms of the Allan Deviation of the comparison of the passive maser, denoted

internally as H7, with respect to PTB’s active maser H6 and the primary frequency standard CSF1 is depicted. Precision frequency comparators were used for the comparisons. The caesium fountain CSF1 is currently the frequency source with the best long term stability available at PTB. The frequency instability of H7 is better than  $3 \cdot 10^{-15}$  at one day. Thus, its performance exceeds the manufacturer’s specifications of  $3 \cdot 10^{-15}$  in one day [58].

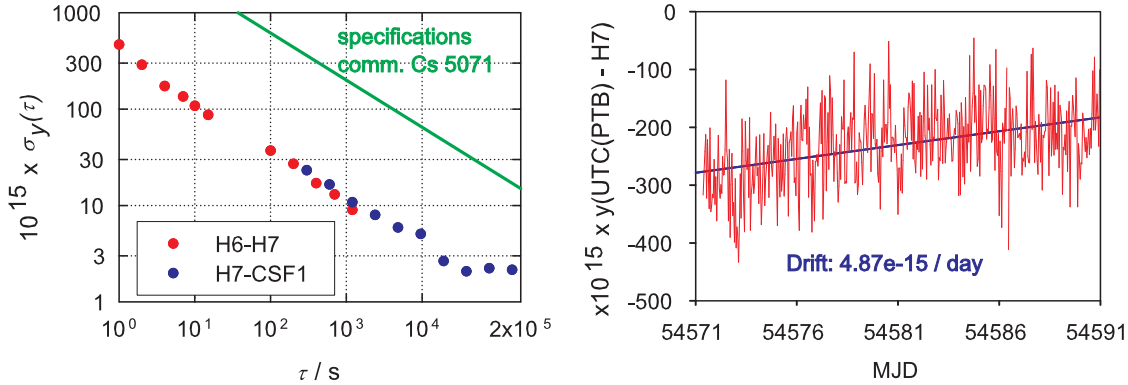


**Figure 3.4.:** Relative frequency instability in terms of the Allan Deviation of the passive maser H7 with respect to an active maser and the primary frequency standard CSF1 (left plot) and comparison of the passive maser with respect to UTC(PTB) (right plot). After an averaging time of  $10^5$  s the instability is limited by the passive maser.

The plot includes the specifications of a commercial caesium clock of type 5071 high performance option, manufactured initially by Hewlett Packard and now by Symmetricom, to demonstrate that the frequency instability of the passive maser is more than one order of magnitude better for short averaging times of less than a few days. A passive maser represents the most stable transportable frequency standard available today. Also in the satellites of the European GNSS system Galileo passive masers will be employed as the local clocks.

The right plot shows a long term comparison of the H7 maser’s 1 PPS output with respect to UTC(PTB) in April and May 2008 for 30 days. The measurement was performed utilizing a time interval counter. UTC(PTB) was derived from the primary standard CS2 that was steered to UTC by an high resolution frequency offset generator. A relative frequency drift of  $4.87 \cdot 10^{-15}/\text{day}$  was observed. Such drifts are typical for masers.

In order to use the maser as a mobile reference, which means that the maser has to be transported in a vehicle, a special mount was constructed that protects the maser against heavy mechanical shocks. The maser is clamped between metal chains which are connected to an outer metal frame with four springs in such a way that the maser can oscillate mechanically inside the outer structure. Handholds

are mounted to the structure to ensure that it can easily be carried by at least two persons. Figure 3.5 shows the construction while it is located in the luggage space of a car. The metal springs are clearly visible.



**Figure 3.5.:** The transportable maser inside the luggage space of a car.

The operation of the maser should never be stopped, otherwise it could take several weeks until the performance of the continuous operation (Figure 3.4) is restored. In Figure 3.5 the rechargeable batteries which provide the maser with 27 V DC are indicated. If the maser is transported with a car it can also be connected to 230 V AC generated from the car's electrical system by a DC to AC converter.

In order to monitor whether the operational parameters of the maser are affected by the transportation or not, the notebook is also operated continuously.

The first test on the transportability of the maser was conducted in 2008. It was taken to the LUH, which is about 70 km away from the PTB. The device was shown there on an exhibition for several hours and then transported back to PTB. Shortly before the transport the frequency was compared to the active maser H5 by a high resolution phase comparator. Measurement values were recorded every second. Directly after the maser returned to PTB this comparison was repeated. The operational parameters were recorded during the complete experiment.

Figure 3.6 shows the relative frequency difference between H7 and H5 before and after the transport. The absolute frequency of the passive maser has changed by  $8.6 \cdot 10^{-14}$ , but the noise after the transport experiment is at the same level as before. Furthermore no abnormality was detected in the operational parameters. Since the maser performance reaches its limit at  $10^4$  s (cf. Figure 3.4) it is sufficient to show only the standard deviation. This shows that the maser can survive a transport without damages, but the monitoring with GPS is essential in order to get the



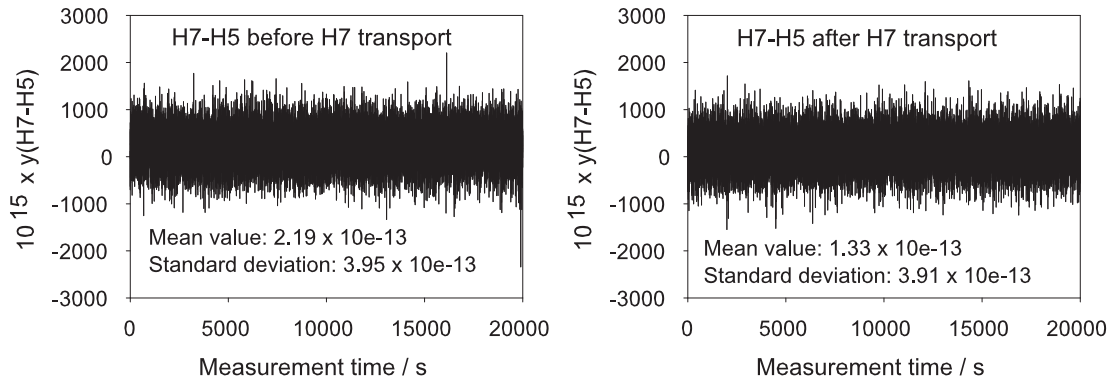


**Figure 3.6.:** Relative frequency differences between H7 and H5 before and after the transport to Hanover.

absolute frequency value at any time, also because of the drift noted in normal operations (Figure 3.4).

### 3.4. Performance of the GTR50 Time and Frequency Transfer Receiver

Since the environmental conditions at a remote location are unknown it is necessary to monitor the maser's frequency output with respect to PTB's frequency standards. For this reason the transportable maser was combined with the Dicom GTR50 time and frequency transfer receiver [59]. This receiver consists of a common industrial computer chassis (Figure 3.3, left photo) and a temperature stabilized box including a Javad GGD 112-T receiver board and a time interval counter card. The GTR50 is designed according to Figure 2.4, but uses state-of-the-art electronic circuits.

If the antenna is connected, the internal 20 MHz oscillator of the GPS board is synchronized to the GPS time and a 1 PPS signal is derived. This 1 PPS signal is compared to an external 1 PPS signal with the internal time interval counter card. The measurement data of the time interval counter and the GPS data are stored on the hard drive of the computer. The data are combined afterwards by a processing software and can be output in the standard CGGTTS [29] and the RINEX [30] format.

The time interval counter uses a new patent-registered technique based on surface acoustic wave (SAW) filters [60], but with less precision than the device described in the reference. The precision of the time interval counter is specified in the manual as  $<50$  ps RMS [59].

Figure 3.7 allows a view inside the temperature stabilized box, housing the receiver board and the time interval counter. The receiver board is clearly identi-

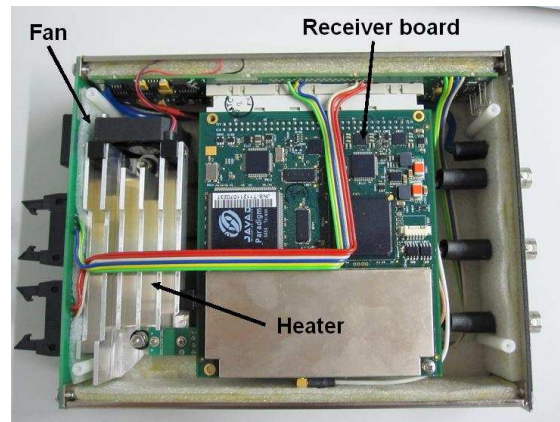


**Figure 3.7.:** A view inside the temperature stabilized box.

able. On the right side the outside signal connectors are visible (cf. Figure 3.3), on the left side two connectors for the RS232 interconnections between the computer and the box are situated. The time interval counter is not visible, because it is located below the receiver board. For a uniform temperature distribution the air inside the box is circulated by a small fan and the heater produces stable conditions of  $45^{\circ}\text{C} \pm 1^{\circ}\text{C}$ . Thus, the performance of the GTR50 receiver is very stable and independent from the environmental conditions. It is thus a well suited receiver for a mobile frequency reference.

The performance of this type of receiver is analyzed in detail in Chapter 4. A relative frequency instability of better than  $10^{-15}$  at one day is possible with two GTR50 receivers in a short baseline common-clock experiment and data evaluation utilizing the PPP method.

### 3.5. Installation of the Frequency Reference at the IQO

The Institute of Quantum Optics (IQO) of the LUH is engaged in developing optical clocks based on neutral magnesium atoms [61]. In addition, an optical fiber link for frequency comparisons based on frequency combs can be operated between IQO and PTB [16]. For both applications, the local frequency comb measurements [62] and the evaluation of the optical fiber, a precise microwave reference frequency is needed at the IQO. For this purpose the highly precise frequency reference was installed at the optical clock laboratory at the IQO.

Figure 3.8 shows the mobile frequency reference at the IQO (left photo) and the antenna on the roof of the IQO's building (right picture).

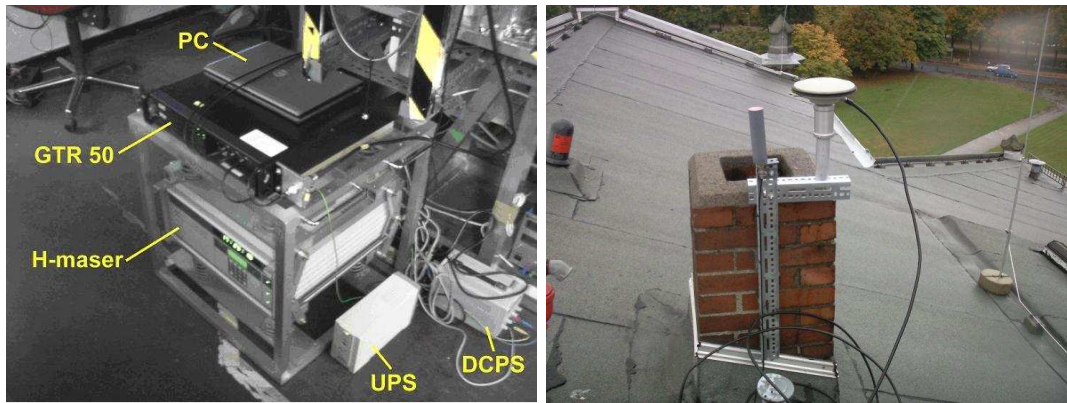


**Figure 3.8.:** The highly precise mobile frequency reference at the optical clock laboratory at the IQO of the LUH and the antenna on the roof of the building.

The maser, the GPS receiver, and the monitoring PC are visible. Additionally, a battery buffered uninterrupted AC power supply (UPS) and a DC power supply (DCPS) are available. The DCPS charges the batteries which provides the maser with 27 V DC (cf. Figure 3.5). These batteries are not visible here.

The antenna is mounted nearby an old chimney together with an other antenna. The plain antenna on the right side is the antenna which is connected to the GTR50 receiver. The old rod antenna on the left side is connected to a GPS disciplined rubidium clock with low precision that was used as the IQO's reference source before the H7 maser was installed.

In Figure 3.9 the relative frequency instability of the comparison of the passive maser at IQO with the active H5 maser at PTB in 2008 is depicted and the results for a local comparison at PTB with a high resolution frequency comparator is shown.

The GPS data were analyzed using the Japanese Concerto C4 software [63]. Details of the software are explained in Chapter 4. The receiver at PTB was also of type GTR50. It was connected to UTC(PTB) and the frequency differences between UTC(PTB) and the H5 maser were additionally measured with a frequency comparator.

The results shown demonstrate that it is possible to provide a highly precise reference frequency at a remote location through a line with two GTR50 that can be referenced to PTB's masers exceeding an averaging time of  $10^4$  s. Up to this averaging time the results are dominated by white noise of the GPS measurement. For longer averaging times the instability is completely governed by that of the passive maser.

It has to be outlined, that such a frequency connection can also be done with institutes that operate their own equipment. Figure 3.10 shows the frequency

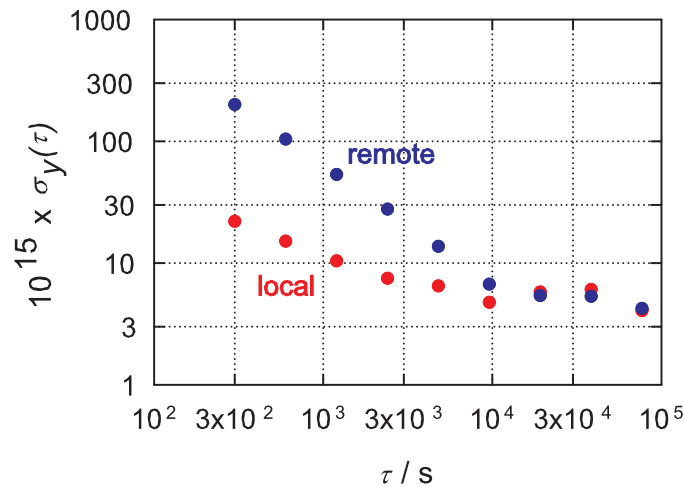


**Figure 3.9.:** Relative frequency instability of the comparisons of the mobile maser to an active maser at PTB (red dots) and with GPS PPP between PTB and LUH (blue dots).

instability of a comparison of an active maser at the Max-Planck Institute for Quantum Optics (MPQ) in Garching with an active maser at PTB.

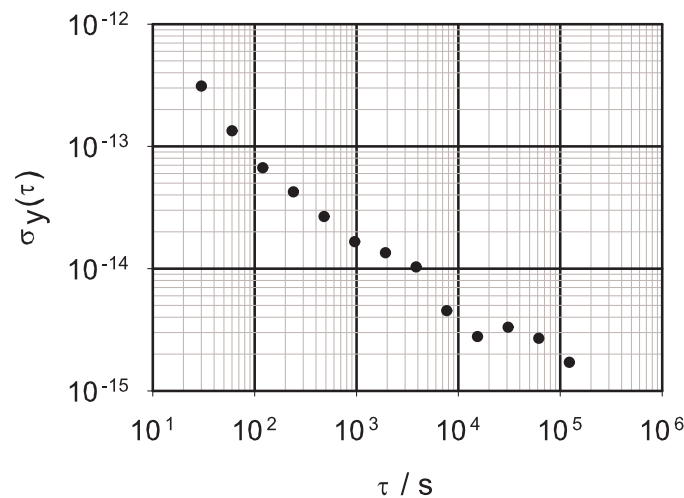


**Figure 3.10.:** Relative frequency instability of the comparison of active masers located at MPQ and PTB with GPS PPP.

The MPQ operates its own active maser and its own GPS receiver of type Septentrio PolaRx. The comparison to PTB is easily established just by exchanging RINEX data with PTB. At PTB an Ashtech Z12-T receiver was used. The PolaRx and the Ashtech receiver are designed according to Figure 2.5 and are not limited by the performance of a time interval counter in the short term (see Chap-

---

ter 5). The data were evaluated at PTB using the PPP method (NRCan software package, see Chapter 4). The results demonstrate that also on a 400 km baseline GPS PPP frequency comparisons are capable to reference maser frequency standards to PTB's standards at averaging times of  $10^4$  s. Since two active masers are compared, the instability is one order of magnitude better for averaging times of more than  $10^4$  s.

## 4. Software Assessment

Different software packages for the PPP analysis of GPS data are available. In this Chapter some of these packages, which are used in time and frequency laboratories, are analyzed in view of their capabilities for time and frequency comparisons.

In the first Section the results of two software packages, namely the NRCan-PPP software [15] and the Concerto C4 software package [63] are compared in common-clock zero baseline experiments. While the former package was originally developed for geodetic applications, including the processing of carrier-phase data of dynamic (moving) receivers, the latter is especially designed for time and frequency comparisons.

The NRCan-PPP software is of particular importance, because it is used by the BIPM for the evaluation of the links contributing to UTC with carrier-phase data [64]. To enable high precision processing of the data of a receiver on a moving platform it is based on a Kalman filter [26]. In the Section 4.2 it is outlined that special care has to be taken when data which are affected by corrupted measurement data are evaluated with this software package.

In Section 4.3 five different software packages have been analyzed in view of all relevant parameters which have to be estimated by a PPP software package. Not only the clock solution, but also other estimated parameters like positions and zenith tropospheric zenith path delay estimates are compared in order to find the software that is most suitable for time transfer. Especially the repeatability of the position could be a good indicator for quality. Dicom GTR50 time and frequency transfer receivers connected to local time scales in different laboratories were used.

In Section 4.4 a simple algorithm developed at PTB, which uses only the carrier-phase measurements is introduced. The results of frequency comparisons on baselines with different lengths are compared to the solutions of the NRCan-PPP software and the influence of the correction models is analyzed.

The results of the studies presented in this Chapter have already been partially published in the references [65, 66].

### 4.1. Common-Clock quasi zero Baseline Experiments

In this study two different software packages are used, the NRCan-PPP software [15] and the Concerto software package developed at the Japanese National

Institute of Information and Communications Technology (NICT) [63] which maintains Japan's timescale UTC(NICT). The NRCan-PPP software was originally designed for geodetic needs. Therefore it uses a Kalman-Filter, because this is the way to enable high precision processing of data of a receiver in motion. The NICT C4 software is especially developed for time and frequency transfer and uses a simpler least squares estimation algorithm.

If a PPP process is started, the ambiguities of all satellites have to be initially estimated. Since the RINEX data are usually recorded on a daily basis and the ambiguities are estimated with the help of the P3-code, a phase discontinuity between two consecutive days occurs. This problem is well known as the so-called day boundary problem [67]. Both the NRCan and the C4 software package are of special relevance for time and frequency comparisons, because they allow to use processing information of the previous day as input for the actual processed day. In NRCan-PPP the phase jumps are removed by adopting a file which is called the "final normal equation of the Kalman-Filter" of the previous day to the actual processed day (cf. Figure 2.8). The C4 software simply restores the ambiguity in a file that is employed by the actual process. This update was implemented in summer 2008 while the developer, Tadahiro Gotoh from NICT, was staying at PTB as a guest researcher [68].

As depicted in Figure 4.1 the solution of the NRCan-PPP shows transient oscillations in the beginning. This is typical for a Kalman-Filter [26]. For this reason there is also the option of using a backward smoothed solution. By concatenating multiple RINEX files, a multi-day batch solution is possible with this software.

In Figure 4.1 and in the following the time differences as the integral quantity of the frequency are plotted, since this allows for a better detection of irregularities.

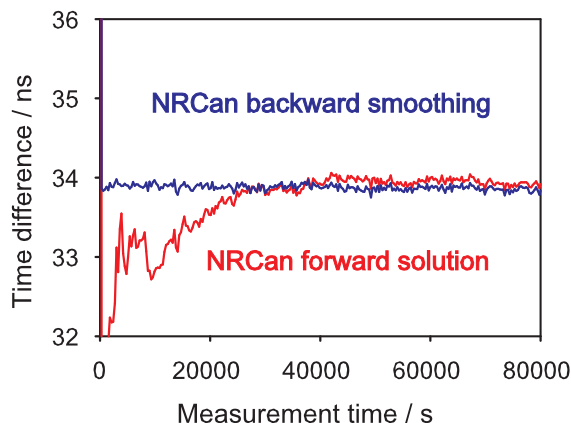


**Figure 4.1.:** One day comparison of two GTR50 receivers in a common-clock quasi zero baseline setup with NRCan-PPP. The forward solution shows initially transient oscillations. Since no calibration of the receivers has been made, the offset is about 34 ns.

As shown in Figure 4.1 the forward solution and the backward smoothing converge not until half a day. Because of that the forward solution is just useful if the processing time is longer than one day and the first days can be neglected.

In Figure 4.2 the relative frequency instability of the comparison of two receivers in a common clock quasi zero baseline setup (the antenna positions differ only by a few meters) is shown.

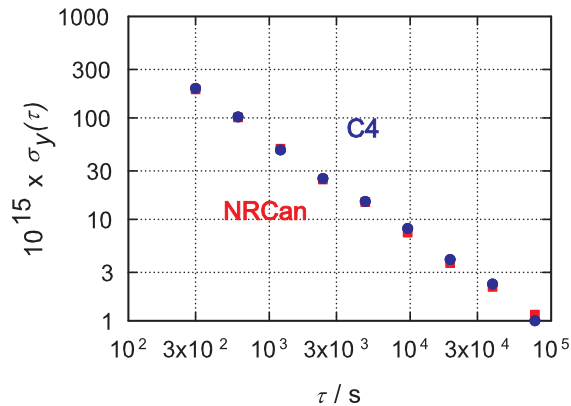


**Figure 4.2.:** Relative frequency instability of comparison of two GTR50 receivers obtained with NICT C4 (blue dots) and NRCan-PPP (red squares) results.

Because the 30 second measurement data were taken from a longer period ranging from MJD 54713 to 54732 and the first day is neglected, the NRCan-PPP backward and forward solution give exactly the same result and can thus not be discriminated in Figure 4.2. From the Allan deviation comparison between the NRCan-PPP and the C4 solution it is not possible to decide which software concept is better and should be preferred. For this reason further examinations are needed. But the results demonstrate that it is possible to compare frequencies with an uncertainty level of  $10^{-15}$  at an averaging time of about one day with both software concepts and GTR50 receivers.

The solutions provided by the two software concepts sometimes show a small divergence. In Figure 4.3 a cutout from a longer data batch is plotted. This divergence is typical, a difference larger than 400 ps has not been observed in different proper data records from different receivers. Normally this divergence will increase after three months of continuous processing, because then the results of the Kalman-Filter are no longer reliable, as specified by the developer [69]. Unfortunately there are not yet such long data records with continuous phase measurements and without any gap available. If there is one small gap in the data both software concepts restart the processing, which means resetting of all ambiguities.



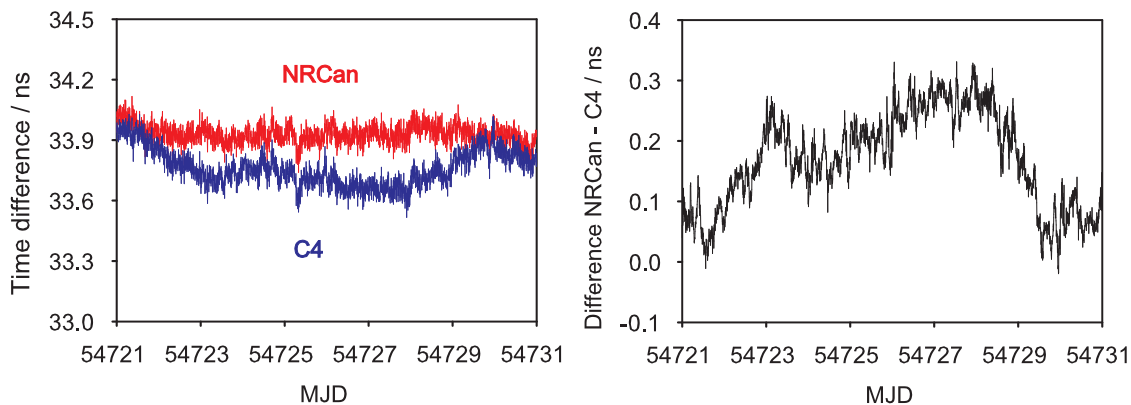


**Figure 4.3.:** Cutout from a longer period with typical divergence between C4 and NRCan-PPP common clock zero baseline solution. The receivers have not been calibrated, the offset is about 34 ns.

The maximum difference ( $\approx 0.3$  ns) between the two solutions show that the numerical processes have an influence on the results. Effects due to different correction models are equal for both receivers in the quasi zero baseline common-clock setup and cancel out. In Chapter 6 the calibration of operational TAI links, which are evaluated by the BIPM with the PPP method, using common-clock differences on both sites are demonstrated. The software comparison depicted in Figure 4.3 shows that the usage of exactly the same software which is used for the evaluation of the operational links is mandatory for the calibration, in order to accomplish a calibration with an uncertainty at the nanosecond level.

## 4.2. Discontinuous measurement data and drifts

Until now continuous measurement data were used, that means that the 30 s code and phase measurement taken from both receivers without interruption are processed over the complete period. Gaps in the measurement data make for disrupting the processing and the ambiguities are reset. It is a well known fact that this causes phase jumps of up to 1 ns in the results [67]. However, it is an interesting question how the different numerical concepts are responsive to corrupted measurement data.

To find this out a 25 day data batch of a common clock experiment with two GTR50s was processed. Due to experiments with the receivers and the receiver software, the measurement was interrupted in average every 2 hours during the first 7 days (Figure 4.4).

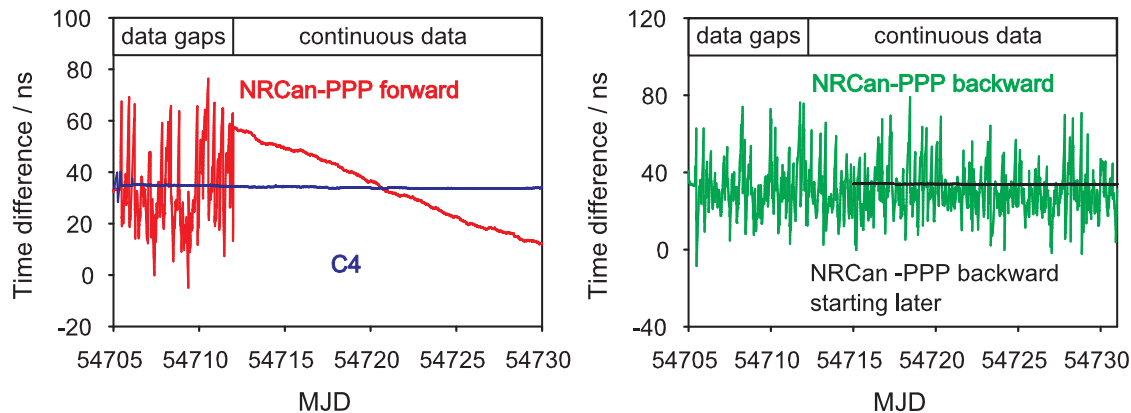


**Figure 4.4.:** A 25 day data batch with corrupted measurements in the first 7 days processed with C4 and the two NRCan-PPP options. The receivers have not been calibrated.

As expected the NRCan-PPP Kalman-filter has to engage very often and this makes the solution very noisy. Surprisingly the Kalman-Filter does not engage correctly in the period with continuous measurement data and produces an oscillation on a larger scale. In backward smoothed solution the noise is carried forward to the time interval with continuous measurement. However, if the starting point is located in the time interval with good measurement data it equals the C4 solution up to 300 ps. In contrast, the C4 software is much more resistant against corrupted measurement data. Corrupted data means that these data are not gathered in routine laboratory conditions.

RINEX data which are suspected to be affected by measurement interruptions and are processed with a Kalman filter based software should always be checked with a second software package, e.g. the Japanese C4.

In Figure 4.5 a Septentrio PolaRx receiver was compared to a GTR50 in a common clock experiment. The clock signals were provided by different pulse and frequency distribution amplifiers and the cables were a few 10 meters long. This apparently caused a phase drift between the two signals to be compared of order 1 ns during the 9 days. Figure 4.5 shows that the slope of the solutions depends on the starting point. It is thus not determinable which solution represents the real slope for a given day. Comparing the red and blue plotted data for the days 3 to 7, respectively, the slopes differ from  $1.6 \cdot 10^{-15}$  in four days for the blue data and  $10^{-15}$  in 4 days for the red ones. This effect has only been found in the backward smoothed solution of the NRCan-PPP software.

It has to be noted here that the BIPM uses 30 day batches of RINEX data and the NRCan backward smoothed solution to evaluate the links for the TAI computation. To find out whether the effect presented before influences the solutions in case of timescale comparisons it is necessary to compare data on long baselines.

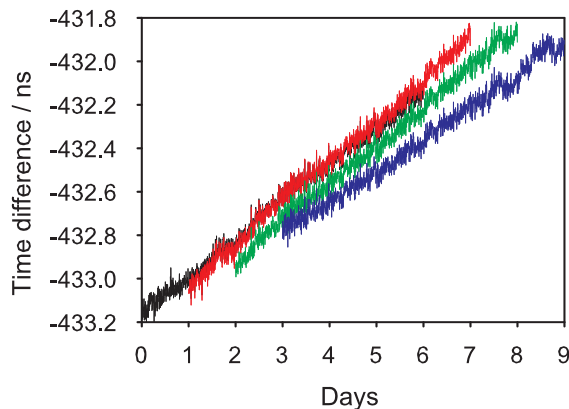


**Figure 4.5.:** The NRCan-PPP backward 6 day smoothed solutions starting one day displaced from each other.

### 4.3. Clock comparisons and PPP parameters

Common-clock experiments in a short baseline setup are important for assessing the general limitations of the measurement process and the data processing strategies. However, figuring out the performance of the PPP software in case of long baseline time comparisons is very important, because in this case the influence of the different correction models used in the different software concepts does not cancel out.

Figure 4.6 shows the timescale comparison UTC(ROA) and UTC(TP) (TP denotes Tempus Pragense) of the Royal Spanish Naval Observatory (ROA) and the Czech Institute of Photonics and Electronics (UFE), respectively. On all sites GTR50s are connected to the local realizations of UTC derived from commercial cesium clocks. IGS rapid clock and ephemeris data were used, but no Earth rotation parameters and ocean loading coefficients (cf. Section 2.5). The standard deviation of the differences between NRCan-PPP and C4 results is 0.275 ns.

The effects induced by the correction models make an impact. This is the so-called "software noise" and depicted in the plot on the right handed side of Figure 4.6. It exceeds the variations shown in Figure 4.3 and the effect demonstrated in Figure 4.5.

One cannot distinguish which of the two solutions is closer to the reality. Thus, the NRCan-PPP and the C4 software package are compared to three other software packages which are used within the timing community in a more detailed analysis.

#### 4.3.1. Software and Experimental Setup

For this analysis data of three Dicom GTR50 time and frequency transfer receivers located at PTB, at NICT, and at ROA, have been used. The 1 PPS inputs of

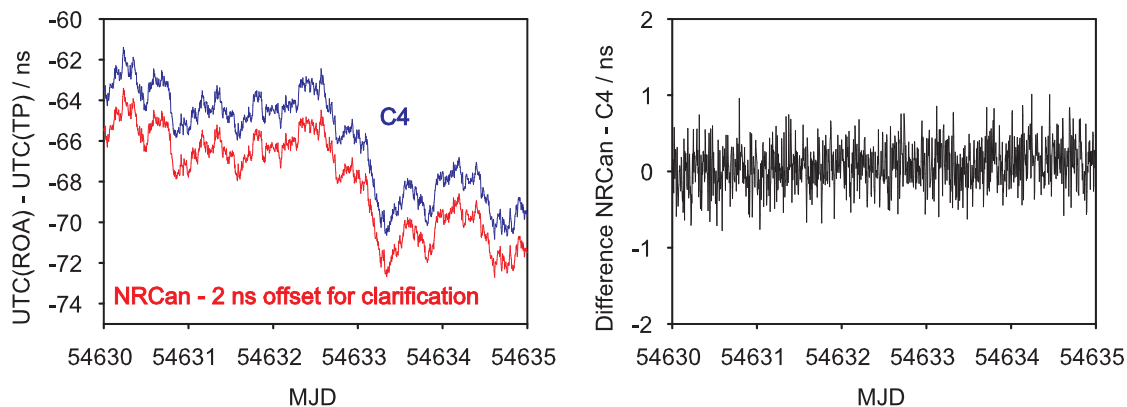


**Figure 4.6.:** Takeout from a longer measurement ranging from MJD 54584 to 54648 between ROA and UFE. The results are on a 5 min. basis. This data are by courtesy of ROA and UFE.

these receivers were connected to the local UTC realizations (Table 4.1). The initial position is the position that is known before the analysis and stored in the receivers for the computation of the CGGTTS data.

**Table 4.1.:** Initial positions of the stations and timescale input.

Station	Initial position	1 PPS input
PTB	$x = 3844056.75$ m	UTC(PTB): Steered primary clock CS2
	$y = 709664.09$ m	
	$z = 5023131.73$ m	
NICT	$x = -3942087.86$ m	UTC(NICT): Active H-Maser steered by clock ensemble
	$y = 3368252.55$ m	
	$z = 3702001.32$ m	
ROA	$x = 5105511.68$ m	UTC(ROA): Steered Cs 5071 A
	$y = -555187.02$ m	
	$z = 3769791.71$ m	

Five different software packages along with IGS final orbit and clock products and ocean loading coefficients from the GOT002 model [41] were used. The packages require different IGS input data due to different interpolation processes (Table 4.2). For instance, the NRCAN-PPP software uses Chebychev Polynomials for the interpolation of the satellite orbits [69]. This interpolation method is more stable around the end points of the data set than others, so that only the IGS orbit file of the processed day (pd) is needed. Furthermore the data are processed directly

**Table 4.2.:** Available software packages and required IGS input. pd denotes processed day, -pd and +pd denote the previous day and the next day, respectively. -6h and +6h denotes 6 hours data of the previous and the next day, respectively.

Software	Algorithm	File input
Atomium [31] PPP	Least square estimation	pd RINEX, -1d, pd, +1d orbit, clock and earth rotation IGS data
NRCAN PPP [15] (static mode)	Kalman filter	pd RINEX, pd clock and orbit, no earth rotation
GIPSY 5.0 [70]	Kalman filter	pd RINEX, -1d, pd, +1d orbit, clock and earth rotation
Bernese GPS Software 5.0 [71]	Least square estimation	pd RINEX, -1d, pd, +1d orbit, clock and earth rotation
NICT C4 [63]	Least square estimation	-6h, pd, +6h RINEX -1d, pd, +1d orbit and clock, -2d, -1d, pd, +1d, +2d earth rotation

in the ECEF system, so that there is no need for Earth rotation parameters (cf. Section 2.5).

The C4 software uses an overlapping process, so that also RINEX data of 6 hours of the day before (-6h) and 6 hours of the day after (+6h) the processed day are needed. This software is currently available in two versions: An older version with some bugs related to outlier rejection and correlation avoidance between parameters, and a new optimized version, but C4 is still in an experimental status. For reasons of comparability, the feature of continuous processing without resetting the ambiguities has not been used for this analysis.

The GIPSY 5.0 and the Bernese GPS software packages are commercial products. The analysis of the data with these packages was done by Héctor Esteban at ROA and Ulrich Weinbach at IfE at LUH, respectively, as PTB does not own the respective software licenses. The Bernese software is similar to the software, which is used by the Center for Orbit Determination in Europe (CODE), an IGS analysis center, for generating its network contribution to the IGS products.

The Atomium software was developed at the Royal Belgian Observatory (ORB) especially for time and frequency comparisons. Similar to the C4 software it uses a least-square estimation algorithm, but it does not have the capability to remove the daily phase discontinuity due to the beginning of a new file each day.

### 4.3.2. Time Scale Comparisons

Two time scale comparisons were made, one for the intercontinental baseline PTB-NICT (8333 km) and the other for the European baseline PTB-ROA (2182 km) with all available software packages. To avoid inconsistencies due to data gaps and receiver problems, a period for data computation was selected where all three receivers were operating normally. A maximum divergence of about 2 ns between C4 and the other solutions (Figure 4.7) is visible.

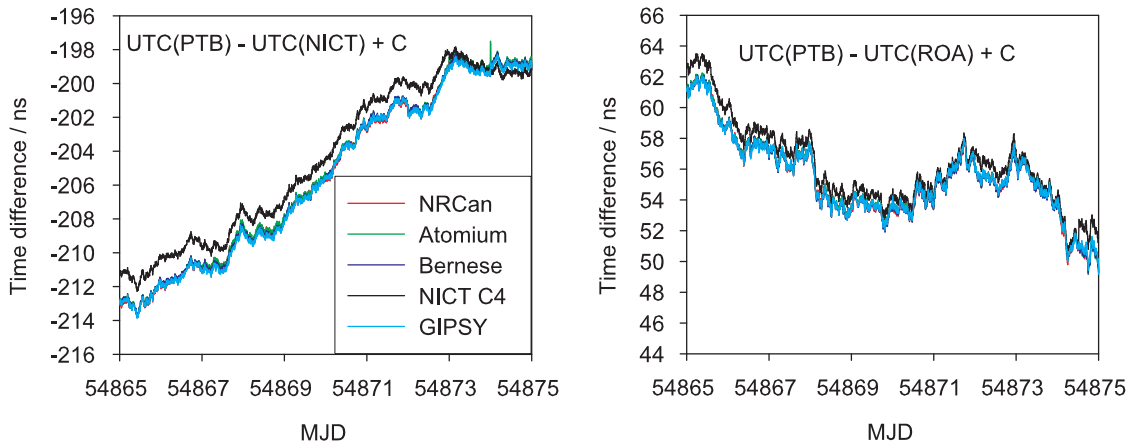


**Figure 4.7.:** Time scale comparison: The GTR50 receiver at PTB has not been calibrated. C denotes an additional calibration constant that depends on the cable and internal delays. The color assignment to the different software packages on the left plot is the same as on the right plot.

In this picture one can hardly distinguish between the packages of the NRCan, Atomium, Bernese, and GIPSY software. The divergence of the C4 solution gives just a first indication that it has some shortcomings.

To cancel the clock noise, it was decided to use the NRCan solution as common reference and compare all other solutions to it (Figure 4.8). A good agreement of Atomium, Bernese, and GIPSY solution with NRCan of less than  $\pm 350$  ps is visible. The ambiguity estimates seem to be similar in these four packages, in consequence no significant jumps occur in the double difference data. Since all correction data were applied to the software packages, the double differences are less noisy compared to the analysis depicted in Figure 4.6. The C4 solution shows mostly an agreement of

about 1.5 ns with NRCan. Clearly, the ambiguities are solved differently, because significant jumps with respect to the other solutions occur in case of both links. A drift with respect to the other solutions is also visible in the PTB-ROA link. However, such drifts occur only if the solutions are calculated on a daily basis, as done in the framework of this study. If the feature of continuous time transfer without resetting the ambiguities is used, these drifts are marginal (cf. Figure 4.6).

Besides the evaluation of the agreement of the GPS solutions with each other, the study of systematic deviations with respect to other techniques or an available ground truth is important. For this reason the solutions of the PPP software packages have been compared to the data of the operational TWSTFT links, which are operated between the institutes in parallel. The TWSTFT data are usually measured in 2 hour intervals. Since the data of the IGS clock products are in 5 min intervals, the output of the PPP software packages is also spaced in 5 min intervals. The GPSPPP data were thus compared to values calculated by a linear interpolation between two adjacent TWSTFT measurements.

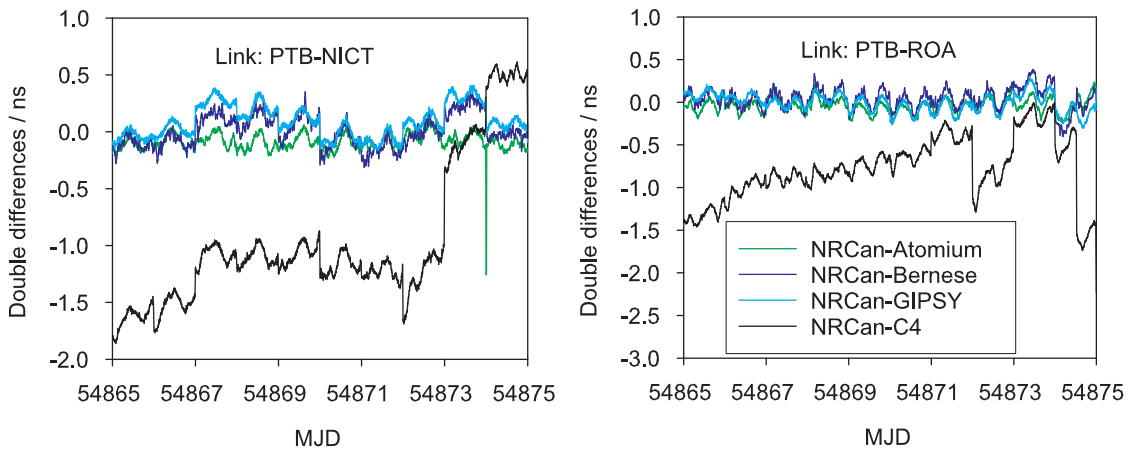


**Figure 4.8.:** Double time differences NRCan – other software solutions. The color assignment to the different solutions on the left plot is the same as on the right plot.

However, TWSTFT is not very helpful for this purpose, because of the noise of the TWSTFT observations one does not get more information than from Figure 4.8, as shown in Figure 4.9 exemplarily for the link between PTB and ROA. Since the GTR50 receiver at PTB has not been calibrated before this experiment the mean offset of about -15 ns occurs in the double difference solution.

It has to be noted here that the NRCan-PPP software package includes the feature of satellite clock interpolation. This increases the noise level but enables creating output data with the same data spacing as the input RINEX data. This feature is also included in some other software packages, e.g. Bernese, but not in

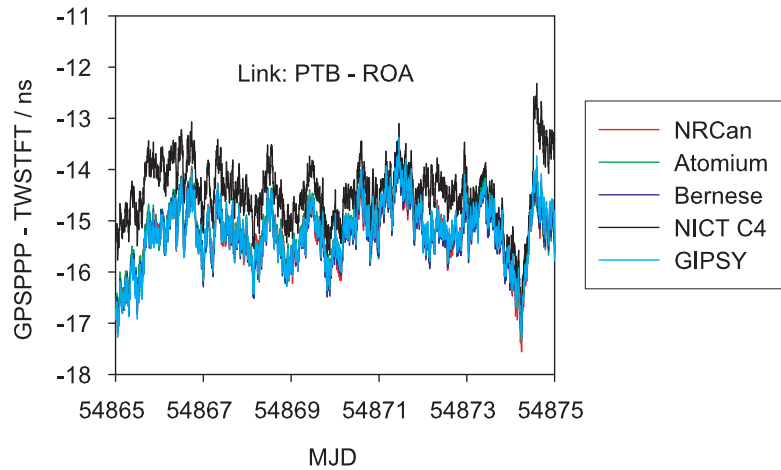


**Figure 4.9.:** Comparison of GPS PPP with TWSTFT, exemplarily for the link PTB-ROA.

all packages analyzed here. Thus it was not used within this analysis, because all packages are to be compared at the same level.

### 4.3.3. Position Estimates

Another way to assess the reliability of the PPP clock solution is the comparison of the position estimates, because position and clock offset have to be solved simultaneously. A good indicator for the quality of the software is the repeatability of the estimated positions, because the antennas of time and frequency transfer receivers are fixed and no significant movement happens within 10 days.

To separate effects related to the vertical and the horizontal position, the position estimates have to be known in the ellipsoidal coordinate system (A.3). Unfortunately some packages output the results only in Cartesian coordinates. To compare all software at the same level, the output of all packages was set to Cartesian coordinates and the conversion was done afterwards. For visualization and simplification the differences of the estimated values are calculated with respect to the initial position (Table 4.1) on a daily basis.

In a first step (Figure 4.10) the distance between the estimated position vector and the initial position vector is calculated:

$$\delta r = |\vec{r}(\text{estimated}) - \vec{r}(\text{initial})| . \quad (4.1)$$

If the initial positions would be known to be true, it would be an estimation for the absolute positioning error of the software. Unfortunately the 3 GTR50s are not IGS stations, so that the initial positions cannot be taken from the IGS data, and the positions might have changed over the years after they were estimated with



other geodetic methods. Furthermore, the dates of the estimation of the initial coordinates are not traceable for the three laboratories and the related realization of the coordinate system was unknown. Since in reality the true position is unknown, the expression (4.1) can just serve as a relative error estimation, i.e. it can show if a software gives repeatable results.

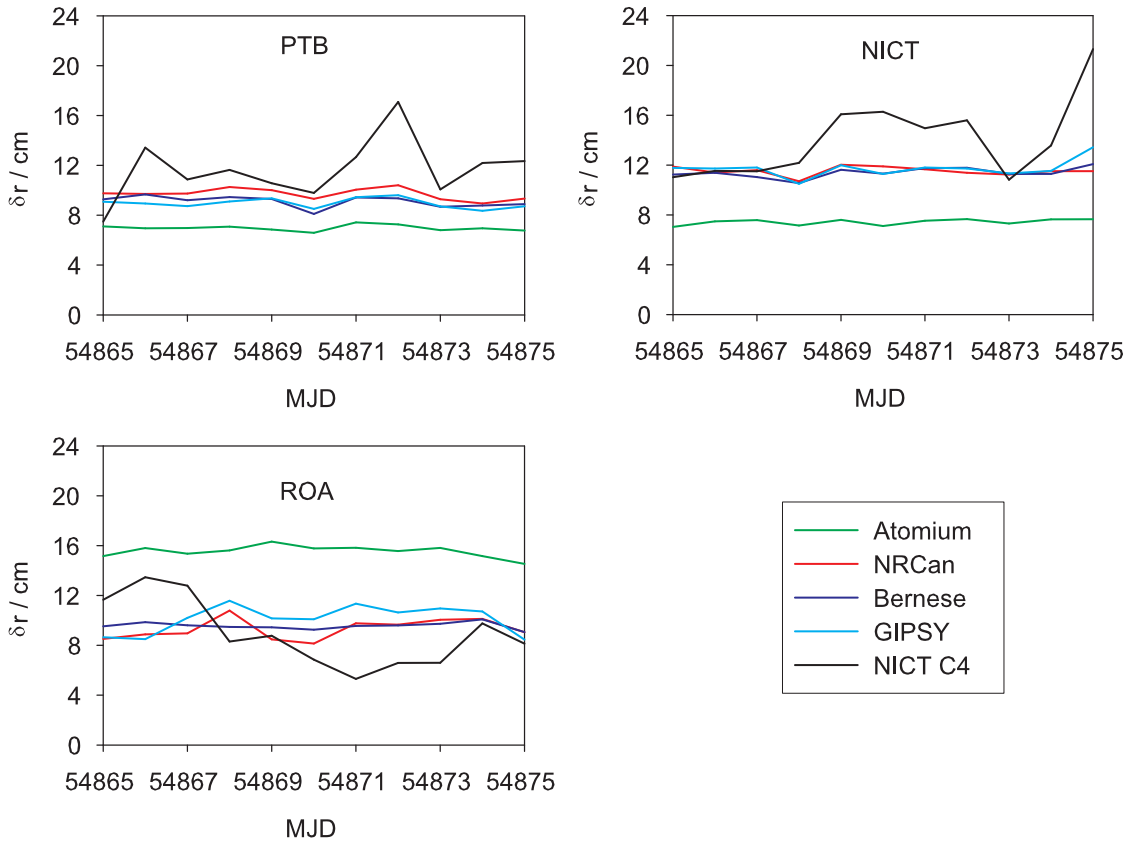


**Figure 4.10.:** Divergence of the estimated position with respect to the initial position. The output of all packages is a daily position estimate.

The NRCAN, GIPSY and Bernese solution are in close agreement, but show variations which are different for each site. It is noticeable that the agreement is best at the location NICT, while it is worst at ROA. This indicates a relationship between the quality of the position estimates and the instability of the external frequency. The average offset of about 9 cm is probably due to the fact that the initial positions are given in an older realization of the ITRF or in the WGS. Since this was unknown, no transformation (A.5) was used.

The position estimates of the C4 software show a very unstable characteristic for all the 3 stations (Figure 4.10). This affects the estimated clock offset in a similar way. The Atomium solution diverges from the other solutions by 2 cm to 4 cm, but

it is very stable. If these divergence would be the same at each location, the time comparison solution would not be affected since a consistent error cancels out.

As depicted in Figure 4.11, most of the position variations of the solutions show up in the height estimate, while latitude and longitude differ only by a few centimeters from each other. The Atomium position estimates show a consistent deviation in the height component for all three sites.

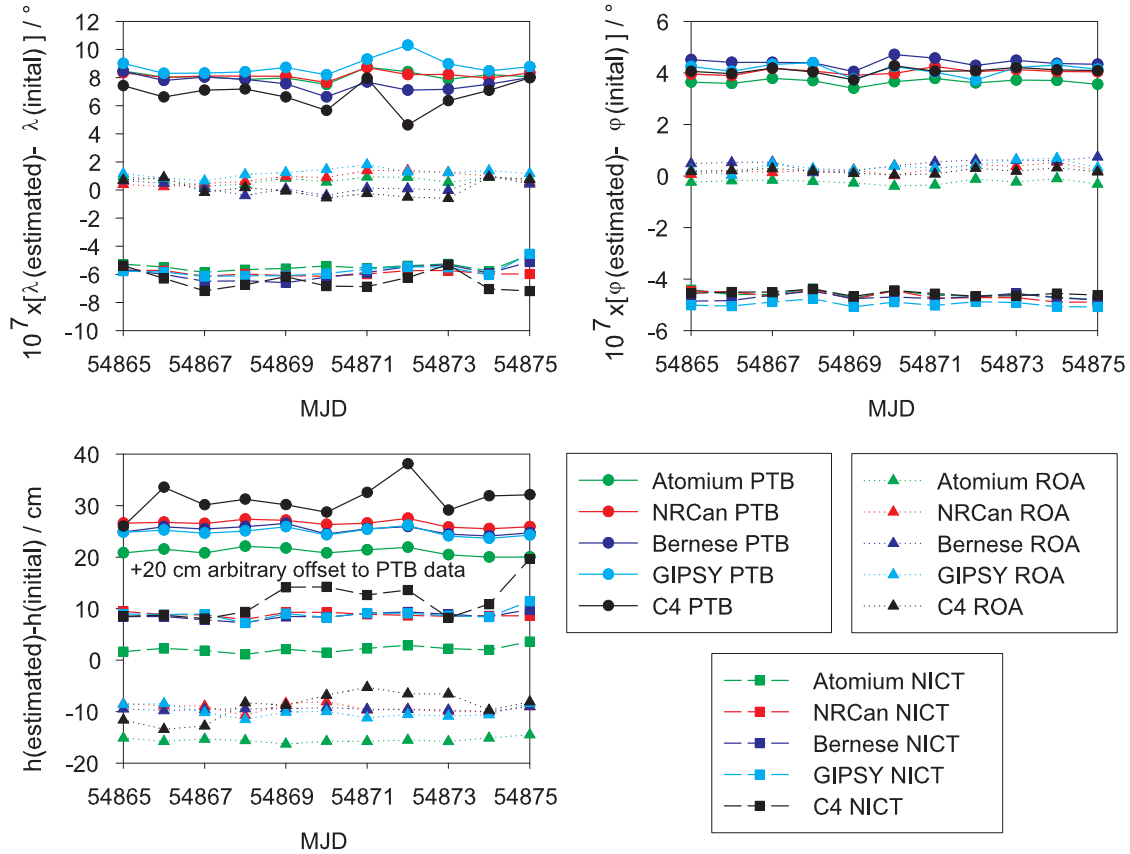


**Figure 4.11.:** Divergence of the estimated position with respect to the initial position in ellipsoidal coordinates.  $\lambda$ ,  $\varphi$ , and  $h$  are geodetic latitude, longitude, and height, respectively. Dots represent the results for the station PTB, squares for NICT, triangles for ROA.  $10^{-7} ^\circ$  equals approximately 1.1 cm. An arbitrary offset of 20 cm is applied to the PTB height data for better visibility.

#### 4.3.4. Troposphere Zenith Path Delay Estimates

The signal delay induced by the troposphere is of the order of more than 2 meters, which equals more than 6 ns. It has to be modeled and estimated [4,5,32] and the

models depend on the coordinates of the station. It is one of the most important error sources for time scale comparisons over long baselines. A wrong estimation leads directly to an offset of the clock estimation. As mentioned in Chapter 2, the common way to model the troposphere is to use one model for the dry part, an other one for the wet part of the troposphere zenith path delay (zpd) [4]. The estimation strategies are different in the software concepts (Table 4.3). The Kalman-Filter based software estimates a new value as often as a clock offset is estimated. In the Bernese solution a zpd is estimated every 30 minutes and in the Atomium and C4 solutions every 2 h. The estimated corrections are applied to the solution algorithm by mapping functions.

**Table 4.3.:** Zenith path delay estimation in the different software concepts.

<b>Software</b>	<b>zpd output</b>
Atomium PPP	every 2h wet part estimation, dry part extracted by Saastamoinen model
NRCan PPP (static mode)	every 5 minutes modified Hopfield model
GIPSY 5.0	Every 5 minutes
Bernese GPS Software 5.0 [71]	Every 30 minutes
NICT C4 [63]	every 2h wet part estimation dry part extracted by Saastamoinen model from initial position

The zpd estimates are in close agreement at all stations for all software concepts, except C4, which shows significant differences from the other packages (Figure 4.12) in the solutions at PTB and NICT. However, a correlation between the obvious errors in the time and position estimates and the zpd estimates is not identifiable.

In contrast to the position estimates the zpd estimates show variations at the same level for the stations NICT and ROA. The solution for PTB is very stable. A relation between the instability of the reference frequency and the resulting zpd is thus not possible. Probably, the characteristics of the zpd estimates depends on the geographic location of the station. PTB is the station which is farthest in the North.

Further research on the correlation between reference frequency, geographic location, position estimates, and zpd estimates is necessary.

Since the parameters estimated by the NRCan-PPP software package, clock offset, position, and zenith path delay are in good agreement with the estimates of

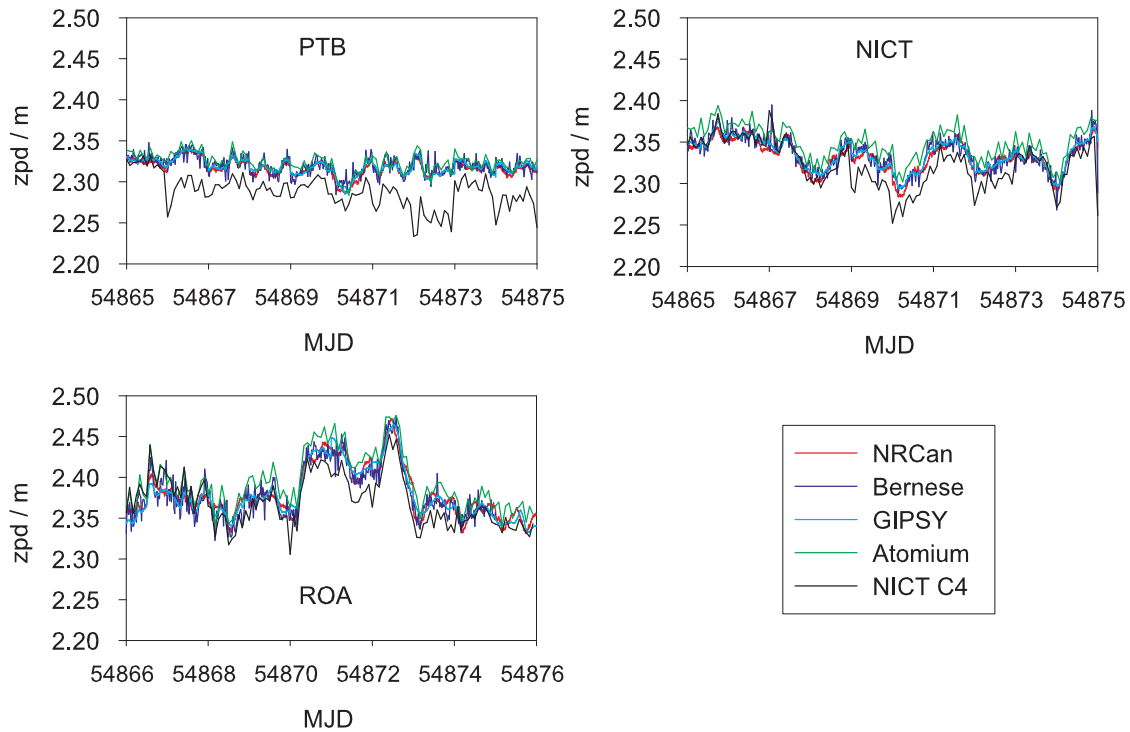


**Figure 4.12.:** Zenith path delay estimates.

the two renowned commercial software packages, it can be considered as a reliable tool for PPP based remote time and frequency comparisons.

#### 4.4. Code free Carrier-Phase Frequency Comparisons

The main parameters that are estimated by a PPP software are highly correlated. The position and troposphere estimates are closely joint by the equations (2.11) and (2.13). An error in the position estimates leads to an error in the position estimates and vice versa, as demonstrated above. Both errors can feed back on each other and influence the troposphere zenith path delay estimates. Clock, troposphere, and position estimates can not be separated. In case of positioning the error can be reduced by a long averaging time, but in terms of time and frequency comparisons a clock solution at each epoch is desired to enable the characterization of the involved frequency standards also at short averaging time.

By definition, PPP is an AV process. Potential benefits of CV on short baselines are excluded. Furthermore, both code and phase measurements are involved and the noise of the code partially migrates to the combined solution, e.g. if the receiver

looses the tracking of all satellites and the ambiguities are reset (Figure 2.8). A jump in the phase domain generates an outlier in the frequency domain.

As demonstrated before, the results of the PPP software packages are influenced by the solution strategy for the linearized observation equations. Thus, it would be desirable to have a method which allows to compare remote frequency standards without linearization. The goal of the work presented subsequently was to reach the same instability level as with PPP, but with a minimum complexity.

#### 4.4.1. Description of the Method

In order to accomplish this and to enable a detailed analysis of the correction models the author has developed a simple method which allows comparing the frequencies of signals connected to two receivers by using only the carrier-phase measurements in AV as well as in CV mode. Fixed positions are used, as in code based time transfer, and the equation (2.13) is solved for the receiver clock  $\delta t_r$ , analog to the solution performed by time and frequency transfer receivers' internal software or the RINEX2CGGTTS software [31]. However, the satellites' clocks and ephemeris data are taken from IGS data and not from the navigation message. Beyond this only corrections for the troposphere and the site displacement due to the gravitational potential of the moon and the sun were used.

The approach described above is of course only possible if the phase measurements are close to the code based pseudorange measurement within several tens of nanoseconds, which means that the receiver provides a kind of pre-solution for the ambiguities. Otherwise the Sagnac correction (2.19) and the elevation (A.8), and thus the troposphere correction, cannot be solved with adequate accuracy. In some time and frequency transfer receivers, e.g. GTR50, a pre-solution of the ambiguities is performed. This can easily be verified by multiplying the carrier-phase measurement of one satellite at one epoch on one of the two frequencies taken from the RINEX data with the corresponding wavelength and checking that this product is in quite good agreement with one of the three code-based pseudoranges (C/A, P1, P3).

In a first step the time difference between a GTR50 receiver's reference clock and the IGS timescale was calculated for one satellite. The receiver was located at PTB and the reference signal was UTC(PTB) derived from the primary frequency standard CS2. The data were taken from the standard daily 30 s RINEX file. The satellite's clock and ephemeris data were extracted from IGS final products. The fixed antenna position was calculated before with the NRCan-PPP software using exactly the same input data in order to ensure the consistency of the reference frame.

To get the position of the satellite at the desired epoch from the 15 min IGS ephemeris file Lagrange polynomials (2.22) of the order 9. To account for the signal propagation delay the time of signal emission was estimated by  $t_s = t_r - L3/c$ , where

$t_r$  is the time of signal reception, related to the timestamps of the RINEX data.  $L3$  is the quantity of equation (2.13) and  $c$  denotes the speed of light in vacuum. The satellite clock offset with respect to the IGS timescale was not applied in this step.

The Sagnac effect was taken into account by rotating the interpolated satellite position  $\vec{r}_{s,\text{Sagnac}}$  around the  $z$ -axis in the ECEF coordinates:

$$\vec{r}_{s,\text{Sagnac}} = \begin{pmatrix} \cos(\alpha) & \sin(\alpha) & 0 \\ -\sin(\alpha) & \cos(\alpha) & 0 \\ 0 & 0 & 1 \end{pmatrix} \vec{r}_s. \quad (4.2)$$

The rotation angle is defined by  $\alpha = -\omega_E L3/c$ , where  $\omega_E = 7.29215 \cdot 10^{-5}/\text{s}$  is the angular velocity of the Earth. If the trigonometric functions are approximated by  $\sin(\alpha) \approx \alpha$  and  $\cos(\alpha) \approx 1$ , the analogy to (F.39) and (2.19) becomes apparent.

The satellite's velocity for the eccentricity correction (2.18) was obtained via equation (2.21) by shifting  $t_s$  by 0.1 ms and interpolating the satellite position from the IGS ephemeris file.

The elevation was calculated according to the equations (A.6) and (A.8) and the troposphere was corrected by applying the model (2.10).

The result is depicted in Figure 4.13 with 5 min spacing due to the 5 min spacing of the IGS clock file. In order to clarify the difference between the phase and the code measurement the process described above was also done using the P3-code (2.11) instead of  $L3$ .

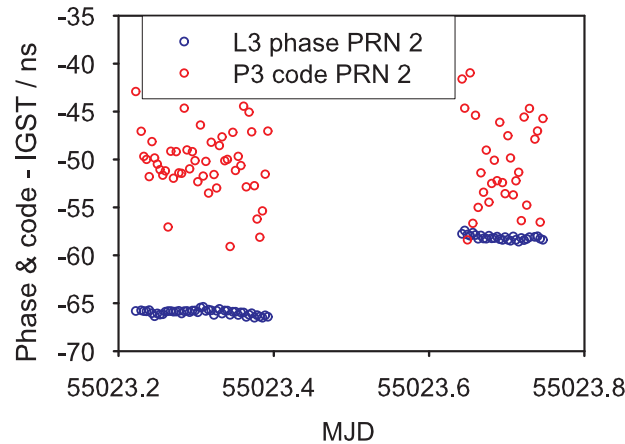


**Figure 4.13.:** The difference between UTC(PTB) and the IGS timescale calculated from troposphere corrected P3-code and L3-phase for the satellite transmitting PRN 2.

The chosen satellite was visible two times during one day. While the mean value of the code measurement is the same before and after the gap, the offset of the phase

measurement differs by more than 10 ns. The pre-solution of the phase ambiguity done by the receiver board inside the GTR50 is apparently imprecise, as seen in Figure 4.14. Thus, the method described above cannot be used for calibrated time comparisons using the carrier-phase measurement, but the relatively low noise level of the phase results compared to that of the code can enable accurate frequency comparisons.

To perform AV and CV frequency comparisons a frequency difference between the reference of the receiver and the IGS timescale can be calculated for each satellite in view by dividing the corrected L3 data by 300 s, according to equation (2.2). This should only be done for continuous satellite tracks in order to avoid outliers and inconsistencies. A gap, like that visible in Figure 4.13, has to be excluded. It can be bridged by the other satellites visible during this period.

From Figure 4.14, where the code and phase results of all satellites in view are depicted, it is obvious that the receiver can lose the tracking of particular satellites for a short period, which can lead to a new phase ambiguity. This can also happen between the processed 5 min epochs. Therefore it is necessary to check whether measurement data are available for all the 9 epochs between two processed 5 min epochs in the standard 30 s RINEX file or not. If data are missing, this epoch has to be treated as a gap and excluded from further processing.

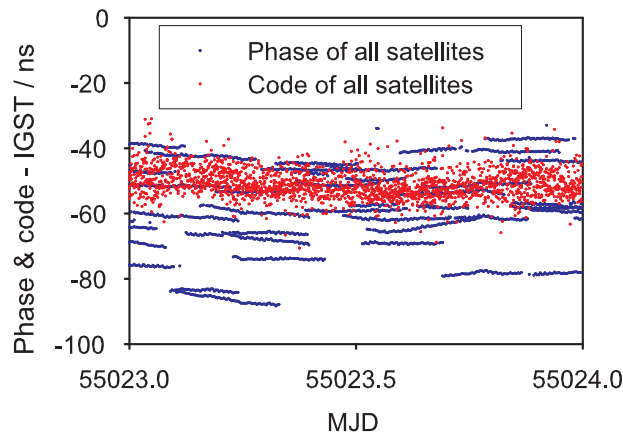


**Figure 4.14.:** UTC(PTB)-IGS time derived from troposphere corrected L3-phase and P3-code measurements for all satellites in view at PTB at one day.

The frequency difference between two remote receivers, and thus the frequency difference of the frequency standards connected to these receivers, can now be calculated by applying the process explained above to the L3-phase measurement data of both receivers. For CV a frequency difference between the two local standards is processed by subtracting the frequency differences available at the same epochs in the results of both receivers for each satellite independently. The mean value

of all satellites is calculated afterwards. In terms of the AV method the frequency average is at first independently calculated at any epoch for each receiver and differences are made based on the averages.

#### 4.4.2. Application to different Baselines

The first test of the code free frequency comparison method was performed on the 60 km baseline between PTB and the IQO of the LUH. The GTR50 at PTB was directly connected to an active hydrogen maser (H5) and the data at the IQO were collected by the mobile frequency reference (cf. Chapter 3) between the MJDs 54792 and 54796 at the end of the year 2008. In a first step the CV solution was computed only with the relativistic eccentricity correction (2.18). Then the solution was again computed using the troposphere model (2.10). The frequency differences of the CV solutions were integrated and are depicted together with the results of the NRCan-PPP software in Figure 4.15 on the left handed picture. For better visibility the drift of the masers was removed by a linear fit. The PPP solution was calculated without applying ocean loading coefficients and antenna phase center corrections. To enable the identification of all noise types the MDEV was calculated.

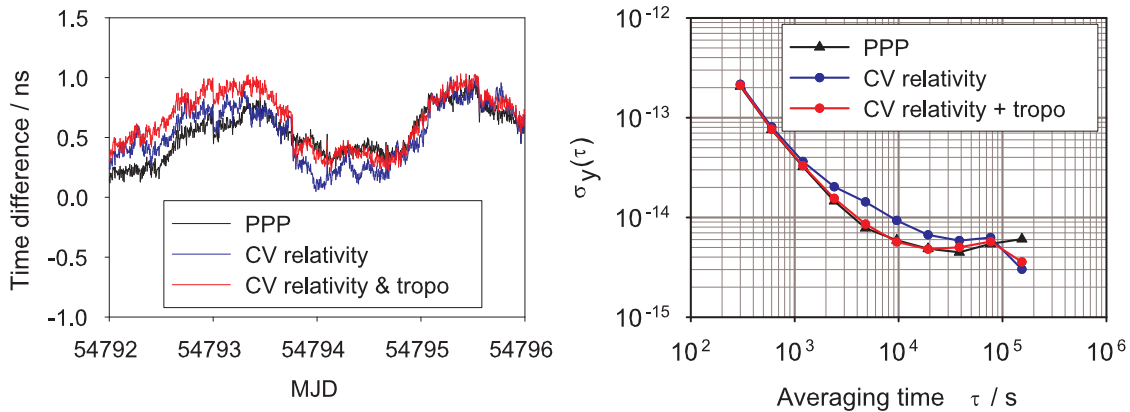


**Figure 4.15.:** Time differences for PPP and CV solutions and the related MDEV. The blue plots represents the CV solution with relativistic eccentricity correction, the red plots are the CV solution with eccentricity and troposphere correction.

The CV solution without troposphere correction is slightly less stable than the solution with troposphere correction, particularly for medium term averaging times between  $10^3$  s and  $10^5$  s. The solution with troposphere correction shows tighter agreement with the PPP solution and the instability is at the same level as that of PPP. Small phase jumps are visible in both the CV and the PPP solutions. One



of these jumps at the end of MJD 54793 is not visible in the PPP. Probably some of the jumps that are related to the GPS measurements are smoothed out by the Kalman filter.

This analysis has demonstrated that also on this relatively short baselines (60 km) the troposphere has an impact on frequency comparisons and must be corrected by a model.

The next comparison using the newly developed software was performed on the 2182 km baseline between ROA and PTB within the period MJD 55231 to 55239 in 2009. The frequency standards and the positions are the same as in Table 4.1. The frequency instability of the results, expressed as the modified Allan deviation (MDEV), is depicted in Figure 4.16. The instability of PTB's primary frequency standard CS2, locally measured with a high resolution phase comparator with respect to a H-maser at the same period and the instability of the PPP solution, obtained with the NRCan-PPP, are also depicted. The instability of the Cs 5071 clock is taken from the manufacturers specification. The PPP solution was again calculated without applying ocean loading coefficients and antenna phase center corrections. The code-free frequency comparisons are realized in this case as AV and CV solutions, applying the eccentricity correction (2.18) and the troposphere model (2.10).

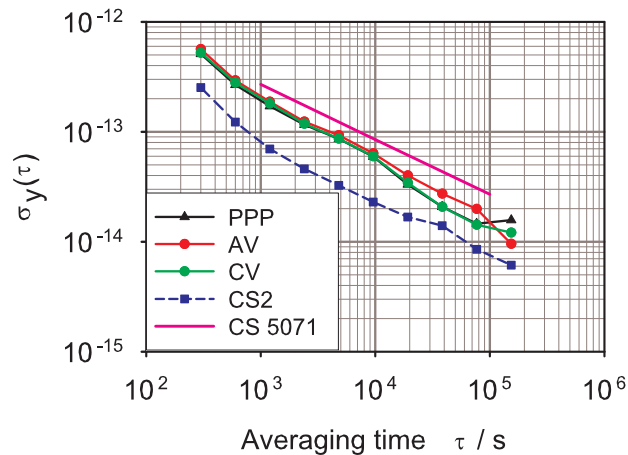


**Figure 4.16.:** Frequency instability of UTC(ROA)-UTC(PTB) expressed as the MDEV for PPP, code free AV, and CV comparisons over the 2182 km baseline PTB-ROA. The MDEV of CS2 is calculated from a local phase comparator measurement at PTB.

The three frequency instabilities of the remote timescale comparison UTC(ROA)-UTC(PTB) are similar. The remote comparisons are 2.5 times less stable than the primary frequency standard CS2, indicating that the remote comparison is limited by the performance of the commercial caesium standard at ROA. If commercial

caesium clocks are involved, the use of the simple models is almost sufficient on European baselines. In this particular case the performance of the Cs 5071 clock is better than specified by the manufacturer.

To figure out the limitations of the code free frequency comparison method and the correction models used within, it was applied to the intercontinental baseline between NICT and PTB at the same period as used for the ROA-PTB comparison. Since UTC(NICT) is derived from an active hydrogen maser (Table 4.1), the results were combined with the data of the local frequency comparator measurement CS2-active maser at PTB, such a way that CS2 cancels out and the final solution represents the comparison of two masers.

In fact, the PPP results reflects the instability of a remote maser comparison (cf. Figure 3.10), but the code free CV and AV solution seem both to be limited by the simplicity of the correction models. The AV results are slightly better than the CV results. This is due to the fact that on this intercontinental baseline mostly one or two satellites are commonly tracked by both receivers at low elevation angles. Thus, the AV and CV calculation were done a second time by using an improved model for the troposphere, taken from the GTR50's internal code processing software:

$$\delta_{\text{tro}} = T_0 \cdot \left( \frac{\sin(el) + 0.00143 \cos(el)}{0.0455 \cos(el) + \sin(el)} \right)^{-1}, \quad (4.3)$$

$$T_0 = 8.22 \cdot 10^{-9} \cdot s - 1.083 \cdot 10^{-12} \cdot h \cdot \frac{s}{m} + 7.467 \cdot h^2 \cdot \frac{s}{m^2}.$$

The correction is given in units of seconds and  $h$  is the height of the antenna above the Earth ellipsoid (A.3). This model directly includes the mapping function.

The instabilities in Figure 4.17 calculated from solutions obtained with the model (2.10) are labeled with "T1", while the instabilities calculated from solutions obtained with the improved model (4.3) are labeled with "T2".

The improvements due to the new troposphere model are marginal. The MDEV plot indicates a daily effect for the CV and AV solutions. This is due to the fact that, in contrast to PPP, no correction model for the solid Earth tides was applied to the code-free solutions. These effect has an opposite sign for PTB and NICT, because the longitude difference between NICT and PTB is about 125°. Thus, the model for the displacement of the solid Earth due the forces of Sun and Moon according to equation (2.20) was applied by adding the vector displacement to the Cartesian coordinates of the antenna before solving equation (2.13). The estimation of the positions of Moon and Sun in the ECEF system is described in Appendix G. The model (2.20) includes a constant part which depends only on the position of the antenna. To be consistent with the ITRF and in case of calibrated time transfer with PPP, this part has to be removed afterwards, but in the framework of code-free frequency comparisons these small constant offset do not have an effect.

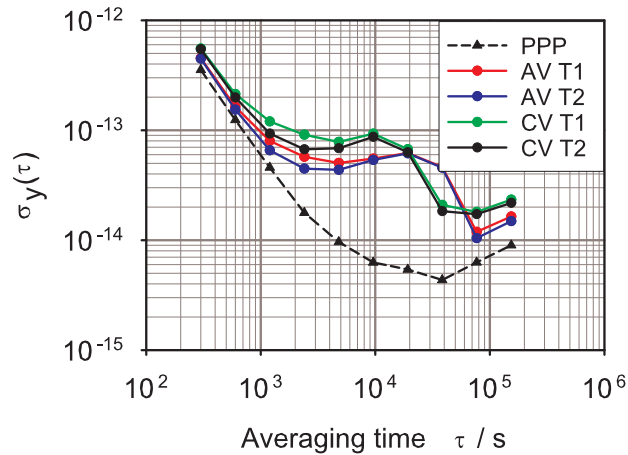


**Figure 4.17.:** Frequency instability of a maser comparison expressed as the MDEV over the intercontinental 8333 km baseline between NICT and PTB. "T1" and "T2" indicate the troposphere models (2.10) and (4.3), respectively.

In a first step only the effect due to the Moon was corrected. Then, in a second step both corrections for Sun and Moon were applied. The phase differences, obtained by integrating the frequency differences, are exemplarily depicted for one day in Figure 4.18 together with the PPP solution (black plot) and the AV solution without solid Earth tide correction (blue plot). The effect of the solid Earth tides is clearly visible. In the solution with only the part caused by the Moon corrected (red plot), only parts of the difference to the PPP solution are removed, while the solution with the complete correction for Sun and Moon (green plot) is in very good agreement with the PPP solution.

The exercise outlined in this section has clearly demonstrated the importance of accurate error modeling. Future improvements to this methods could be to solve for the time of signal emission  $t_s$  in an iterative process and to apply a correction for the difference between antenna phase center and center of mass of the satellites. Furthermore, the code free methods could be made applicable to receivers which are not providing a pre-solution of the phase ambiguity by aligning the phase measurement to the code by an additional preprocessing.

On relatively short baselines the modeling of the troposphere and the relativistic eccentricity correction is sufficient. The same is also valid on European baselines when stations are equipped with commercial caesium clocks. On very long intercontinental baselines the modeling of the solid Earth tides cannot be neglected if frequency comparisons at the instability level of active hydrogen masers are desired.

The troposphere can in all cases be corrected with the help of the relatively simple model (2.10). Improvements due to the model (4.3) are marginal. This is surprising, because in the literature [4, 5, 32, 33] the importance of sophisticated

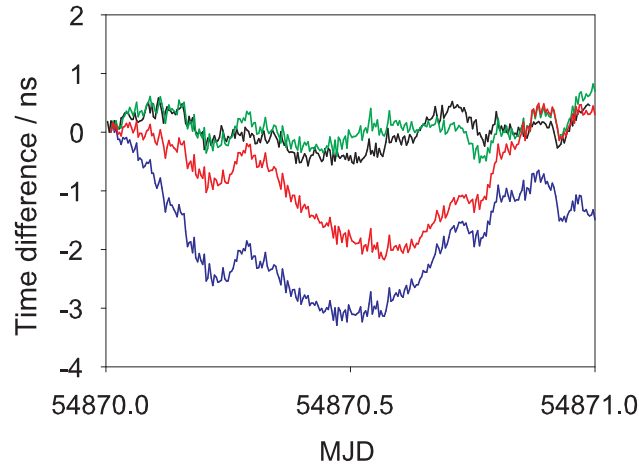


**Figure 4.18.:** One day maser comparison between NICT and PTB. The black plot was calculated with PPP, the blue one with code-free AV, relativistic eccentricity correction and troposphere model (4.3). The red plot represents the AV solution with the correction for the displacement of the Moon applied, the green plot is AV with both corrections for Moon and Sun applied

models is emphasized. The correlation between troposphere estimates and other parameters is analyzed in the reference [72].

Unfortunately, an analytical solution of the phase ambiguity problem has not yet been developed, but it has to be pointed out that the code free carrier-phase method can be also used for calibrated time transfer. The time differences obtained by integrating the frequency differences can be adjusted by comparing them to the P3 code time differences measured at the same period. The double difference has then to be subtracted from the code-free solution. The initial phase of the code-free solution could also be determined by an other independent method, like PPP or TWSTFT.

# 5. Hardware Experiments

In the previous Chapter the importance of the proper evaluation of the measurement data and the accurate modeling of the error sources has been demonstrated. However, the accuracy of GPS time and frequency comparison results particularly depends on the performance of the receivers involved.

In this Chapter the performance of receivers used for time and frequency comparisons is analyzed with respect to the short, medium, and long term instability. A comparison to state-of-the-art geodetic receivers that can only be used for frequency comparisons, since they are not equipped with an 1 PPS input, show that there is still room for improvements.

The common-clock difference (CCD) data of four receivers provided by the LUH QUEST institutes involved (IfE, IQO) were analyzed. These receivers were used for the first "long baseline common-clock experiment" between LUH and PTB forming double differences with measurement data taken from an optical telecommunication fiber link between PTB and LUH at the same time. The term "long baseline" is used here, because the baseline is long from the point of view of a common-clock experiment.

By comparing the different receivers in the quasi zero baseline setup at PTB, it was decided which types of receivers were finally used for that experiment involving the fiber.

Before that, the temperature stability of the receivers chosen for the long baseline common-clock experiment is analyzed. It shows up that the internal delay changes inside these receivers are highly correlated to the environmental temperature.

Based on the experiences with the QUEST receivers two new design concepts for a highly accurate frequency receiver are proposed.

Finally, the results of the first common-clock long baseline experiment are outlined. Such experiments could be used in the future for detailed studies of the correction models, because local clocks and other influences can be separated.

## 5.1. Performance of Receivers

In this Section, receivers which are typically used in time laboratories are analyzed with respect to their stability on different averaging times. This is done by quasi short baseline data evaluation at PTB.

Receivers which were provided by the IfE and the IQO were installed and compared with each other in order to figure out which type of receivers is most suitable for highly accurate and stable frequency comparisons (cf. reference [73]). The temperature stability of the IQO receivers is analyzed in detail.

### 5.1.1. Instability of Time and Frequency Receivers

In timing labs, such as PTB, receivers equipped with TICs as well as modified geodetic receivers are operated (cf. Section 2.3.4). At PTB two Ashtech Z-12 T receivers are continuously operated and providing data to the BIPM UTC computation as well as to the IGS network. These installations and the operation must not be compromised by any experiment. The Ashtech receivers are based on the design concept given in Figure 2.5. Additionally four receivers based on the concept outlined in Figure 2.4 are installed. Among these are two GTR50s whose data are analyzed.

In Figure 5.1 the results of a quasi zero baseline 5 day comparison of the Ashtech Z-12 T receivers and of a zero baseline comparison of two GTR50 time and frequency transfer receivers within the same period are shown. The GTR50s were connected to the same antenna using a splitter. The RINEX data of receivers were evaluated with the NRCan-PPP software using IGS products and the backward smoothing option.

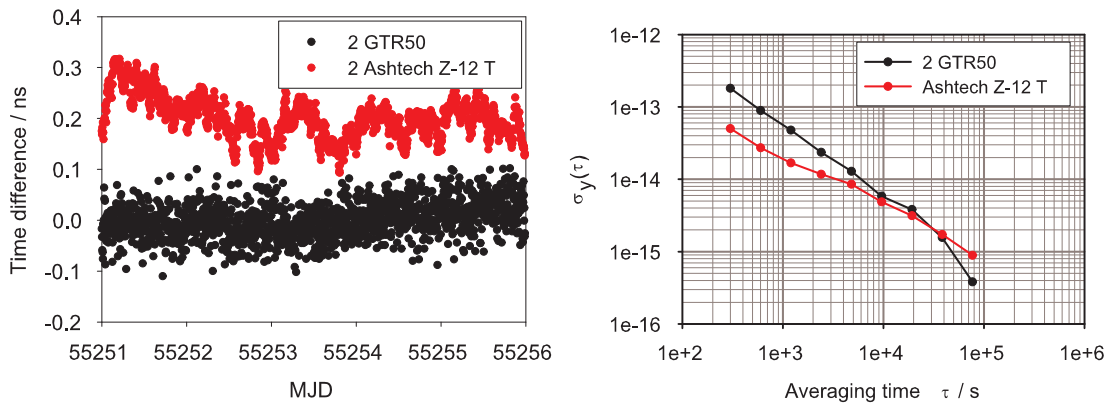


**Figure 5.1.:** Quasi zero baseline results of two Ashtech Z-12T and two GTR50 receivers. The frequency instability is expressed as the ADEV.

The performance of the GTR50 receivers is the same as in a short baseline CCD experiment (cf. Figure 4.2 and Figure 4.3). The performance of this type of receiver is limited by the performance of the internal time interval counter. The phase plot as well as the ADEV show the domination white phase noise, which is the typical limitation of time interval counters. In contrast, the Ashtech receivers

are limited by another type of noise, namely by random walk phase noise (white frequency noise). This is probably due to the locking of the receivers' internal crystal oscillator to the external reference frequency. Up to about  $10^4$  s their stability is better than that of the GTR50.

In the framework of UTC computation and time scale comparisons especially the long term performance of the receivers is of interest. Thus, the Ashtech receivers were compared with each other for 100 days in 2008 using the NRCan-PPP software in the forward processing mode and without ambiguity resetting. The question is how the random walk phase noise degrades the phase within time. The daily averages of this comparison and the corresponding TDEV are shown in Figure 5.2. Since these receivers are mainly used for the comparison of the timescale UTC(PTB) to the timescales of other institutes in the framework of TAI computation, the usage of the TDEV instead of the ADEV is preferable.

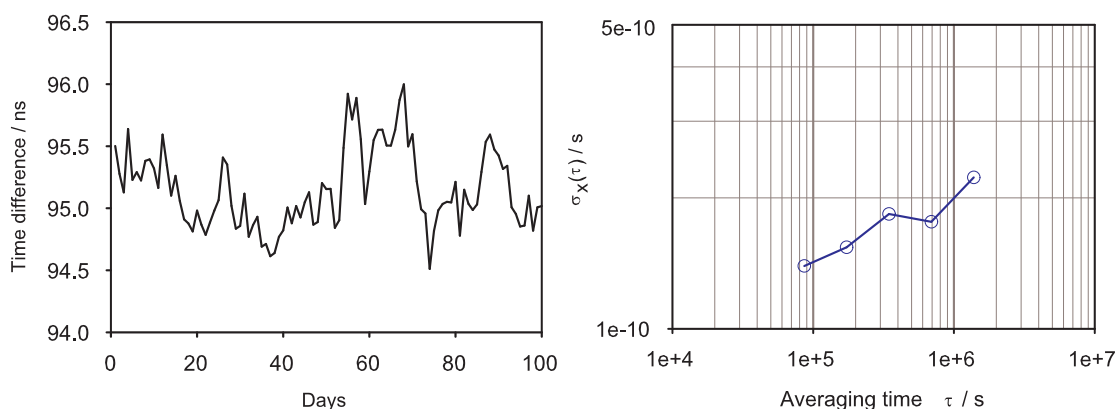


**Figure 5.2.:** Longterm comparison of two Ashtech Z-12 T receivers. The left plot shows the daily averages, the right plot shows the corresponding TDEV. The corresponding frequency instability at  $10^5$  s is  $2 \cdot 10^{-11}$ .

The variations show a maximum peak to peak difference of about 1.5 ns within the 100 days. However, time comparisons with these receivers are possible with a phase instability of less than 200 ps at an averaging time of 10 days. Unfortunately no such long batch of continuous data exist for a comparison of two GTR50 receivers, because only one of the two PTB receivers of this type is continuously operated and connected to UTC(PTB). The second one was periodically disconnected from UTC(PTB) and used for other purposes. A comparison of the fixed GTR50 to one of the two Ashtech receivers shows the same instability as the comparison of the two Ashtechs and does not need to be shown here.

In the framework of frequency comparisons mainly the short and medium term stability of the receivers is of interest. Figure 5.3 depicts the short term comparison of two GTR50s and two Javad Legacy receivers. The Javad Legacy receivers were provided by the IfE and operated at PTB for a few hours in a zero baseline setup.

The output RINEX data are given in 1 s intervals. To compare both types of receivers at the same level, also 1 s RINEX data were produced by the GTR50s' internal processing software, in contrast to the 30 s files that are usually generated in time and frequency laboratories. The data were processed with the NRCan software's backward mode and the satellite clocks were interpolated from the 5 min IGS clock products.

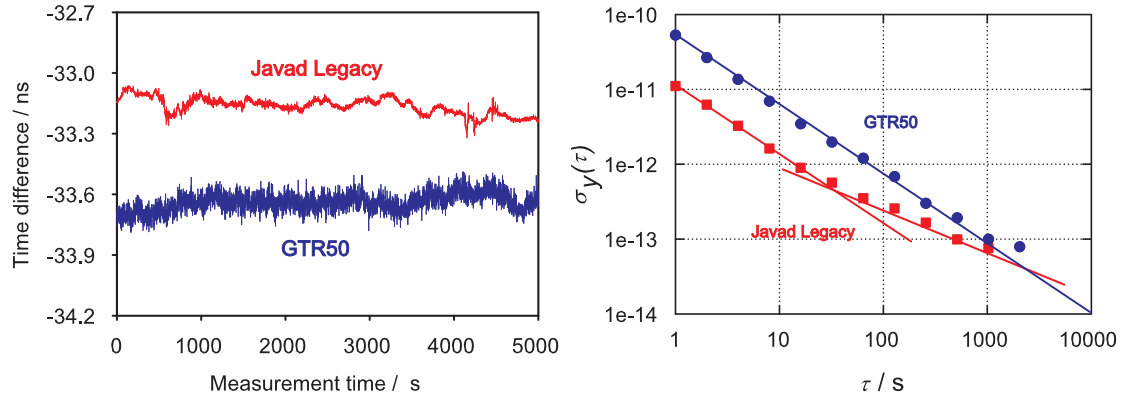


**Figure 5.3.:** Short term zero baseline comparison of two GTR50s and two Javad Legacy receivers. The frequency instability is expressed as the ADEV.

Due to the interpolation of the satellite clocks additional noise is generated. However, the GTR50s is about one order of magnitude less stable in short term than the Javad Legacy receiver, since it is limited by the performance of its internal time interval counter. In very short term the instability of the Javad legacy receiver is limited by white noise, as that of the GTR50. Then the random walk noise is dominating.

This comparison leads to the assumption that it should in principle be possible to construct a receiver which can reach the  $10^{-16}$  level at an averaging time of one day. For this, a solution to overcome the random walk noise is necessary.

### 5.1.2. QUEST Experimental Receivers

In 2009 four receivers provided by the QUEST institutes IfE and IQO were operated at PTB in a zero baseline setup within the framework of an experiment with using an optical fiber connecting PTB and IQO, which is explained later. One of the IQO receivers is of the type Javad Legacy, as the receivers used for the analysis given in Figure 5.3. The IQO receivers are based on the same GPS board that is used inside the GTR50 receiver, a Javad receiver circuit, but without temperature stabilization. Also no time interval counter is used. Instead, the board can be locked to an external reference frequency and the option of synchronizing the



internal timescale to an external 1 PPS is available. This option was not used in this analysis.

All receivers were recording the measurement data in 1 s RINEX files and the phase results were again obtained with the NRCan-PPP software in backward smoothing mode with IGS satellite clock interpolation. The results of the CCD comparisons are depicted in Figure 5.4. The IfE receivers are labeled "IFE2" (Javad Legacy), "IFE33", and "IFE82", manufactured by Leica, respectively. The IQO Javad receiver is named "IQO2". Four different CCD combinations are depicted in the Figure 5.4.

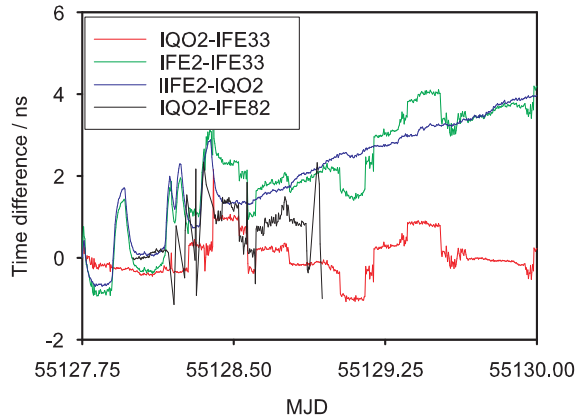


**Figure 5.4.:** Zero baseline CCDs of the QUEST receivers.

Both comparisons involving "IFE2" are affected by a phase drift. This drift is not present in the comparison of the two receivers "IQO2" and "IFE33". Thus this drift can be related to the "IFE2" receiver, which was thus excluded from additional experiments with the optical fiber. Unfortunately the "IFE82" receiver did not operate continuously during the complete measurement period. It was also excluded from further examinations. Only the "IQO2" and the "IFE33" receiver remain. The intercomparison of these two receivers indicates measurement interruptions, because the typical phase discontinuities due to a re-estimation of the ambiguities of all satellites in view are visible. An analysis of the RINEX data has shown that the interruptions are clearly related to the "IFE33" receiver.

Since the four receivers were operated within an experiment with an optical fiber between IQO and PTB, at the IQO four other receivers of the same types were operated. Unfortunately only two receivers were correctly recording measurement data. One of them was the second IQO receiver "IQO1". A comparison with the other IFE receiver showed the same performance as the "IQO2"- "IFE33" comparison. Again, interruptions were caused by the IfE receivers. This analysis is similar to that depicted in Figure 5.4 and is not shown here.

In the framework of precise positioning one can probably accept discontinuities and phase drifts, because these effects can be averaged out in the calculation of a static position, but in the perspective of time and frequency comparisons continuous and stable measurements are required. In terms of time and frequency transfer receivers providing a continuous and stable measurement over long periods are mandatory.

### 5.1.3. Temperature Sensitivity

As mentioned above the IQO receivers are based on the same GPS board as the GTR50 receiver. Inside the GTR50 this board is temperature stabilized. This shall avoid that the GPS measurements are highly affected by temperature variations due to changes of the internal delays.

To figure out the sensitivity of this type of receivers to the temperature one of the QUEST receivers was put in a metal box with regulated heating inside. The box was heated up to a maximum temperature of 68° C and RINEX data were recorded at the same time. Figure 5.5 shows the temperature inside the box as well as the time differences between the receiver outside the box in the stabilized measurement room and the receiver inside the temperature box.

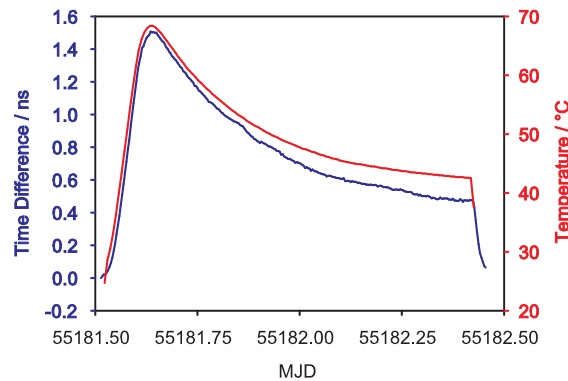


**Figure 5.5.:** Time difference between two Javad receivers (blue plot). One of the receivers is located inside a temperature regulated box. The red plot depicts the temperature inside this box.

The temperature and the electrical delays of the GPS receiver are highly correlated. A temperature sensitivity coefficient of about 20 ps/° C was estimated. The operation of receivers used for time and frequency transfer under stable environmental conditions is essential for highly precise comparison results.

## 5.2. Suggestions for Improvements in Frequency Transfer

The performance of GPS time and frequency transfer is not only affected by temperature variations influencing the electrical delays of the receivers, but also by temperature variations changing the electrical lengths of the antenna cable and the delays of the antenna itself, which are installed outdoor. In order to overcome these effects and the noise due to locking the internal oscillator of a GPS receiver to an external frequency the author has developed two ideas for improving the frequency stability. These two new approaches are not yet realized and just some preliminary experiments were performed.

### 5.2.1. Phase Comparator Measurements

To overcome the noise of the oscillator locking it would be desirable to construct a GPS receiver that does not have an internal crystal oscillator, but instead directly uses the reference frequency. Experiments with the GTR50's receiver board were performed but with no suitable result.

A second approach could be not to lock the internal oscillator to an external frequency, but to measure the frequency of the internal free running crystal oscillator with a high resolution phase comparator with respect to a reference frequency, similar to the receivers that measure 1 PPS signals with a time interval counter, but in the frequency domain. If two of such receivers are operated at remote sites, the GPS data can be combined with the frequency comparator data and exchanged for highly precise frequency comparisons.

A first experiment was performed at PTB with the two IQO receivers. Here both receivers were connected to the same frequency comparator such that no external reference frequency was needed (Figure 5.6).

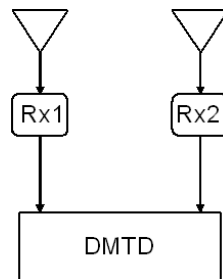


**Figure 5.6.:** Measurement of the output frequencies of the two IQO receivers. Rx stands for receiver, DMTD depicts the frequency comparator.

Unfortunately the output frequency of the receivers was 20 MHz, in contrast to the 10 MHz that are usually used in time laboratories. Thus, it was necessary to

convert the 20 MHz down to 5 or 10 MHz. Since the involved components, mainly additional amplifiers, were not constructed for signal levels needed by the high resolution frequency comparator at PTB, no suitable results were possible.

### 5.2.2. Stabilization of Cables

To cancel temperature effects on the antenna cable and the antenna a GPS receiver could directly be integrated together with the antenna in a temperature stabilized housing. In this case it is necessary to provide the reference frequency to the antenna site. Inspired by the stabilization of optical frequencies in terms of frequency comparisons with an optical fiber by a reflected signal, which is used to compensate changes in the length of the fiber, the idea of stabilizing the 10 MHz reference frequency came up. Figure 5.7 shows the proposed experimental setup.

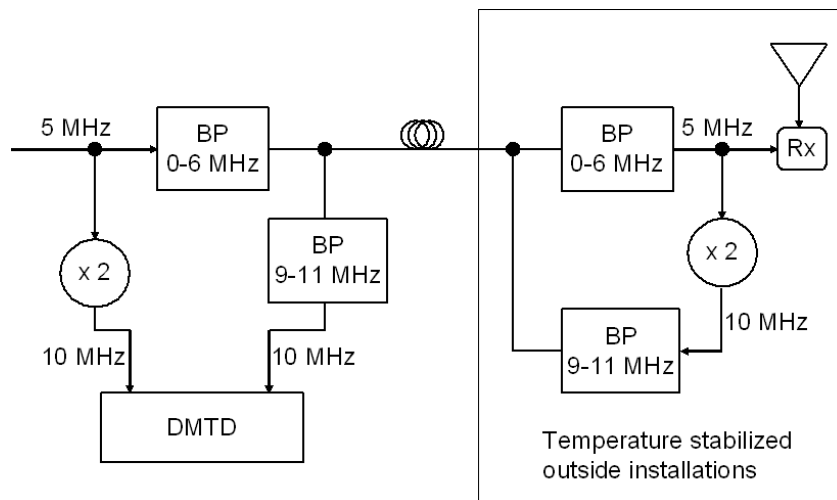


**Figure 5.7.:** Proposed set-up for high precision GPS frequency comparisons. BP denotes band-pass filter, DMTD is a high resolution frequency comparator. The elements shown in the box on the right handed side are located outside together with the antenna. The elements shown on the left handed side are located commonly inside a stabilized indoor measurement room.

The parts of the schematic located inside the box are the outside installations. It is connected to the other parts of the setup, which are located inside a stabilized measurement room, by one cable transmitting frequencies in both directions. Additional cables for electrical power and data transfer to the roof are also needed, but are not depicted in the Figure. The antenna is also part of the stabilized environment.

A 5 MHz signal is doubled to 10 MHz and connected to one input of a high resolution frequency comparator. It is additionally send to the outside installations and connected to the receiver which is integrated together with its antenna in a temperature stabilized box. Inside this box the signal is doubled to 10 MHz and send back to the measurement room. Bandpasses isolate the different signals from each other. The reflected signal is connected to the second channel of the phase comparator. The measurements of the phase comparator have to be applied to the GPS measurement as corrections at each of the remote sites (if such a setup is used at two remote sites).

First tests with common time laboratory equipment has shown that the reflection method would work and that delay variations due to temperature changes on the cable can be canceled out for the most part (Figure 5.8).

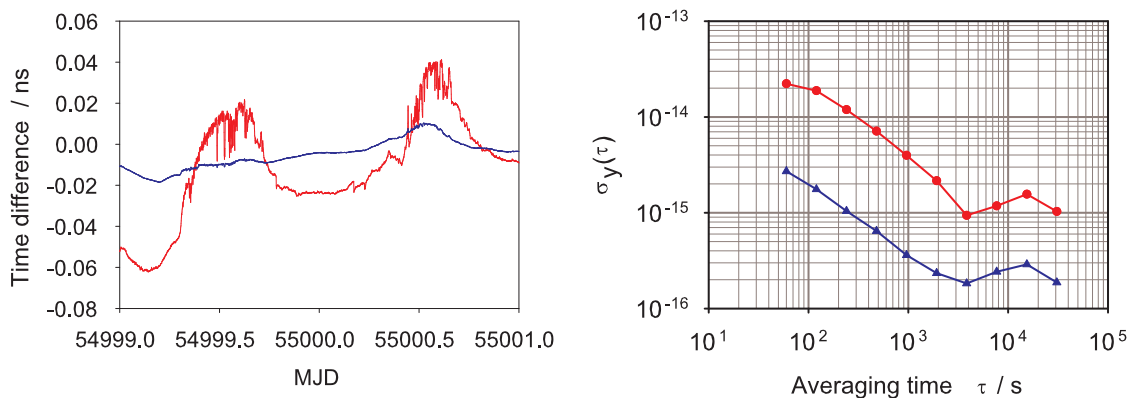


**Figure 5.8.:** Test of the proposed set-up without receiver and without electronic components outside. Instead, the signal was connected to a two channel high precision frequency comparator before and after the reflection (see text). Phase data as the integral quantity are shown. The red plot in the left handed picture shows the measurement of the signal fed to the cable with respect to the input signal. The blue plot depicts the double difference between these measurement and the reflected signal, also measured with respect to the input signal. The right handed plot depicts the related Allan deviations.

For the test the "outside" installations were located inside a measurement room. The connecting cable was a 50 m cable loop on the antenna roof of PTB. This cable was not intended for outdoor use and shows significant delay variations due to daily temperature variations. Instead of a receiver a second channel of a frequency comparator was connected to the 5 MHz of the "outdoor" installation and measured with respect to the 5 MHz input signal. The double difference of both frequency measurements shows that the delay variations of the cable be in principle compensated. The noise floor visible after averaging times of  $4 \cdot 10^3$  is related

to the frequency doubling amplifiers used for this preliminary experiment. It is expected that with the usage of modern low-noise amplifiers the instability is well below  $10^{16}$  for averaging times of  $10^4$  s.

### 5.3. The first Long Baseline Common-Clock Experiment

In 2009 an optical fiber was operated between PTB and the IQO of the LUH. The idea behind was to compare the experimental optical magnesium frequency standard developed at the IQO to the optical frequency standards and to the primary clocks at PTB with very high stability and accuracy [16]. A common optical fiber originally intended for telecommunication signals was used for this purpose. At PTB the 194 THz frequency of a laser was fed into the fiber and a reflected signal was used to compensate changes of the length of the optical fiber. By using erbium fiber laser frequency combs [62] at both sites the optical signal can be compared to the frequencies of the experimental optical standards as well as to microwave standards like the active masers at PTB and the passive maser H7 at the IQO. The fiber link can be used as a reference to characterize the GPS frequency link, because the optical link performance exceeds that of GPS on the relatively short 60 km baseline.

In the double differences between GPS and fiber measurement data the contributions of the masers cancel out and a common-clock characterization on the 60 km baseline is enabled. Similar experiments and measurements are planned for the future, e.g. between PTB and the Max-Planck Institute of Quantum Optics (MPQ) in Garching. They can be used for a detailed clock free analysis of the errors in GPS frequency transfer and help to improve the modeling of systematic GPS effects.

The measurement data of this experiment were evaluated by integrating the frequency data of the 1 s fiber measurement and then comparing it to the GPS data. The frequency reference at PTB was the active maser H6 (Figure 3.1). The 1 s RINEX data of the two IQO Javad experimental receivers were used and analyzed with the NRCan-PPP software in the backward smoothing mode. In order to get GPS results which are also spaced in 1 s intervals the clock interpolation mode of the software package was used. The results are depicted in Figure 5.9. The initial phase was arbitrarily chosen to be zero.

In the left picture it is clearly visible that the GPS link is noisier than the fiber frequency transfer. This could be partially induced by the analysis process due to the interpolation of the satellite clocks from the 30 s IGS clock data. Thus, the noise visible in the right picture can be mainly considered to be originating from

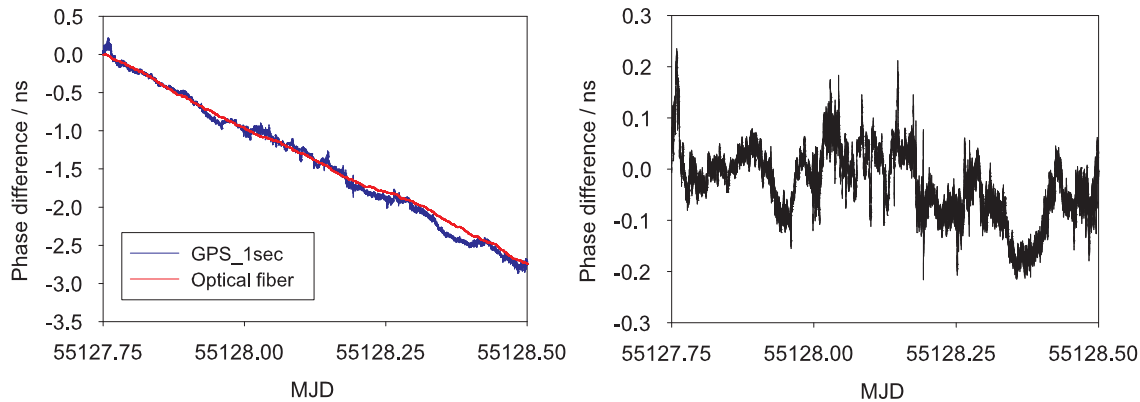


**Figure 5.9.:** Results of the GPS - optical fiber experiment between PTB and LUH. The left picture shows the GPS and the fiber link separately and the right picture depicts the double difference (see text).

the GPS link. The variations reach a maximum of 200 ps peak to peak and a standard deviation of 65 ps during the shown measurement interval.

Unfortunately, measurement data of the optical fiber are only available for a short period since the optical connection was in a very early experimental state. The laser system and the other optical components were very sensitive to any kind of mechanical vibrations. The measurement data were taken over a weekend when these vibrations were at a minimum since only few persons were inside the laboratories. With the given data set it was possible to calculate the frequency instability only up to  $10^4$  s, as depicted in the MDEV plot (Figure 5.10).

For short averaging times the fiber connection is about half an order of magnitude down to 0.8 orders of magnitude more stable than the GPS link. However, for very short averaging times it was limited by a counter at the IQO. In future experiments this can be avoided due to a more advanced experimental setup. For averaging times exceeding  $10^4$  s the limitation is given by the performance of the passive maser H7 (cf. Figure 3.4).

The instability of the stand-alone GPS link is at the same level as that of the clock free double differences for the short averaging times. Due to the lack of more fiber data a long term characterization was not possible in this framework. To avoid noise due to the interpolation of the satellite clocks, the GPS data were processed again with IGS 5 min clock products and the clock interpolation disabled in the NRCAN-PPP software package, as usual. The double differences are calculated by comparing the GPS data to the interpolated fiber data every 300 s. The double differences and the instabilities of the stand-alone GPS link, the fiber link, and the double differences are depicted in Figure 5.11.

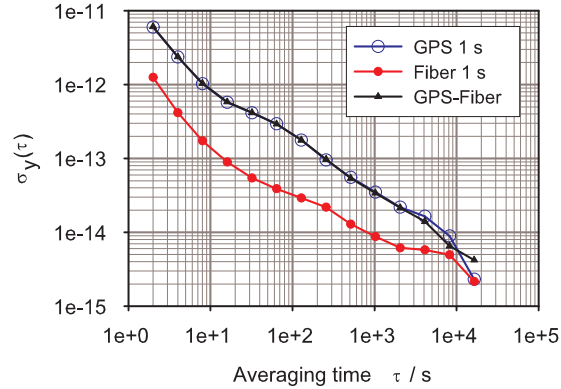


**Figure 5.10.:** Frequency instability of the GPS and optical fiber frequency comparison, expressed as the MDEV. In order to enable distinguishing between all noise types, the MDEV instead of the ADEV was calculated.

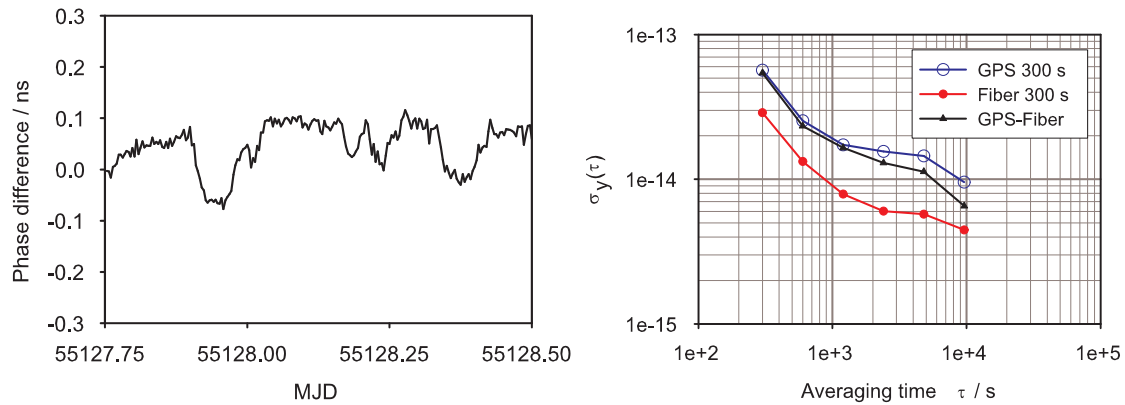


**Figure 5.11.:** Comparison between GPS and the optical fiber (left plot) and the MDEV of the GPS link, the fiber link and the double differences, respectively, evaluated on a 300 s basis.

The peak to peak divergence of the double differences is now at about 200 ps. In very short term, the GPS receivers seem to be able to measure with a precision of a few ps, but sometimes the solution is affected by instabilities. The MDEV indicates no significant improvement compared to the 1 s evaluation for short averaging times below  $10^3$  s. Then the canceling of the phase drift of the masers leads to a minor improvement, but this can also be achieved by just removing the maser drift with a linear interpolation.



The variations in the GPS result could be due to temperature instabilities, limitations of the error corrections, or limitations of the measurement process itself. Since the PPP comparison is an AV process, also noise of the IGS timescale could have an effect, because also on the relatively short 60 km baselines the two receivers were not always tracking the same satellites. Furthermore, especially the signal of satellites with low elevation angles could be affected by multipath induced by surrounding trees at PTB and surrounding buildings at the LUH, respectively.

To minimize the multipath effects the data were processed again, but the data of all satellite tracks with a satellite elevation below  $30^\circ$ , and in a second step below  $45^\circ$ , were rejected (Figure 5.12).

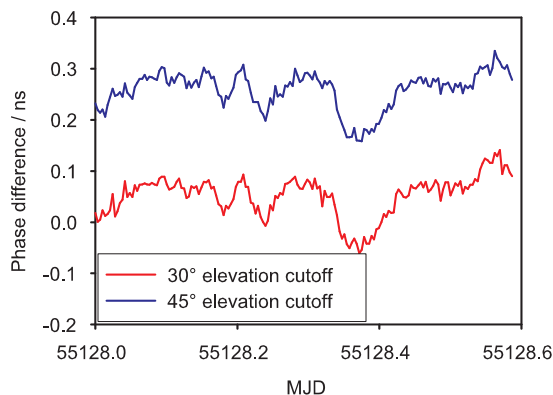


**Figure 5.12.:** Comparison of GPS and optical fiber with all satellites with elevation angles below  $30^\circ$  removed from the solution (red plot) and with all satellites with elevation angles below  $45^\circ$  removed from the elevation.

An improvement in the results is not visible. The double differences between the red and the blue plot in Figure 5.12 and the plot in Figure 5.11 are at the 0.05 ns level. The variations are probably partly related to the external temperature variations. The author hopes that with the suggestions described in the previous Section such variations can be minimized and frequency comparisons at the  $10^{-16}$  level at an averaging time of one day become possible. Before future experiments a detailed examination of the involved receivers and an analysis of the source of the instabilities should be conducted.

# 6. Relative Calibration of TAI links

## 6.1. Motivation

In the preceding chapters, all analysis has been done from the perspective of frequency comparisons and phase offsets have been arbitrarily chosen. However, the comparison of time scales, as done by the BIPM, and the evaluation of the corresponding links requires the accurate knowledge of the internal delays of the time transfer equipment involved or the delay of the complete link.

Up to now, operational links have been calibrated either by cost and labor intensive TWSTFT calibration campaigns, reaching the uncertainty of 1 ns [56] at the moment of the campaign, or by more easy to handle circulations of traveling GPS receivers [57], as conducted by the BIPM. The uncertainty of the latter has been estimated to be 5 ns for the operational link, considered valid for about 2 years until the next calibration campaign is conducted. This is based on BIPM's long-term experience on the performance of installed equipment during the past decades.

Recently, with the use of a new receiver (type GTR50), an uncertainty of less than 2 ns for a relative link calibration between ROA and PTB performed in 2008 has been reported [17]. The validity of this small uncertainty at the moment of the campaign is supported by previous studies of delay changes in GPS receivers of this type including switching on and off procedures [74]. In 2009 the author on behalf of PTB made a calibration along these lines between the Swiss Federal Office of Metrology (METAS) and PTB using a traveling receiver (TR) of the same type. At METAS the work was supported by the local staff, André Stefanov, Laurent-Guy Bernier, and Christian Schlunegger. The results are reported in the reference [75].

In 2010 PTB has conducted such a campaign involving USNO. For this purpose a GTR50 time and frequency transfer receiver and a SR620 TIC together with a monitor and a keyboard were integrated in a small transportable rack. The idea behind this was to simplify operations and to reduce the systematic uncertainty: In relative calibration campaigns the offset  $\delta t_0$  between the 1 PPS signal representing the local realization of UTC that is connected to the TR and the local UTC reference point has to be measured in each laboratory. Usually TICs are used for that purpose, but the internal delays between their two input channels vary from

unit to unit. If a TIC is shipped together with the receiver and  $\delta t_0$  is measured using exactly this device at all participating laboratories, the overall uncertainty would be reduced. The software which automatically controls the operation of the GPS receiver as well as of the TIC was developed by the author.

The USNO-PTB calibration campaign was organized by the author. At USNO the installation and operation of the calibration set-up was performed by Blair Fonville, Elizabeth Goldberg, and Stephen Mitchell, and supervised by Demetrios Matsakis.

It was decided to integrate only the contributions to the uncertainty budget, which are directly related to the calibration itself and not to consider the long term performance of the links. Furthermore an improved data handling, making use of the TDEV statistics was applied. Thus the overall uncertainty was reduced to less than 1 ns for some links.

In this chapter the differential GPS link calibration procedure is briefly explained. The uncertainty estimation is discussed and an introduction to PTB's new calibration set-up is given. The results of the 2009 METAS-PTB calibration campaign and of the 2010 USNO-PTB calibration campaign are presented. The METAS-PTB data have been re-evaluated using the improved data processing and the newer method of uncertainty estimation as for the USNO-PTB data.

The two campaigns between METAS and PTB and between USNO and PTB are of special interest, because the timescales of METAS and USNO were additionally connected to the PTB timescale by calibrated TWSTFT links which could thus serve as a verification for the GPS based method.

## 6.2. Description of the Calibration Procedure

In a relative GPS link calibration campaign between two timing laboratories LAB1 and LAB2 a traveling receiver (TR) is first operated at LAB1, together with all the fixed GPS receivers in a common-clock, very short baseline setup for several days. Then it is shipped to LAB2 together with its antenna and antenna cable and operated there again for several days in very short baseline setup together with the equipment in LAB2. In order to ensure that the internal delays have not changed during the travel the measurement at LAB1 is repeated after the TR was shipped back to LAB1.

As depicted in Figure 6.1, the devices are connected to the local UTC realization by 1 PPS signals with offsets relative to the local UTC reference point. Figure 6.1 shows the setup at two labs operating GPS as well as TWSTFT equipment. FR denotes all fixed receivers at LAB1 and LAB2, respectively.

Normally, for the fixed equipment the 1 PPS signal delays with respect to the local reference points are known with a low uncertainty, as well as equipment internal delays and antenna cables. However, in terms of a relative calibration

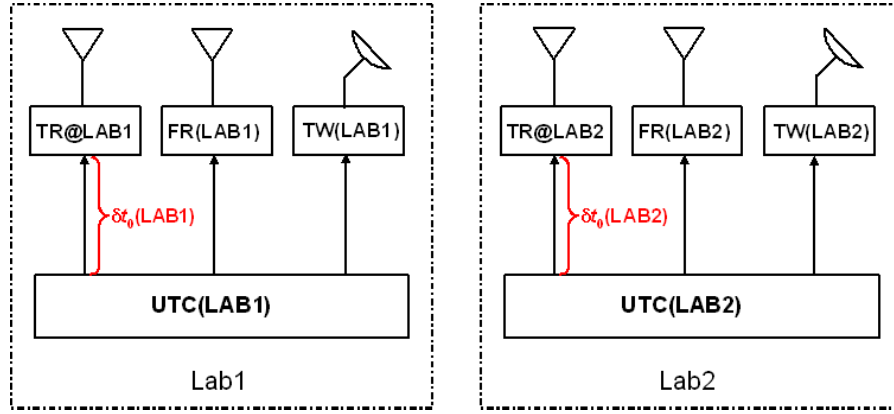


**Figure 6.1.:** Schematic of the link calibration setup at two labs equipped with GPS and TWSTFT.  $\delta t_0$  is the delay of the local UTC signal at each lab with respect to the TR's reference point. It is different at each lab and has to be determined by a measurement.

these delays do not have to be taken into account, if the goal is to calibrate the entire link, including the complete chain of signal distribution, cables, and antennas in both laboratories. The only important value is the offset  $\delta t_0$  of the temporary connection between the TR and the local reference point in both labs. It should be measured as accurately as possible.

To ensure that short term variations are averaged out in the common-clock difference (CCD) between the TR and the FRs, the TR should be operated at least about one week in each laboratory. The CCD values then represent the difference of the sums of the delays in the chains comprising antenna, antenna cable, receiver, and connection to the reference point. By differencing the CCD results of both labs, the contributions of the TR cancel out and the calibration value for the links between FRs (one pair or multiple combinations) is obtained. This statement is valid to the extent that the properties of the TR are unchanged during the campaign. In mathematical terms it reads as follows:

$$\langle \text{TR@LAB1-FR(LAB1)} \rangle - \langle \text{TR@LAB1-FR(LAB1)} \rangle = C_1 - C_2 = C_{\text{GPS}}, \quad (6.1)$$

where  $\langle \dots \rangle$  stands for the mean value of measurements over a certain period. It is noted that the sign of the calibration value  $C_{\text{GPS}}$  is arbitrarily defined by (6.1). With this convention the operational link between the two UTC realizations UTC(LAB2) and UTC(LAB1) has to be corrected according to

$$[\text{UTC(LAB2)} - \text{UTC(LAB1)}]_{\text{GPS}} = \text{FR(LAB2)} - \text{FR(LAB1)} - C_{\text{GPS}}. \quad (6.2)$$

The mean values of both CCDs at LAB1 before and after the trip to LAB2 are used to calculate the value  $C_1$  in order to detect small changes of the TR's internal

delays induced by the travel. The difference between the two CCDs obtained in LAB1 is part of the uncertainty budget which is explained later.

If the two labs maintain a TWSTFT link, as shown in Figure 6.1, a calibration value for the TWSTFT link can be calculated by comparing it to the calibrated GPS link:

$$\begin{aligned} & \langle [\text{UTC}(\text{LAB2}) - \text{UTC}(\text{LAB1})]_{\text{GPS}} \\ & - \text{TW}(\text{LAB2}) - \text{TW}(\text{LAB1}) \rangle = C_{\text{TWSTFT}}. \end{aligned} \quad (6.3)$$

The correction to the TWSTFT link is thus given by

$$\begin{aligned} & [\text{UTC}(\text{LAB2}) - \text{UTC}(\text{LAB1})]_{\text{TWSTFT}} \\ & = \text{TW}(\text{LAB2}) - \text{TW}(\text{LAB1}) + C_{\text{TWSTFT}}. \end{aligned} \quad (6.4)$$

In general, the TR can be shipped to more than one remote laboratory before returning to LAB1, as done by the BIPM for the relative characterization of time equipment (see e.g. [57]). Then also the links between the remote laboratories are calibrated. However, in this work the results of two campaigns with one remote laboratory involved are shown, and PTB acts as LAB1.

### 6.2.1. CV versus AV

As explained before in Chapter 2, a GPS C/A or P3 code link on an European baseline, such as between METAS and PTB or ROA and PTB, can either be evaluated in common-view (CV) or in all-in-view (AV) mode. AV is superior to CV on intercontinental baselines, such as between USNO and PTB, and is currently (October 2010) used for all the GPS-based TAI links by the BIPM [76]. One could intuitively think that a CV link should be calibrated using CV CCD computation and an AV link using AV CDD computation. In the following it is demonstrated that CV CCD computation is always preferable in order to calculate the calibration value, independent of the mode with which the link is operated later.

Two receivers of the same type (GTR50) and two receivers of different types (GTR50 and TTS-3) were compared in CCD experiments. As depicted in Figure 6.2, with identical receivers the result of CV and AV are equal (the double difference between AV and CV is zero) in 57.23 % of the epochs, while with different receivers this is just the case in 3.36 % of all measurement epochs.

For the interpretation of this result the measurement performed by one single receiver R with respect to one satellite at a certain epoch is expressed as

$$R_n(k) = \text{UTC}(L) - \text{GPST} + \Delta(k) + \varepsilon_n(k) + \delta_n, \quad (6.5)$$

with the satellite number n, the receiver number k=1 or 2, the local UTC realization UTC(L), the GPS time GPST, a receiver R specific offset  $\Delta(k)$ , a noise contribution  $\varepsilon_n(k)$  and a satellite specific offset  $\delta_n$  from the ideal GPS time. The sets of all

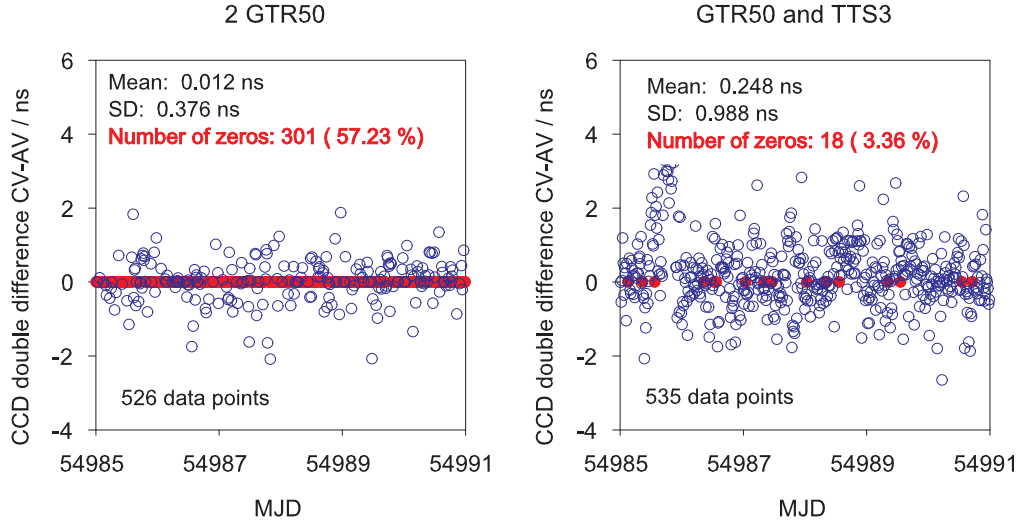


**Figure 6.2.:** CCD double differences CV-AV of two identical receivers (2 GTR50) and two receivers of different types (GTR50 and TTS-3), each equipped with its own antenna, but connected to the same clock.

satellite observations performed by two receivers in a very short baseline CCD setup at a certain epoch  $\tau$  can be defined as

$$\begin{aligned} S(1)_\tau &= \{R_1(1), R_2(1), \dots, R_N(1), R_{N+1}(1), \dots, R_P(1)\}, \\ S(2)_\tau &= \{R_1(2), R_2(2), \dots, R_N(2), R_{N+1}(2), \dots, R_Q(2)\}. \end{aligned} \quad (6.6)$$

The satellites are consecutively numbered and  $P$  and  $Q$  are the numbers of satellites tracked by receiver  $R(1)$  and  $R(2)$ , respectively. The observations numbered from 1 to  $N$  are done by both receivers simultaneously. Thus  $\tilde{P} = P - N$  is the number of satellites tracked only by  $R(1)$ , while  $\tilde{Q} = Q - N$  is the number of satellites tracked only by  $R(2)$ . A CV CCD comparison (CCC) can be written as

$$\begin{aligned} CCC &= \frac{1}{N} \sum_{n=1}^N [R_n(1) - R_n(2)] = \Delta(1) - \Delta(2) + \frac{1}{N} \sum_{n=1}^N [\varepsilon_n(1) - \varepsilon_n(2)] \\ &= C_L + E_{CV}. \end{aligned} \quad (6.7)$$

UTC(L) and the ideal GPS time GPST cancel out. An AV CCD (ACC) reads

$$ACC = \frac{1}{P} \sum_{n=1}^P R_n(1) - \frac{1}{Q} \sum_{n=1}^Q R_n(2) = \frac{1}{N + \tilde{P}} \sum_{n=1}^{N+\tilde{P}} R_n(1) - \frac{1}{N + \tilde{Q}} \sum_{n=1}^{N+\tilde{Q}} R_n(2). \quad (6.8)$$

After using  $1/(N+X) = 1/(N+X) + 1/N - 1/N = 1/N - X/[N(N+X)]$ , where  $X$  stands for  $\tilde{P}$  or  $\tilde{Q}$ , and segmenting the sums, equation (6.8) can be written as

$$\begin{aligned} \text{ACC} = & \frac{1}{N} \left[ \sum_{n=1}^N R_n(1) + \sum_{n=N+1}^{N+\tilde{P}} R_n(1) - \sum_{n=1}^N R_n(2) - \sum_{n=N+1}^{N+\tilde{Q}} R_n(2) \right] \\ & - \frac{\tilde{P}}{N(N+\tilde{P})} \sum_{n=1}^{N+\tilde{P}} R_n(1) + \frac{\tilde{Q}}{N(N+\tilde{P})} \sum_{n=1}^{N+\tilde{Q}} R_n(2) . \end{aligned} \quad (6.9)$$

The two sums from 1 to  $N$  represent the CCC (6.7). The satellite independent parts can be extracted from the other sums. Explicitly for receiver R(1) it reads

$$\begin{aligned} & \frac{1}{N} \sum_{n=N+1}^{N+\tilde{P}} R_n(1) - \frac{\tilde{P}}{N(N+\tilde{P})} \sum_{n=1}^{N+\tilde{P}} R_n(1) \\ & = \frac{1}{N} \left\{ \tilde{P} [\text{UTC(L)} - \text{GPST} + \Delta(1)] + \sum_{n=N+1}^{N+\tilde{P}} [\varepsilon_n(1) + \delta_n] \right\} \\ & - \frac{\tilde{P}}{N(N+\tilde{P})} \left\{ (N+\tilde{P}) [\text{UTC(L)} - \text{GPST} + \Delta(1)] + \sum_{n=1}^{N+\tilde{P}} [\varepsilon_n(1) + \delta_n] \right\} . \end{aligned} \quad (6.10)$$

The satellite independent parts cancel out. The same is valid for the terms with receiver R(2) measurements. Equation (6.9) can now be written as

$$\begin{aligned} \text{ACC} = & \text{CCC} + \frac{1}{N} \left\{ \sum_{n=N+1}^{N+\tilde{P}} [\varepsilon_n(1) + \delta_n] - \sum_{n=N+1}^{N+\tilde{Q}} [\varepsilon_n(2) + \delta_n] \right\} \\ & - \frac{\tilde{P}}{N(N+\tilde{P})} \sum_{n=1}^{N+\tilde{P}} [\varepsilon_n(1) + \delta_n] + \frac{\tilde{Q}}{N(N+\tilde{P})} \sum_{n=1}^{N+\tilde{Q}} [\varepsilon_n(2) + \delta_n] . \end{aligned} \quad (6.11)$$

Both receivers are tracking a number of satellites in parallel, while some satellites are only tracked by one of the receivers. An AV CCD is a CV CCD with additional noise and offset contributions. In nearly 60% of all measurements two identical receivers track exactly the same satellites, according to Figure 6.2. Achieving nearly 100% would only be possible if the two receivers were connected to the same antenna using a signal splitter. The other satellites add additional measurements to the solution and can slightly shift the mean value. In the operation of very long baseline links in AV mode the advantage of using many satellites, in particular at high elevation, is larger than these negative effect [21, 22], but in the framework of a calibration campaign they just increase the noise level, and thus the uncertainty.

The CV method for a code based link calibration is thus preferable. In reference [75] the evaluation of the CCD data is done with both CV and AV method. The results of the AV evaluation do not yield significantly different values than the CV evaluation, but the standard deviation of the individual measurements around the mean is higher.

### 6.2.2. Code Based Time Transfer and Position Errors

Time and frequency comparisons between two receivers are accomplished by comparing the 16 min spaced data of the CGGTTS files of two receivers. Since the data in the RINEX files are calculated from fixed positions which are manually entered to the processing software that generates the CGGTTS data, an error in the position causes an offset in the time result and affects the data by an increased noise level, because the geometric range is erroneous.

To study the impact of a wrong position information to the code based time transfer two receivers at PTB were examined in a short baseline common-clock setup. The P3 data of the two receivers are generated from the RINEX files with the RINEX2CGGTTS software. The P3 data of one of the receivers were recalculated several times and the position was fictitiously shifted in the three geodetic coordinates in several steps between a few cm up to 30 m from the original position. As processing period ten days were chosen. Then the new P3 data were compared to the original P3 data of the other receiver using the CV method. The mean values were subtracted from the true differences in order to get the delay due to a wrong position. Then the standard deviations (SD), reflecting the noise level of the data, were calculated. The results are depicted in Figure 6.3.

It is clearly visible that the error on the common-clock difference is linear within an error of the position up to 30 m for all the three coordinates. The effect is largest in the case of height errors, because the antenna is shifted virtually closer to or farther from the satellite constellation. The errors on the angle coordinates are smaller, because this coordinates benefit from symmetries. The offset in the latitude coordinate is due to shifting the virtual position with respect to the "north hole". In the longitude coordinate the offset is marginal, because the satellite constellation is completely rotationally symmetric in this coordinate, assuming perfect circular satellite orbits. The remaining divergence is due to the fact that the troposphere corrections are not solved correctly with a wrong position and that the orbits in reality are not perfect circles.

However, due to the incorrect positions the difference between the pseudoranges and the calculated distance to the satellite (and thus the time difference results) are different for each satellite, depending on the current satellite position. The noise is increasing dramatically for all three types of errors introduced with the same order of magnitude.



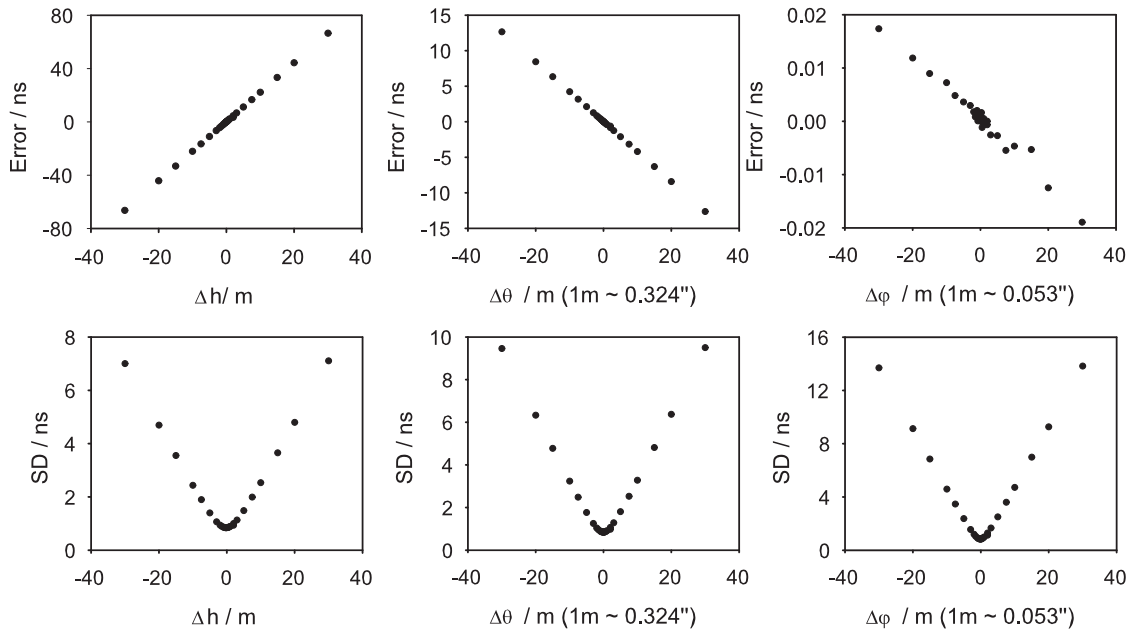


**Figure 6.3.:** Error on P3 CCD data due to wrong positions and the related standard deviation SD.  $\Delta\theta$ ,  $\Delta\varphi$ , and  $\Delta h$  are the errors in geodetic latitude, longitude, and height, respectively.

The results found here are only valid for the antenna site at PTB, because the satellite constellation is different at each location. Since the offsets are linear for position errors below 30 m it is sufficient to calculate the phase error only for one fictitiously shifted point in order to get the impact of a wrong position at any location.

In Figure 6.4 the fictive position shifting is applied to the comparison of the timescales UTC(USNO)-UTC(PTB) with the two calibrated receivers USN3 at USNO and PT02 at PTB. Here the positions of the USN3 receiver are shifted in the height.

The comparison with the original position is in good agreement with the results UTC(USNO)-UTC(PTB) taken from BIPM'S Circular T. With a position error of 3 meters the increase of the noise is marginal, but the offset with respect to the original data is significant. From the noise level the error is not detectable before the error is reaching 7.5 m.

This result shows the importance of proper position estimates for calibrated time transfer. However, for small errors below a few meters the position error can not be detected from the noise and the offset is absorbed by the calibration value (6.1) in terms of a relative link calibration.

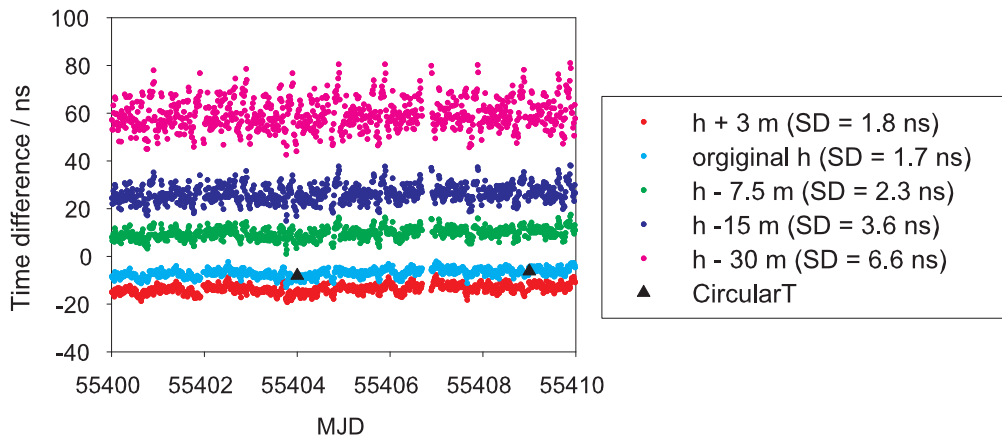


**Figure 6.4.:** Phase shift and noise on time transfer data due to errors of the height  $h$ .

### 6.2.3. PPP and Antenna Phase Center Corrections

In order to calibrate the links which are evaluated using the PPP method in operation the usage of PPP software is mandatory, even though the ambiguities, and thus the absolute phase values of the time results, are estimated from the P3 code, because the P3 data are calculated using fixed positions that are manually entered into the receiver's internal processing software (see previous Section 6.2.2) and could diverge from the positions calculated by the PPP software during the calibration period.

The software which is used by the BIPM to evaluate GPS time links with PPP is the NRCan-PPP package [15]. In Section 4.1 it was demonstrated that different software solutions can yield different time offsets for the same RINEX input data, also in a quasi zero baseline CCD setup. Thus, to calibrate a TAI link which is evaluated with PPP, the same software which is used by the BIPM for the link computation has to be used for the evaluation of the calibration values with exactly the same settings and input data.

In Section 2.5 it was briefly noted that the phase center of the receiving antenna depends on the elevation angle of the satellites. The IGS provides data files which include corrections for a variety of commercial available antennas. These corrections are obtained either by comparing the different antenna models to an antenna which was considered to be absolutely calibrated or by using a calibration robot [77]. These correction files can be used by the NRCan-PPP software. If the antenna name in the RINEX observation file header (cf. Appendix D) coincides with an antenna name in the IGS correction file, the correction is applied.

Although the effect of antenna phase center corrections does not show an effect on the instability of a time link, it is applied by the BIPM, if antenna informations are available in the RINEX header.

As shown in Figure 6.5 the corrections cause a general offset to the time results of the PPP solution. The data of two receivers called "Rx1" and "Rx2" here to simplify matters, operated at USNO in a common-clock quasi zero baseline setup were evaluated with and without applying the antenna phase center corrections. Then the possible four comparison combinations were calculated.

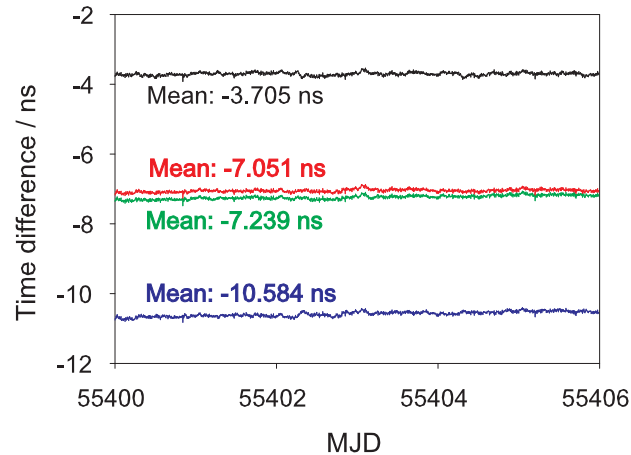


**Figure 6.5.:** PPP common-clock quasi zero baseline comparison of two receivers Rx1 and Rx2 at USNO. Black plot: Antenna phase center correction applied to Rx1, not to Rx2; red plot: No correction applied to both receivers; green plot: Correction applied to both receivers; blue plot: No correction applied to Rx1, correction applied to Rx2.

The red and the green plot, depicting the comparisons without antenna phase center corrections and with corrections applied to both receivers, respectively, are in close agreement, but the difference of the mean values is 0.19 ns. If the antenna phase center corrections are only applied to one of the two receivers, the solutions (black and blue plot) diverge from the red and green results by more than 3 ns.

In terms of calibration with an uncertainty at the nanosecond level it is absolutely necessary to apply the corrections to all receivers involved, in order to get proper results which can be used by the BIPM.

#### 6.2.4. Data Processing

The standard 16 minute interval CGGTTS P3 and/or C/A code data of all FRs involved in both laboratories are compared to the TR's CGGTTS data using the CV method to get the calibration values for the code based links. The standard 30 s interval RINEX data are processed with the NRCAN-PPP software using the same settings as done by the BIPM with 5 minutes IGS clock and 15 minutes orbit data and applying the antenna correction according to the IGS. Then the time results of the FRs are compared to the TR's results.

As pointed out before, only few receivers apply the internal and cable delays  $D_{P1}$ ,  $D_{P2}$ ,  $D_{Cab}$ , and  $D_{Ref}$  to the RINEX data, according to equation (2.23). Of course, these would be absorbed in the calibration values (6.1). However, it is useful to correct the calibration values obtained with the PPP processing for the internal delays taken from the P3 CGGTTS file header, in order to verify the consistency between the P3 and the PPP solution. In this work, both the corrected and the uncorrected values are given in the Tables 6.4, 6.5, 6.6, 6.9, and 6.11.

Subsequently, outliers in the code based data are removed by applying a  $3\sigma$  filter iteratively until it has no effect on the remaining data, with the limitation that not more than 5% of the data are removed. In the two campaigns described here the amount of removed code based data was marginal. In the case of the PPP data a phase drift can exceed the level of the phase noise and a  $3\sigma$  filter would remove too many measurement data. Hence, obvious outliers are removed manually.

In the next step the TDEV of the data is calculated with the  $\tau_0$  value chosen as the average of the individual data spacing (see Chapter 2). From the minimum in a double logarithmic diagram an averaging time for the individual data points is estimated in order to remove the white phase noise. In case of a significant data gap (more than 5% deviation from the original data spacing) the TDEV of the data before the gap and after the gap is calculated separately. The TDEV with its minimum at a shorter averaging time is used. Special attention has to be paid to the last TDEV value. Especially if it does not follow the trend of the previous values, it should be mistrusted and discarded.

The last step is to average the individual CCD data, to calculate the mean value, and to calculate the SD of these averaged data around the mean.

To calibrate a TWSTFT link, the TWSTFT data are compared to the data of one GPS link after applying the new calibration value (6.1) to this link, according to (6.3). Since the TWSTFT data spacing interval is in general higher than that of the GPS data, the GPS data are compared to values obtained by a linear interpolation between two adjacent TWSTFT measurements. This double difference data could be affected by significant outliers related to the TWSTFT as well as to the GPS link. To clean the data a  $3\sigma$  filter is applied iteratively, as for the code based CCD data. Finally, the double difference data are also averaged by estimating the averaging time with the help of the TDEV. The mean value of the averaged data represents the TWSTFT calibration value, and the SD of the averages around the mean contributes to the TWSTFT calibration uncertainty.

### 6.3. Uncertainty Estimation

The overall uncertainty of a relative GPS link calibration between two remote laboratories is given by

$$U_{GPS} = \sqrt{u_a^2 + u_b^2}, \quad (6.12)$$

with the statistical uncertainty  $u_a$  and the systematic uncertainty  $u_b$ . The statistical uncertainty is related to the noise of the GPS measurement and changes of the internal delays of the equipment, whereas the systematic uncertainty accounts for effects and errors that affect all CCD measurement data in the same but unknown way.

The statistical uncertainty is the geometric sum of the statistical uncertainty at LAB1 and the remote LAB2

$$u_a = \sqrt{u_{a,LAB1}^2 + u_{a,LAB2}^2} . \quad (6.13)$$

At the remote laboratory LAB2 the SD of the averaged data around the mean is directly the relevant contribution  $u_{a,LAB2}$ . Since CCD data are taken at LAB1 before and after the trip to LAB2 the higher SD is the relevant contribution. If the difference of the mean values of the two CCD measurements (dCCD) is smaller than this SD, the SD is taken as the uncertainty contribution  $u_{a,LAB1}$ . Otherwise the absolute value of dCCD is used, because equipment delay changes apparently exceed the other noise components.

The systematic uncertainty is given by

$$u_b = \sqrt{\sum_n u_{b,n}^2} \quad (6.14)$$

and explained in detail in Table 6.1 and the following text.

The instability of the connection to the local UTC signal ( $u_{b,1}$ ,  $u_{b,2}$ ) is estimated from long term experience at PTB, assuming that the environmental conditions at other laboratories are equivalent, and related to long term variations of the signal distribution system.

Since SR620 TICs were used in both calibration campaigns shown below to determine the offset  $\delta t_0$ , the errors related to this type of TIC have to be incorporated to the uncertainty budget ( $u_{b,3}$ ,  $u_{b,4}$ ). According to the manufacturer specifications [78] the trigger level timing error is given by

$$\text{Trigger level timing error} = \frac{15 \text{ mV} + 0.5\% \text{ of trigger level}}{1 \text{ PPS slew rate}} \quad (6.15)$$

for start and stop channel, respectively. With a trigger level of 1 V at one channel and an estimated signal slew rate of 0.5 V/ns the error is 0.04 ns per channel and 0.06 ns for the measurement after adding the start and stop error in quadrature.

According to information given by the manufacturer [37], the trigger level timing error of the TR's internal TIC ( $u_{b,5}$ ,  $u_{b,6}$ ) is estimated as 10 mV / (1 PPS slew rate) per channel. The error of the stop channel cancels out, because this channel is always provided with the signal of the receiver board and the error is the same at each laboratory.

**Table 6.1.:** Systematic uncertainty contributions. The contributions identified with an M are different in each calibration campaign and have to be determined by additional measurements. The contributions marked with an asterisk are only applied to special measurements (see text).

$u_{b,n}$	Value	Description
$u_{b,1}$	0.10 ns	Instability of the connection to UTC(LAB1)
$u_{b,2}$	0.10 ns	Instability of the connection to UTC(LAB2)
$u_{b,3}$	0.06 ns	TIC trigger level timing error at LAB1 [78]
$u_{b,4}$	0.06 ns	TIC trigger level timing error at LAB2 [78]
$u_{b,5}$	0.02 ns	TR trigger level timing error at LAB1 [37]
$u_{b,6}$	0.02 ns	TR trigger level timing error at LAB2 [37]
$u_{b,7}$	0.10 ns	TIC nonlinearities at LAB1
$u_{b,8}$	0.10 ns	TIC nonlinearities at LAB2
$u_{b,9}$	0.50 ns	Systematic error of the TIC at LAB1 [78]
$u_{b,10}$	0.50 ns	Systematic error of the TIC at LAB2 [78]
$u_{b,11}$	M	Jitter of the TIC measurement at LAB1
$u_{b,12}$	M	Jitter of the TIC measurement at LAB2
$u_{b,13}$	M	Determination of the UTC reference point at LAB1
$u_{b,14}$	M	Determination of the UTC reference point at LAB2
$u_{b,15}$	0.30 ns	Multipath [79]
$u_{b,16}$	0.18 ns	Antenna cable and antenna [74]
$u_{b,17}^*$	M	Position error at LAB1
$u_{b,18}^*$	M	Position error at LAB2
$u_{b,19}^*$	0.30 ns	Uncertainty of the ambiguity estimation [64]

The uncertainty contributions  $u_{b,5}$ ,  $u_{b,6}$  are related to imperfections in the TIC in conjunction with the external reference frequency. When two pulses with stable time offset between them are fed to the start and stop channel, the measurement result depends on the relationship between the pulses and the zero-crossing of the reference frequency. The traveling TIC was connected to different frequencies generated by different clocks at PTB (masers, commercial caesium clocks) and 5 MHz and 10 MHz were used, respectively, while the start and stop channel were provided with 1 PPS signals of one clock. The length of the reference cable was also changed. After averaging 50 single measurements in each setup slightly different results were obtained, but the difference was always below 0.1 ns. The results were verified by repeating all measurements with other TICs available at PTB. This effect has not yet been studied in detail, but it is probably related to interpolation processes in the TIC. It is accounted for by 0.1 ns at each laboratory.

The TR's internal TIC uses a surface acoustic wave (SAW) filter as interpolator, similar to the TIC analyzed in [80], but with less precision [37]. For TICs based on this principle the imperfection (the so-called nonlinearity effect) is negligible, because it is of the order of magnitude of a few picoseconds [37, 80].

According to the manufacturer's specifications [78] an uncertainty of 0.5 ns has to be taken into account at each laboratory ( $u_{b,9}$ ,  $u_{b,10}$ ) if local TICs are used to determine the delay  $\delta t_0$ , because the internal delays between their two input channels vary from unit to unit.

The offset  $\delta t_0$  is obtained by averaging multiple single TIC measurements at each lab. The jitter of the TIC is given by the standard deviation of these measurements around the mean ( $u_{b,11}$ ,  $u_{b,12}$ ). From the point of view of the TIC measurement this is the statistical uncertainty of the TIC, while the other TIC related uncertainties listed in Table 6.1 are contributions to the systematic uncertainty of the TIC. However, in the framework of the GPS measurement it becomes a systematic error, because it affects all CCD data in the same way.

Currently there is no standardized definition of the UTC reference point in a time and frequency laboratory. It could be a fixed connector or the endpoint of a cable. It could also be a virtual point somewhere inside the 1 PPS distribution devices. In many cases the physical signal used for the  $\delta t_0$  measurement is defined by an additional measurement with uncertainties  $u_{b,13}$  and  $u_{b,14}$ , respectively.

The propagation of the satellite signal is affected by multipath effects [79] ( $u_{b,15}$ ), but in the quasi zero baseline setup, in which the CCDs are measured, the atmospheric and site displacement effects cancel out.

Since CCD data are taken for at least one week, diurnal variations due to temperature variations over the day which affect the outside installations (cables, antennas) should cancel out in the average, but increase the statistical uncertainty. However, it cannot be assumed that the average outside temperature at both laboratories is the same for the three measurement periods, and thus the length of the antenna cable of the TR and the electrical delay of the antenna is exactly the same. In both campaigns shown here a FSJ1 cable with an approximate electrical delay of 224 ns was employed. The cable manufacturer indicates a temperature sensitivity value of 400 parts per million (ppm) for the electrical delay change per degree Celsius. With the assumption of a maximum average temperature change of 20°C between each CCD measurement the delay change of the entire 50 m cable is 0.09 ns. Unfortunately, the temperature sensitivity of the Novatel GPS 702GG antenna is unknown. Therefore a temperature coefficient of less than 0.01 ns/°C for the complete system cable and antenna is used here, according to CCD measurements performed at ROA in 2008 between two GTR50 receivers connected to the same type of antenna with the same type of cable with comparable length [74]. The order of magnitude is supported by the analysis presented in the reference [81]. The uncertainty contribution  $u_{b,16}$  is thus accounted for by 0.18 ns, indicating that

half of this sensitivity is related to the cable while the other half is related to the antenna.

An evaluation of the temperature sensitivity of a GPS system using code-phase residuals was proposed in [82], but this could not be done with a receiver of the type GTR50, because the 1 PPS signal measured by the internal TIC versus the external 1 PPS signal is derived from the code and applied to all data. Hence the temperature sensitivity of the code measurement is transferred to the phase measurement.

As demonstrated above, a position error is linear in the time results and dominating in the height. According to that, the impact of the height error at each laboratory can be estimated by fictitiously shifting the position of one of two receivers taking CCD data in a quasi zero baseline setup by using the RINEX2CGGTTS conversion software [31]. Within the framework of calibration, these errors  $e_h(\text{LAB1})$  and  $e_h(\text{LAB2})$ , given in units of ns/m, are multiplied with the absolute value of the difference between the "true" position and the position manually entered into the TR's processing software. The position error of the FRs is not subject of a relative calibration, because the phase shift is included in the link calibration value and the increased noise level of the CCD measurement is incorporated into the statistical uncertainty. If the manually entered position of the TR's antenna is obtained by collecting RINEX data from one or two days and the position is estimated with the NRCAN-PPP software and then used for the CGGTTS processing, as done in the METAS-PTB calibration campaign at METAS, the uncertainty can be neglected, because the precision of the PPP software is expected to be at the sub-centimeter level [47], if the transformation between the reference frames (A.5) is accounted for correctly, such that the TR position and the positions used by the FRs are consistent.

An additional uncertainty contribution  $u_{p,19}$  of 0.3 ns is applied to all PPP calibrations, because the initial phase of the carrier frequency is a priori unknown and has to be estimated by the PPP software from the P3 code. In reference [64] a typical phase discontinuity of 0.15 ns per receiver was found for PPP batch processing with the NRCAN-PPP [15], independent of the length of the processed batch. This adds up geometrically to 0.21 ns for a CCD comparison between a pair of receivers and to 0.3 ns for the two CCD measurements at LAB1 and LAB2.

The uncertainty of the TWSTFT calibration (6.3) is given by geometrically adding the uncertainty of the GPS link calibration to the SD of the averaged double difference data around the mean.

The systematic error of the TICs is a dominating contribution to the fixed parts of the statistical uncertainty. It can be removed by using the same TIC at both participating laboratories.



## 6.4. PTB's Calibration Set-up

To measure the offset  $\delta t_0$  between the local UTC reference point and the 1 PPS signal connected to the TR usually a TIC is used at each laboratory. The delay between the start and stop channels of different TICs are unequal, also for TICs of the same type. The time interval measurement with the Stanford Research System SR620 TIC, which is well known and extensively used in the timing community, is affected by a systematic error of 500 ps according to the manufacturers specifications [78]. This error has to be considered in the uncertainty budget (Table 6.1).

To reduce the overall uncertainty of a relative link calibration, a traveling TIC can be shipped together with the receiver, and  $\delta t_0$  would then be measured using exactly this device at all participating laboratories involved in the calibration campaign. The systematic error of the traveling TIC cancels out and the uncertainty contributions  $u_{b,9}$  and  $u_{b,10}$  vanish. In order to accomplish this, a GTR50 time and frequency transfer GPS receiver has been integrated with a SR620 TIC in a small transportable rack together with a monitor and a keyboard (Figure 6.6). This new calibration set-up was used for the first time to calibrate the links between PTB and USNO in 2010.

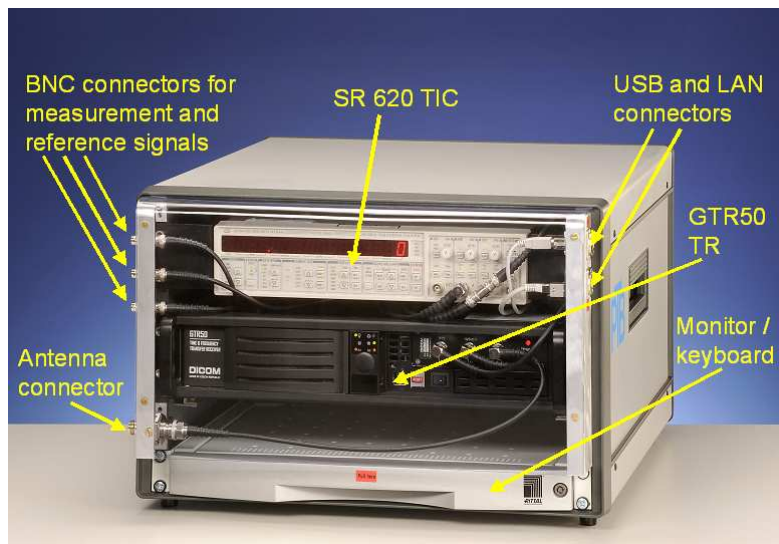


**Figure 6.6.:** Front view of the calibration set-up.

Beyond the reduction of the uncertainty the new calibration set-up offers further advantages, because it is easy to use for the local staff at the involved laboratories due to a text based software that controls the complete calibration procedure including the TIC measurement as well as the GPS measurement, and thus minimizes the risk of unintended errors. Furthermore the remote labs neither need to

allocate additional equipment like keyboard and monitor for the control of the TR nor to care about documentation of the TIC measurement and its uncertainty.

Figure 6.6 shows the front side of the calibration set-up. All connectors are easily accessible along the side, except the connection for power supply, which is located on the back side. This avoids cable mess in the laboratory. The LAN computer network connector is only designated for maintenance purposes at PTB and deactivated in the remote laboratories.

In Figure 6.7 on the left photo the signal connectors are visible, on the right scheme the cable layout plan inside the rack is depicted.

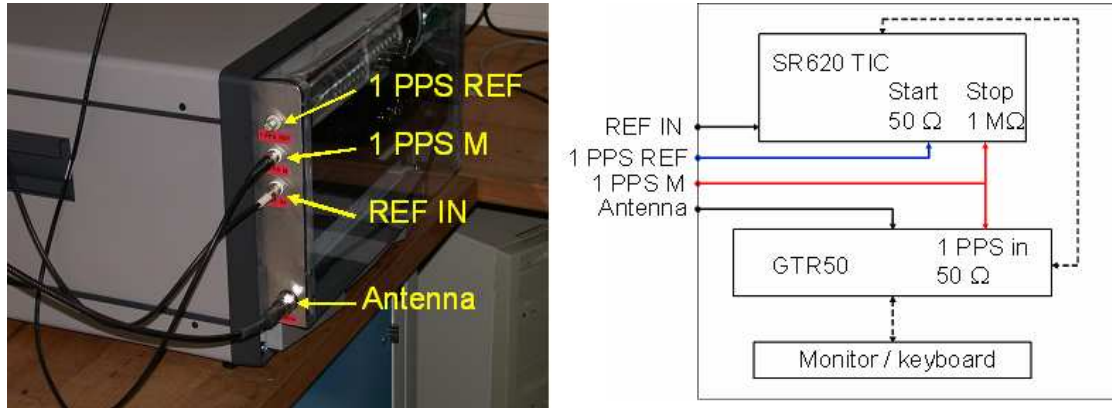


**Figure 6.7.:** Signal connectors (left picture) and internal cable layout (right picture).

At the REF IN connector the set-up is provided with a 5 MHz or 10 MHz external reference frequency. This frequency needs not to be the UTC frequency and can be derived from any atomic standard. Effects due the TIC imperfections are included in the uncertainty budget, as explained above. The 1 PPS M connector provides the receiver with the 1 PPS UTC signal. The offset of this signal with respect to the local UTC is measured by the TIC before the GPS measurement starts. For this purpose a 1 PPS signal with known delay to UTC has to be connected to the 1 PPS REF connector. The delay induced by the internal cables, labeled red and blue in Figure 6.7, cancels out in equation (6.2).

After setting up the calibration set-up in the laboratory's measurement room and connecting it to the power supply the operating system of the TR boots up and the calibration software starts automatically. The required AC input voltage can be adjusted to the anticipated conditions in each laboratory. In Figure 6.8 in the left picture the calibration set-up with pulled out monitor and keyboard is shown.

The first program screen requests the user to wait until the internal SR620 TIC is warmed-up. The right plot in Figure 6.8 shows that the TIC needs approximately

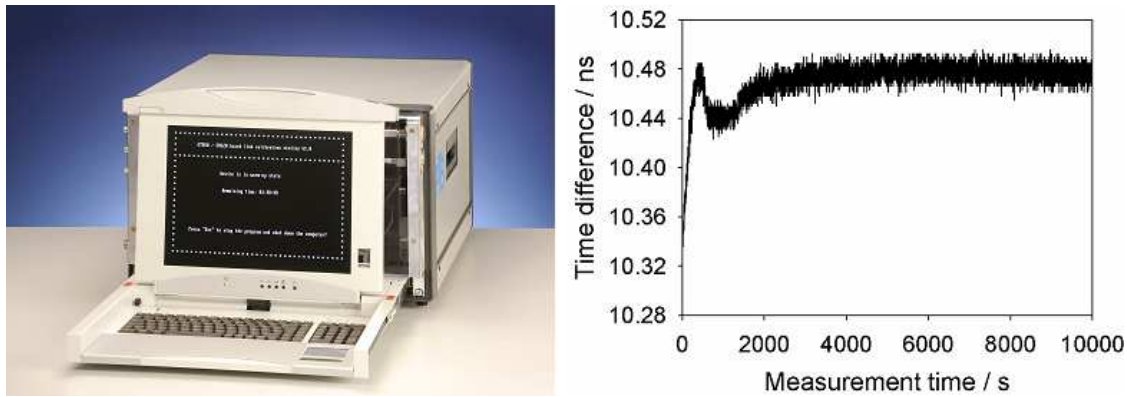


**Figure 6.8.:** The calibration set-up with pulled out monitor and keyboard (left) and warm-up characteristics of the internal SR620 TIC (right).

one hour to reach a stable state after turning-on. For this test both the start and stop channel were provided with the same 1 PPS signal by using a power splitter and a length difference of the connecting cables. To ensure that the TIC is in the stable state in any case under the unknown environmental conditions in a remote lab, the waiting time is set to two hours. The remaining time is displayed on the monitor.

After the warm-up period the operator is asked for the precise antenna position in ITRF Cartesian coordinates. If the antenna position is unknown in a remote laboratory an arrangement could be made in order to enable collecting RINEX data for one or two days, to send it to PTB, and to input the position later after estimating it from the RINEX data using the PPP method.

It is impossible to proceed with the procedure until both signals are correctly detected by the TIC. The operator has to decide whether the reference frequency is 5 MHz or 10 MHz. Normally a trigger level of 1 V is used for the 1 PPS M signal, but if arrangements are made with the remote lab this level can be changed between 0 V and 2 V. This level is then used by the TIC as well as by the TR.

After this, the SR620 TIC automatically starts to measure the delay between 1 PPS REF and 1 PPS M. The software takes 100 single measurements and calculates the mean value, the jitter and the rate. The measurement can be repeated in case of problems with the signals, e.g. if a significantly high jitter or rate is observed. The measured delay of the reference signal and the internal cable delay is applied to the GPS measurements automatically.

The reference cable can be removed after the delay measurement and used for other purposes in the laboratory. Due to the internal TIC used inside the GTR50 no additional measurements are needed. The internal temperature stabilization inside the GTR50 needs about 20 minutes to warm up the receiver board and the TIC card to 45°C. Then the receiver starts to collect the first GPS data. At

the end, after about one week taking GPS measurement data, the reference delay measurement can be repeated to check the stability of the environmental conditions in the laboratory and to verify the correctness of the uncertainty estimates  $u_{b,1}$  or  $u_{b,2}$ , respectively.

## 6.5. METAS-PTB Calibration

In June and July 2009 the time links between MEATS and PTB were calibrated using a TR of the type GTR50. The TR was operated at PTB in June 2009 for six days within the interval MJD 54985 - 54991. Then, after the TR was used for another purpose, it was shipped to METAS and operated in July for ten days between MJD 55016 and MJD 55026. After this, it was immediately sent back, so that the second operation at PTB was done between MJD 55034 and MJD 55042.

Table 6.2 specifies the types of fixed receivers involved at PTB and METAS and their data output. The nomenclature is according to the conventions used on the BIPM data server (C/A, P3, RINEX) and by the IGS tracking network (RINEX), respectively, if the data are provide to these institutes. Otherwise the laboratory's internal convention is used. An exception is the TTS-3 receiver. The TTS-3 RINEX data were found not useful for the purpose here [75]. In the following it will be referred to the FRs as given in Table 6.2, which takes into account that one receiver produces different kinds of data.

**Table 6.2.:** Receivers at PTB and METAS and the related data output.

Institute	Receiver	P3	RINEX
PTB	Ashtech Z12-T	PT02	PTBB
	Ashtech Z12-T	PT03	PTBG
	AOS TTS-3	PT06	- - -
	Dicom GTR50	PT08	PT08
MEATS	Ashtech Z12-T	CH01	WAB2
	Septentrio PolaRx	CH03	WAB4

As Table 6.2 shows, eight P3 links and six PPP links can be evaluated. Other receivers at PTB that provide C/A code data have not been involved, because the METAS receivers do not provide this kind of data.

In June 2009 lightning conductors were mounted nearby the antennas at PTB, as visible in Figure 6.9, without notification of the laboratory. These installations affected the measurements by multipath effects, which resulted in unstable carrier-phase measurements. Thus, the lightning conductors were removed at the end of

July. At PTB the tracking of satellites with low elevation angles is limited by the surrounding trees. In general, the roof of the METAS building is a better place for GPS measurements, due to free sight to all directions.

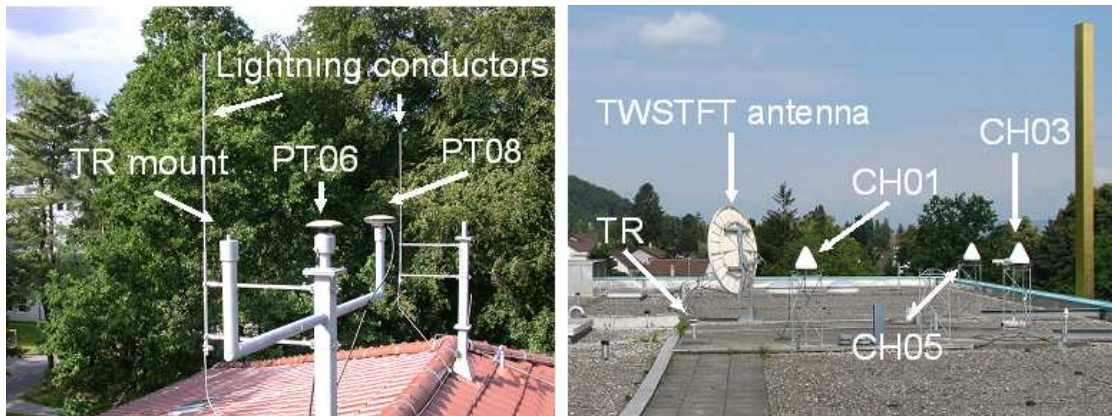


**Figure 6.9.:** Antenna sites at PTB (left picture) and at METAS (right picture). The TR antenna was not mounted at PTB site when the photo was taken. CH05 did not collect data during the calibration campaign.

At PTB the offset due to a wrong position of the TR's antenna was found to be  $e_h(\text{PTB}) = 2.22$  ns/m. The absolute value of the manually entered a priori position and the position estimated from the RINEX files of the TR during the CCD measurement is 0.119 m and the related uncertainty contribution is  $u_{b,17} = 0.26$  ns. At METAS the TR's antenna was installed on a temporary mount with unknown a priori position. Thus, the TR was collecting one day RINEX data with arbitrary offset  $\delta t_0$  and fictitious position before the CCD measurement started. The position was estimated using the NRCan-PPP online version. The uncertainty contribution  $u_{b,18}$  can be considered to be zero.

The offset of a 1 PPS signal with respect to the local UTC reference point at PTB is measured using a reference cable connected to the 1 PPS UTC distribution. The delay at the male BNC connector is periodically checked with respect to UTC(PTB) with a fixed SR620 TIC which is used as the central measurement device to compare all PTB clocks to UTC(PTB) and with each other. In normal operation the start and stop channels are connected to a switching matrix that allows for measuring all intercombinations of the connected clock signals. The true UTC(PTB) reference point is a virtual point inside the signal distribution chain. If any changes of the equipment are made, this point has to be reconstructed by aligning the data after the change to the data before the change and adjusting delay constants in the computer software which controls the switching matrix and reads the TIC measurements.

The reference cable is checked by disconnecting the TIC's stop channel from the switching matrix and measuring the UTC signal, as provided by the switching matrix, with respect to these cable. The start channel is provided with the UTC signal of the switching matrix. Before using the reference cable in order to determine  $\delta t_0$  it was verified with the method described above. After averaging 20 single measurements the jitter was 0.02 ns. This has been taken into account as uncertainty contribution  $u_{b,13}$ . The offset  $\delta t_0$  was measured with a second TIC in the framework of the METAS-PTB calibration campaign.

The local UTC representation at METAS UTC(CH) is by definition the male BNC connector of a cable connected to the start channel of a SR620 TIC. The stop channel was directly used to determine  $\delta t_0$  at METAS. Thus the uncertainty contribution  $u_{b,14}$  is zero.

Since different counters have been used for the  $\delta t_0$  measurement,  $u_{b,9}$  and  $u_{b,10}$  remain in the uncertainty budget. In both laboratories 20 single measurements were averaged and the jitter was found to be 0.20 ns in both cases ( $u_{b,11}$  and  $u_{b,12}$ ).

In Figure 6.10 the results of the P3 and PPP CCD measurements at PTB are depicted. The nomenclature here and in the following illustrations is to be under-

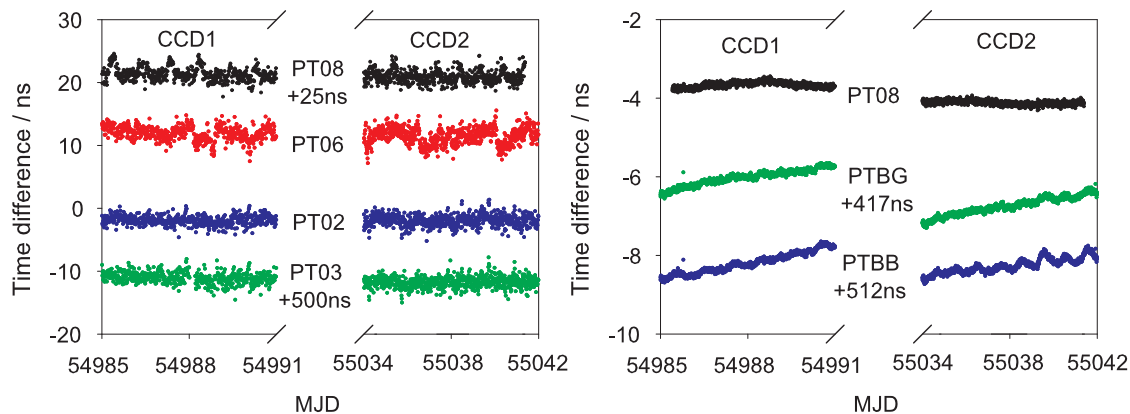


**Figure 6.10.:** Code (left) and PPP (right) CCD measurements at PTB before and after the calibration trip to METAS.

stood as TR-FR, e.g. PT02 denotes the CCD measurement TR-PT02. For better visibility arbitrary offsets have been applied to some of the data. No significant differences of the results before and after the calibration trip to METAS are visible for the P3 measurements. Due to problems with the antenna, PT08 RINEX data are not available for MJD 54985 and MJD 55042. Furthermore this data look more unstable than expected from a comparison of two GTR50 [65, 74], which was probably caused by the lightning conductors.

The CCD results at METAS are shown in Figure 6.11. At MJD 55021 the CH01/WAB2 receiver has not generated a daily RINEX file. The data were rebuilt

from hourly files, but it was not possible to reconstruct the corresponding P3 file using the RINEX2CGGTTS conversion software [31]. The PPP results generated with the rebuilt RINEX data show a phase jump indicating a complete loss of all satellite tracks.

In Figure 6.11, as well as in Figure 6.10, phase drifts in the PPP results of the Ashtech Z12-T receivers are clearly visible. These drifts cannot be found in the P3 data. They are only related to defects in the phase measurement and are probably intensified by the Kalman-Filter of the NRCan-PPP software (cf. Figure 4.5). In reference [75] this effect was accounted for by an additional uncertainty contribution. This was omitted in the analysis presented here, because the drift is already increasing the statistical uncertainty and thus already taken into account. A detailed analysis of the Ashtech Z12-T receiver can be found in reference [83].

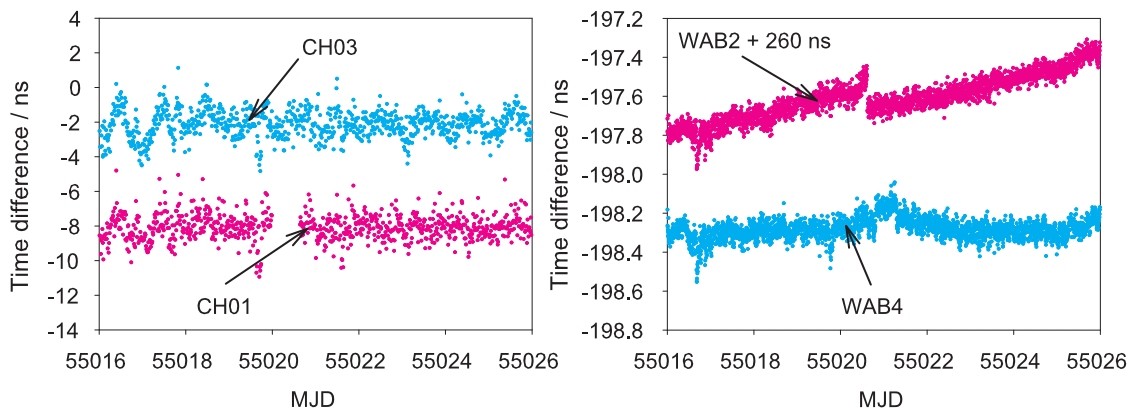


**Figure 6.11.:** Code (left) and PPP (right) CCD measurements at METAS.

In Figure 6.12 the TDEV is exemplarily depicted for the second P3 CCD measurement at PTB (CCD2) and the P3 CCD measurement at METAS. Due to the data gap at MJD 55021 in the CH01 data the TDEV is calculated twice with the data before and after the gap. In Table 6.3 the data averaging times estimated from the TDEVs of all CCD measurements are listed. AVT denotes the averaging time. In the PTB case AVT1 stands for the averaging times estimated for the results obtained from the first CCD measurement (CCD1), while AVT2 denotes the averaging time for the results of the second CCD measurement (CCD2).

Table 6.4 shows the results of the two CCD measurements at PTB, the corresponding standard deviation (SD), and the difference between the CCD measurements (dCCD) after averaging the data according to Table 6.3. The underlined value is used as the statistical uncertainty contribution at PTB. Since PTBB and PTBG do not apply the internal delays to the RINEX data, these values are added to the PPP calibration values at the end of the data analysis according to equa-

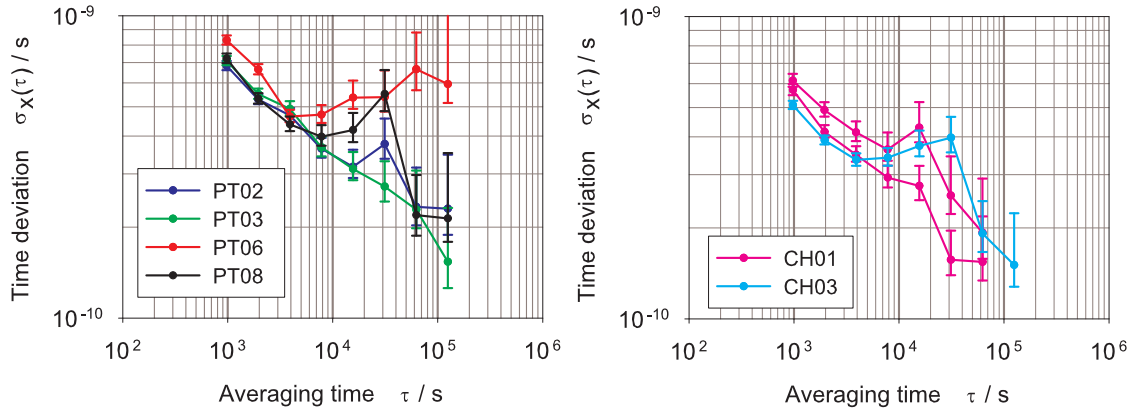


**Figure 6.12.:** Double logarithmic plots of the time deviations of the second P3 CCD measurement at PTB (left plot) and the P3 CCD measurement at METAS (right plot).

**Table 6.3.:** Estimated data averaging times.

PTB				METAS		
Type	FR	AVT1	AVT2	Type	FR	AVT
P3	PT02	1 day	1 day	P3	CH01	$3 \cdot 10^4$ s
P3	PT03	$1.5 \cdot 10^4$	1 day	P3	CH03	1 day
P3	PT06	7680 s	3840 s	PPP	WAB2	2400 s
P3	PT08	1 day	1 day	PPP	WAB4	2400 s
PPP	PTBB	2400 s	2400 s			
PPP	PTBG	2400 s	2400 s			
PPP	PT08	2400 s	2400 s			

tion (2.23) and stated in brackets. All P3 results agree with the PPP results within a few 0.1 ns.

The P1 and P2 delays,  $D_{P1}$  and  $D_{P2}$ , and the antenna cable delay  $D_{Cab}$  of the PT03/PTBG receiver have never been evaluated and are set to zero in the RINEX2CGGTTS conversion software. The applied delay consists only of the reference signal delay  $D_{Ref}$ . Hence the CCD values in Table 6.4 are at the level of about -511 ns for PT02, as well as for PTBG after the correction for the reference delay.

The results at METAS and the corresponding SD, which is the statistical uncertainty at METAS, are depicted in Table 6.5. Here also the internal delays of the WAB2 and WAB4 receivers are added after the analysis. The P3 and PPP



**Table 6.4.:** Results of the CCD measurement at PTB. Values are rounded to the second decimal. The underlined value is chosen as the uncertainty  $u_{a,PTB}$ . The values in brackets are the calibration values after applying the internal delays according to (2.23).

Type	FR	CCD1 / ns	CCD2 / ns	$C_1$ / ns	dCCD / ns	SD1 / ns	SD2 / ns
P3	PT02	-1.91	-1.92	-1.91	0.01	<u>0.21</u>	0.19
P3	PT03	-511.10	-511.76	-511.43	<u>0.66</u>	0.42	0.18
P3	PT06	11.95	11.48	11.71	0.47	0.83	<u>1.04</u>
P3	PT08	-3.64	-4.02	-3.83	<u>0.38</u>	0.31	0.24
PPP	PTBB	-520.20 (-1.76)	-520.26 (-1.82)	-520.23 (-1.79)	0.06	<u>0.26</u>	0.18
PPP	PTBG	-423.03 (-511.23)	-423.75 (-511.95)	-423.39 (-511.59)	<u>0.72</u>	0.19	0.22
PPP	PT08	-3.66	-4.12	-3.89	<u>0.45</u>	0.06	0.04

**Table 6.5.:** Results of the CCD measurements at METAS. Values are rounded to the second decimal. The values in brackets are the calibration values after applying the internal delays according to (2.23).

Type	FR	$C_2$ / ns	SD / ns
P3	CH01	-8.08	0.25
P3	CH03	-2.11	0.14
PPP	WAB2	-457.61 (-8.02)	0.11
PPP	WAB4	-198.28 (1.56)	0.05

results are in good agreement for the receiver CH01/WAB2, but between CH03 and WAB4 the discrepancy is more than 3.5 ns. This is due to missing information about the CH03/WAB4 antenna. The antenna type is not included in the RINEX file header and thus no phase center correction is applied by the PPP software. As demonstrated before (Chapter 4) this can lead to an offset with the observed order of magnitude.

Table 6.6 shows the calibration values and the corresponding uncertainties for all possible links between METAS and PTB. The 3 ns discrepancy between the links

**Table 6.6.:** Calibration values and corresponding uncertainties for all possible GPS links between METAS and PTB. The values are rounded to the second decimal. The values in brackets are the calibration values after applying the internal delays according to (2.23).

Type	Link	$C_{\text{GPS}} / \text{ns}$	$u_a / \text{ns}$	$u_b / \text{ns}$	$U / \text{ns}$
P3	CH01-PT02	6.17	0.33	0.87	0.93
P3	CH01-PT03	-503.35	0.70	0.87	1.12
P3	CH01-PT06	19.79	1.07	0.87	1.38
P3	CH01-PT08	4.25	0.45	0.87	0.98
P3	CH03-PT02	0.20	0.25	0.87	0.90
P3	CH03-PT03	-509.32	0.67	0.87	1.10
P3	CH03-PT06	13.82	1.05	0.87	1.36
P3	CH03-PT08	-1.72	0.40	0.87	0.95
PPP	WAB2-PTBB	-62.62 (6.23)	0.28	0.88	0.92
PPP	WAB2-PTBG	34.22 (-503.56)	0.73	0.88	1.14
PPP	WAB2-PT08	453.72 (4.13)	0.47	0.88	0.99
PPP	WAB4-PTBB	-321.95 (-3.36)	0.26	0.88	0.92
PPP	WAB4-PTBG	-225.11 (-513.15)	0.72	0.88	1.14
PPP	WAB4-PT08	194.39 (-5.46)	0.46	0.88	0.99

involving CH03 and the links involving WAB4 is also visible here. All uncertainties are at the level of about 1 ns and well below 2 ns, as in previous exercises [17, 75].

The results can be compared to the results of previous calibrations conducted by the BIPM [84, 85], where a traveling Ashtech Z12T receiver was circulated between the laboratories several times between 2002 and 2008. This traveling receiver was considered to be absolutely calibrated and the CCD measurements were used to calibrate the internal P1 and P2 delays of the fixed receivers. The method of absolute receiver calibration is described in the reference [86]. PT02 has been calibrated by the BIPM in April 2008 [84] and CH03 has been calibrated in August 2008 [85]. The link calibration value of the link CH03-PT02 in Table 6.6 is nearly zero, confirming the stability of the equipment during more than 2 years.

The CH01 calibration was done in 2004. The link CH01-PT02 has to be corrected by 6.17 ns.

Before this result is discussed further, it has to be noted that any changes of the equipment result in different delays. This changes are modifications of the time and/or frequency signal distribution system, modifications of the antenna and the antenna cable, dislocations of the antenna, and variations in the environmental conditions. Also the replacement of the receiver itself with an other one causes a delay difference, because  $D_{P1}$  and  $D_{P2}$  are a-priori unknown.

The link calibration values can of course be readjusted, if a second calibrated link is operated during the period in which the events described above have been occurred. The data of the link which lost its calibration are therefore aligned to the data of the calibrated link. But this practice obviously increases the uncertainty, because the uncertainty of the readjusted calibration value consists of the geometric sum of the uncertainty of the calibrated link and the SD of the comparison of the two links. Furthermore, in case of the alignment of one link to the other the baseline is not short and additional uncertainty contributions due to the atmospheric (2.8) and site displacement effects have to be taken into account.

It can be assumed that over time changes occur to all the equipment at different instants of time. It is thus necessary to perform periodical realignments on all links. This leads to an increase of all calibration values over the years. This shows that calibrations should be repeated periodically as often as possible.

Between 2008 and 2009 the operation of the receivers CH03 and PT02 was stable at the sub-nanosecond level. No changes of the equipment have been occurred within this period. On the one hand this demonstrates that the calibration campaign with the GTR50 receiver produced reliable results, on the other hand the 5 ns uncertainty applied by the BIPM to all GPS links used for TAI computation becomes questionable in the case that verifiably no equipment changes have been occurred after a calibration campaign. The 5 ns originates from BIPM's long term experience.

Unfortunately it is not possible to trace what happened to the CH01 receiver between 2004 and 2009. Large steps typically point to changes in the installations rather than in the receiver itself. This supports the above statement that calibration campaigns should be repeated periodically.

METAS and PTB maintain a TWSTFT link in the Ku-band, which was calibrated using a traveling TWSTFT earth station in 2008 [87]. The results of the GPS calibration can be verified by comparing a calibrated GPS link to the TWSTFT data. If the TWSTFT calibration value calculated according to equation (6.3) vanishes within the combined uncertainty, the proof is obtained that relative GPS calibration campaigns can serve as an alternative to the cost and labor intensive calibrations with traveling TWSTFT equipment and that the GPS based calibration uncertainty is not underestimated.

For this purpose the now calibrated P3 link with the lowest uncertainty, which is the link CH03-PT02, is compared to the operational TWSTFT link. The GPS link is evaluated in the CV mode. The processed period is partially overlapping with the CCD measurement at METAS and CCD2 at PTB. In Figure 6.13 the results and the corresponding TDEV is depicted.

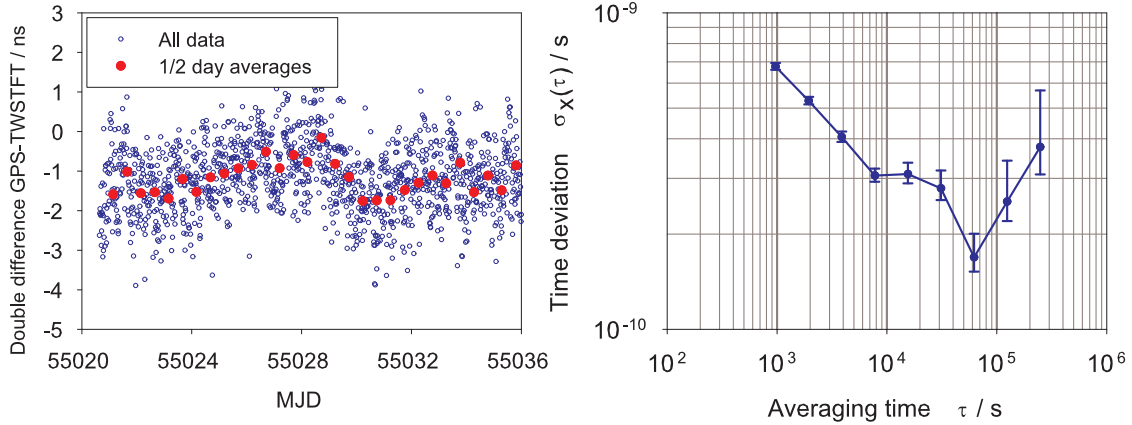


**Figure 6.13.:** GPS - TWSTFT double differences (left plot) and related TDEV (right plot). The mean value of the averaged data is -1.19 ns, the SD is 0.41 ns.

The left plot shows all data obtained with the interpolation method described in Subsection 6.2.4, as well as the averages. The TDEV justifies an averaging period of 1/2-day.

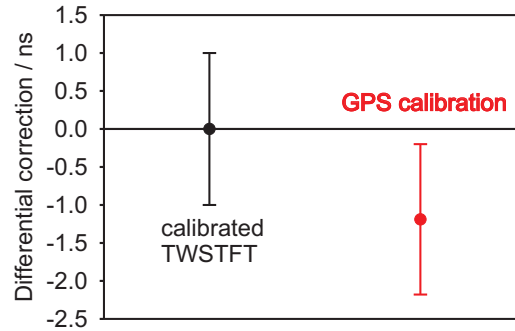


**Figure 6.14.:** Differential correction between the TWSTFT calibration and the new calibration value obtained with a relative GPS calibration.

Combining the SD of the averaged data around the mean with the GPS calibration uncertainty the TWSTFT calibration value is given by

$$C_{\text{TWSTFT}} = -1.19 \text{ ns} \pm 0.99 \text{ ns}. \quad (6.16)$$

The uncertainty of the TWSTFT calibration was stated as 1 ns [87]. The GPS-based result and the 2008 TWSTFT calibration result agree with each other within the combined uncertainty.

## 6.6. USNO-PTB Calibration

The USNO-PTB calibration campaign was done with the new calibration set-up described in Section 6.4. Thus the uncertainty contributions  $u_{b,9}$  and  $u_{b,10}$  vanish. In June 2010 the set-up was operated at PTB for nine days between MJD 55350 and MJD 55358. Then it was shipped to USNO and operated there for twelve days within the interval MJD 55400 to MJD 55411 in July and August 2010. After it was sent back, the second operation at PTB was done between MJD 55448 and MJD 55456 in August 2010.

In Table 6.7 the types of receivers involved at PTB and USNO and the related data output are specified. The nomenclature is handled with the same principles as explained in the METAS-PTB section. Data of the fixed GTR50 receiver at PTB (PT08) were not available for this campaign. Hence, nine P3 links, six PPP links, and one C/A code link between the TTS-3 at PTB (PT05) and an old TTS-2 at USNO (US01) can be evaluated. The TTS-2 is the precursor of the TTS-3, providing only L1 C/A code CGGTTS data.

**Table 6.7.:** Receivers at PTB and USNO and the related data output.

Institute	Receiver	C/A	P3	RINEX
PTB	Ashtech Z12-T	- - -	PT02	PTBB
	Ashtech Z12-T	- - -	PT03	PTBG
	AOS TTS-3	PT05	PT06	- - -
USNO	Ashtech Z12-T	- - -	USNO	USNO
	AOS TTS-2	US01	- - -	- - -
	Ashtech Z12-T	- - -	US03	USN3
	NovAtel ProPak	- - -	NOV1	NOV1

The "USNO" receiver constitutes a special case. The antenna is not mounted at the main antenna site of the laboratory, because this receiver is located at a different building. The baseline between the TR and USNO is about 176 m. Furthermore it is not connected to UTC(USNO). It is referenced to a different clock that is kept close in frequency to UTC(USNO) but with a large phase offset.

The uncertainty contribution due to a wrong position was again found to be  $u_{b,17} = 0.26$  ns at PTB. At USNO the error was estimated as  $e_h(\text{USNO}) =$

2.13 ns/m. The absolute value of the difference between the a priori position and the PPP estimates is 0.141 m, and thus  $u_{b,18} = 0.30$  ns.

The  $\delta t_0$  measurement with the TIC integrated into the calibration set-up was done at PTB before and after each CCD measurement and at USNO before and after the CCD measurement. Exemplarily the measurement at PTB before CCD1 is depicted in Figure 6.15.

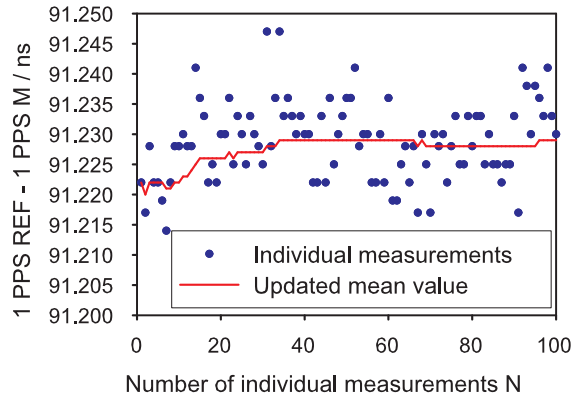


**Figure 6.15.:**  $\delta t_0$  measurement at PTB.

The blue dots are the individual measurements, the red line is the mean value of  $N$  individual measurements. The jitter at PTB, and thus the uncertainty  $u_{b,11}$ , was calculated to be 0.01 ns. At USNO the uncertainty is  $u_{b,12} = 0.05$  ns. This significantly higher jitter is due to the fact that the 1 PPS M signal appeared before the 1 PPS REF signal. The TIC measurements become more noisy for such long time intervals (approaching 1 s).

Usually TICs are based on counting the zero crossings of a reference frequency between start and stop signal. Interpolation processes are applied to minimize the error which occurs due to the missing correlation between these signals and the zero crossings [88]. However, the performance of the TIC is limited by the instability of the clock at the measured time interval [78]. Since atomic clocks are dominated by white frequency noise for averaging times of several seconds the product of the measurement interval and the instability at this interval is increasing for longer intervals (cf. the definition of the TDEV in Section 2.1).

In both laboratories the first measurement was in agreement with the second measurement within 0.05 ns, supporting the estimate of 0.1 ns uncertainty of the connection to the local UTC ( $u_{b,11}$ ,  $u_{b,2}$ ).

In the USNO-PTB campaign the measurement of the offset  $\delta t_0$  required more efforts, because the UTC(USNO) reference point is defined at the endpoint of a female BNC connector. An additional cable with two male BNC connectors was needed to establish the connection to the 1 PPS REF connector of the calibration set-up. This cable was also used at PTB in order that its delay cancels out and

the uncertainty of the determination of the reference point at USNO ( $u_{b,14}$ ) can be considered to be zero. At PTB the cable was interconnected between the set-up and the UTC(PTB) reference cable using a male to male BNC adapter. The delay of the adapter was determined to be 0.113 ns by an additional measurement with an uncertainty less than 10 ps. After adding this uncertainty geometrically to the uncertainty of the UTC(PTB) reference cable verification measurement, the overall uncertainty of the UTC(PTB) reference point determination is again 0.02 ns, if rounded to the second decimal.

In Figure 6.16 the CCD measurements at PTB are depicted. Offsets are again introduced for better visibility. As in the METAS-PTB campaign the Ashtech

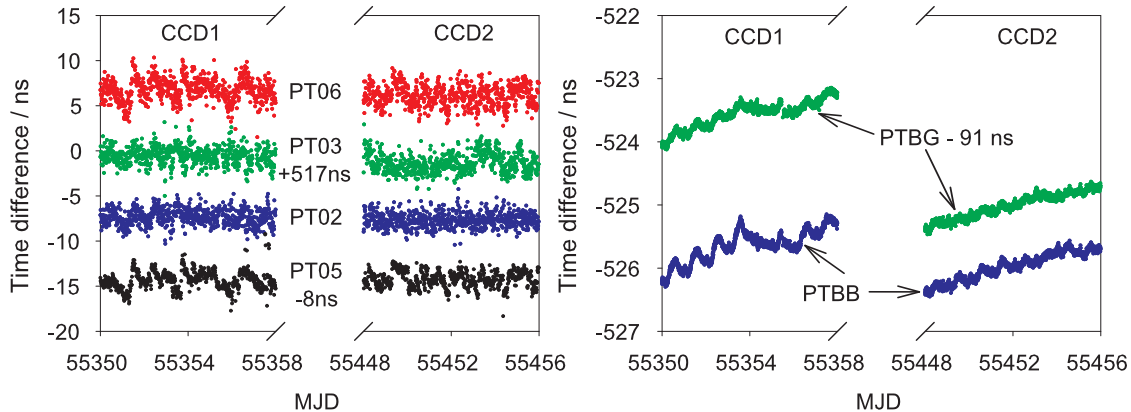


**Figure 6.16.:** Code (left) and PPP (right) CCD measurements at PTB before and after the calibration trip to USNO.

Z12-T phase measurements caused drifts in the PPP results. Figure 6.17 shows the CCD measurements at USNO.

It becomes apparent that the Ashtech receivers do not inevitably show up the drift behavior in the PPP results. The solution of the CCD measurement TR-USN3 is very stable. A disturbance happened in the measurement at MJD 55407, inducing the drift starting with a small phase shift on MJD 55407. It is visible in both the TR-USN3 and TR-NOV1 solution and is thus related to the TR. Since USNO is connected to a different clock this effect is below the noise level. Strictly speaking, the comparison TR-USNO is not a CCD measurement, but the results show that the coupling of USNO's clock to UTC(USNO) is very tight and this quasi CCD measurement can be treated as the others.

The TDEV plots are exemplarily shown for the USNO measurement in Figure 6.18. The right plot shows the typical TDEV for PPP CCD measurements. In the majority of cases it decreases until about 2400 s and then it increases. The averaging is done over 8 individual measurements.

All estimated averaging times are listed in Table 6.8.

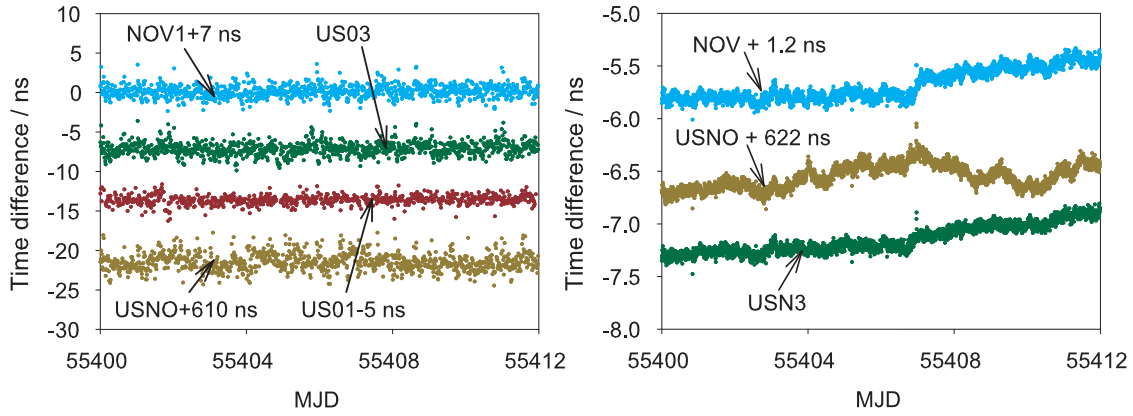


**Figure 6.17.:** Code (left) and PPP (right) CCD measurements at USNO.

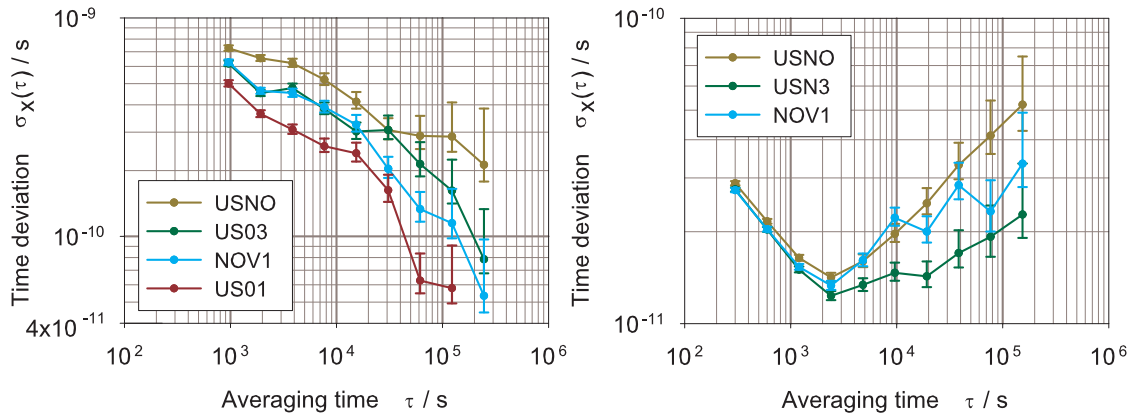


**Figure 6.18.:** Double logarithmic plots of the time deviations of the CCD measurements at USNO for code (left plot) and PPP (right plot).

In Table 6.9 the results at PTB are listed. After adding the internal delays (2.23) to the PPP results they are in good agreement with the P3 results.

The values obtained at USNO are shown in Table 6.10. In contrast to PTBB and PTBG, at USNO the internal delays are applied to the RINEX data, as it is done for receivers of type GTR50. Hence the P3 and PPP results are directly at the same order of magnitude. The values for P3 and PPP are in good agreement for US03/USN3 and NOV1. The discrepancy of about 3 ns for the receiver USNO is due to an error of the a priori position used for the P3 generation of about 1.5 m. If the position will be corrected in the future to decrease the noise, the calibration value  $C_2$  will be no longer valid for this receiver.



**Table 6.8.:** Estimated data averaging times.

PTB				USNO		
Type	FR	AVT1	AVT2	Type	FR	AVT
P3	PT02	1 day	1 day	P3	USNO	1 day
P3	PT03	1 day	7680 s	C/A	US01	1 day
C/A	PT05	No avg.	1920 s	P3	US03	1 day
P3	PT06	7680 s	3840 s	P3	NOV1	1 day
PPP	PTBB	1200 s	2400 s	PPP	USNO	2400 s
PPP	PTBG	1200 s	2400 s	PPP	USN3	2400 s
				PPP	NOV1	2400 s

**Table 6.9.:** Results of the CCD measurement at PTB. Values are rounded to the second decimal. The underlined value is chosen as the uncertainty  $u_{a,PTB}$ . The values in brackets are the calibration values after applying the internal delays according to (2.23).

Type	FR	CCD1 / ns	CCD2 / ns	$C_1$ / ns	dCCD / ns	SD1 / ns	SD2 / ns
P3	PT02	-7.32	-7.65	-7.49	<u>0.33</u>	0.17	0.09
P3	PT03	-517.57	-518.36	-517.96	<u>0.79</u>	0.15	0.78
C/A	PT05	-6.33	-6.18	-6.25	-0.15	<u>1.05</u>	0.82
P3	PT06	6.79	6.19	6.49	0.59	<u>0.98</u>	0.92
PPP	PTBB	-525.65 (-7.21)	-525.98 (-7.53)	-525.81 (-7.37)	<u>0.33</u>	0.25	0.22
PPP	PTBG	-432.58 (-516.78)	-434.03 (-518.23)	-433.30 (-517.50)	<u>1.45</u>	0.28	0.33

Table 6.11 shows the calibration values and the corresponding uncertainty for all possible links between USNO and PTB.

The uncertainties are all well below 2 ns, as for the METAS-PTB calibration. The link which is used by the BIPM for the TAI computation if no TWSTFT data are available is the link USN3-PTBB. The small calibration value correction indicates that the internal delays of the USN3 receiver had been aligned to a TWSTFT calibration performed before, relying on links discussed subsequently.

All general statements made on link calibrations above in terms of the METAS-PTB campaign are also valid for the USNO-PTB campaign.

**Table 6.10.:** Results of the CCD measurements at USNO. Values are rounded to the second decimal.

Type	FR	C <sub>2</sub> / ns	SD / ns
P3	USNO	-631.45	0.30
C/A	US01	-8.59	0.11
P3	US03	-7.14	0.19
P3	NOV1	-6.85	0.12
PPP	USNO	-628.55	0.11
PPP	USN3	-7.15	0.13
PPP	NOV1	-6.88	0.14

Until June 2010 two TWSTFT links using two different communication satellites were maintained between USNO and PTB. The first one was operating in the X-band and turned off in June 2010, the second one in the Ku-band was still operational at the time of writing this text (December 2010).

The advantage of the X-band link was that the same transponder was used at USNO and PTB. Thus relative calibrations with a traveling X-band station were possible, as for the European TWSTFT links in the Ku-band. In contrast the USNO-PTB Ku-band link uses different transponders for Europe and the USA and cannot be calibrated without involving GPS [56, 89].

Since the X-band link was periodically calibrated with a traveling TWSTFT station [56] a comparison of a new calibrated GPS link can be used in order to verify the GPS calibration (Table 6.11). The new calibration value is applied to US03-PT02 P3 data taken during the last 25 days when the TWSTFT X-band link was used for TAI computation. Due to the very long baseline between USNO and PTB it was decided to evaluate the GPS data in the AV mode. After applying the  $3\sigma$  filter to the GPS-TWSTFT double difference data about 5% of the data were discarded. The TDEV (Figure 6.19) allows for daily averages. After averaging the daily mean values, calculating the SD of the averages around the mean, and adding it geometrically to the GPS calibration uncertainty the result for the X-band calibration value is

$$C_{\text{TWSTFT,X}} = -0.71 \text{ ns} \pm 0.92 \text{ ns} . \quad (6.17)$$

This demonstrates that the GPS calibration campaign was successful and that a TWSTFT link can be calibrated with an uncertainty less than 1 ns in favorable cases. Figure 6.20 depicts the agreement of the GPS calibration and the 2007 X-band calibration within the combined uncertainty. The uncertainty of the X-band

**Table 6.11.:** Calibration values and corresponding uncertainties for all possible GPS links between USNO and PTB. The values are rounded to the second decimal. The values in brackets are the calibration values after applying the internal delays according to (2.23).

Type	Link	$C_{\text{GPS}} / \text{ns}$	$u_a / \text{ns}$	$u_b / \text{ns}$	$U / \text{ns}$
C/A	US01-PT05	2.27	1.06	0.58	1.21
P3	USNO-PT02	623.97	0.45	0.58	0.73
P3	USNO-PT03	113.49	0.84	0.58	1.02
P3	USNO-PT06	637.94	1.02	0.58	1.18
P3	US03-PT02	-0.35	0.38	0.58	0.69
P3	US03-PT03	-510.82	0.81	0.58	1.00
P3	US03-PT06	13.63	0.99	0.58	1.15
P3	NOV1-PT02	-0.63	0.35	0.58	0.68
P3	NOV1-PT03	-511.11	0.80	0.58	0.99
P3	NOV1-PT06	13.34	0.99	0.58	1.15
PPP	USNO-PTBB	102.57 (621.18)	0.35	0.52	0.63
PPP	USNO-PTBG	195.25 (111.05)	1.46	0.52	1.55
PPP	USN3-PTBB	-518.83 (-0.22)	0.35	0.52	0.63
PPP	USN3-PTBG	-426.16 (-510.36)	1.46	0.52	1.55
PPP	NOV1-PTBB	-519.09 (-0.49)	0.36	0.52	0.63
PPP	NOV1-PTBG	-426.42 (-510.62)	1.46	0.52	1.55

calibration was estimated as 0.88 ns. The complete history of X-band calibrations since 2003 is outlined in the reference [56].

The calibration of the operational Ku-band link was done within a period after the GPS calibration campaign. Due to the long period of 64 days an averaging period of 4 days was chosen (Figure 6.21).

The new calibration value for the USNO-PTB Ku-band link was found to be

$$C_{\text{TWSTFT,Ku}} = 3.67 \text{ ns} \pm 1.26 \text{ ns}. \quad (6.18)$$

Here the uncertainty is also well below 2 ns. However, although the Ku-band link was aligned to the X-band calibration [56] the 3.67 ns are remarkable and neces-

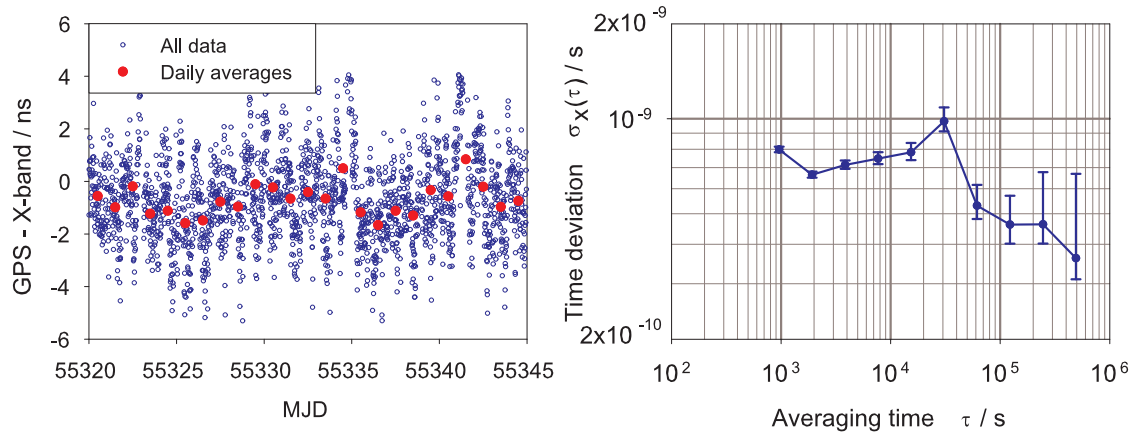


**Figure 6.19.:** GPS - X-band double differences (left plot) and related TDEV (right plot).

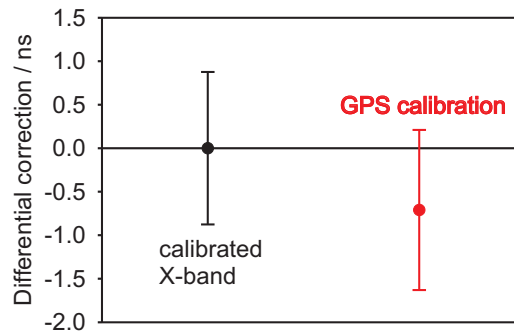


**Figure 6.20.:** Differential correction between the 2007 X-band calibration value and the new calibration value obtained with the relative GPS calibration.

sitate an explanation: A long term comparison of the X-band and the Ku-band link shows an increase of the noise and a reduced stability since the first quarter of 2010. This is also visible in the comparison between GPS PPP and the Ku-band. The same effects are also visible in the link comparisons between European laboratories equipped with TWSTFT stations and PTB. They are probably caused by a reduction of the bandwidth available for time comparisons on the communication satellite connecting the US and European laboratories.

However, both the X-band and the Ku-band results shown here confirm that a relative GPS calibration can be used as an alternative to cost effective TWSTFT calibrations also on long intercontinental baselines, since the uncertainty at the moment of the calibration is at the same low level as with TWSTFT equipment.

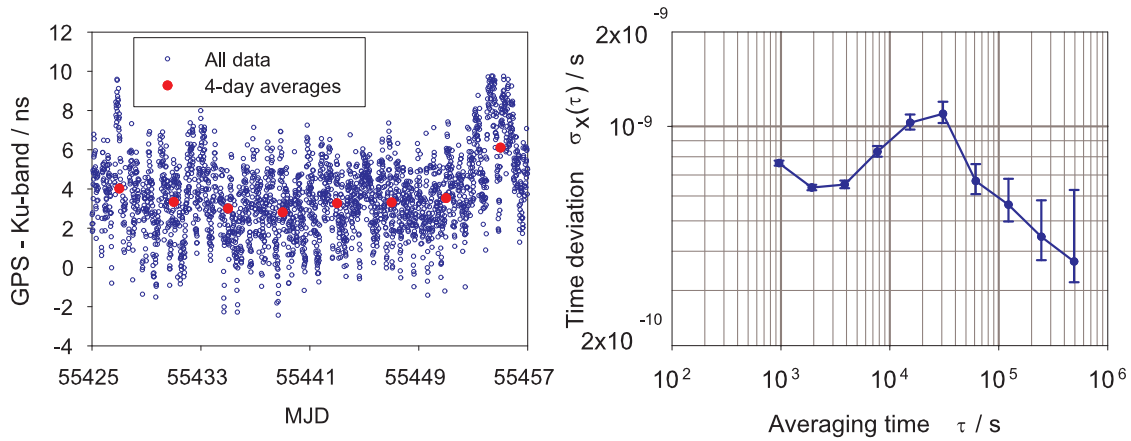


Figure 6.21.: GPS - Ku-band double differences (left plot) and related TDEV (right plot).

## 6.7. Suggestions for further Reductions of the Uncertainty

Due to the traveling TIC integrated into the calibration set-up the main part of the uncertainty of the  $\delta t_0$  determination vanishes. However, other non-negligible uncertainties related to 1 PPS time interval measurements are part of the uncertainty budget. In order to cancel out more error contributions the set-up shall be updated as depicted in Figure 6.22.

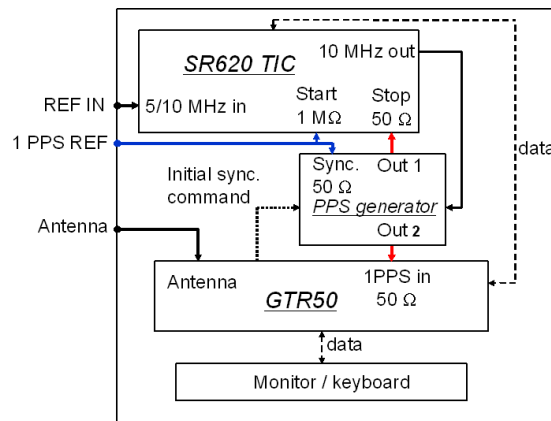


Figure 6.22.: Proposal for a future update of the calibration set-up.

If the 1 PPS measurement signal is generated with a traveling 1 PPS generator integrated into the set-up, the trigger level timing error of the stop channel of the traveling TIC as well as the trigger timing level error of the receiver's internal

counter will completely cancel out, because the signal characteristic is the same in all laboratories, as for the stop signal of the receiver's internal TIC which is always provided with the 1 PPS generated by the GPS board.

In this case no 1 PPS IN signal is needed. The 1 PPS provided to the TR is derived from the external reference frequency. To ensure proper operation of the receiver, initially this signal has to be synchronized with the 1 PPS REF signal, in order to keep it in close agreement with the GPS time. The relationship to the local UTC is then again established by a TIC measurement. If the reference frequency signal is interrupted during the CCD measurement, the initial synchronization and the TIC measurement have to be repeated. The reference frequency must be the local UTC frequency.

The uncertainty contributions  $u_{b,3}$  and  $u_{b,4}$  will reduce to 0.04 ns and  $u_{b,5}$  and  $u_{b,6}$  will be zero. Since the only reason of the initial synchronization of the 1 PPS generator is to ensure that the 1 PPS signal provided to the GTR50 does not deviate too much from the internal GPS signal, as stated above, the trigger level timing error of the generator has no further influence on the measurements.

To calculate the overall uncertainty the classical root mean square method was used here (6.12). By now, new rules for the uncertainty evaluation based on statistical models have been formulated and are summarized in BIPM's "Guide to the expression of uncertainty in measurement" (GUM) [90]. This rules could become the mandatory standard in metrology in the future. Thus, the uncertainty of future calibration campaigns should be evaluated according to the GUM. For this purpose a detailed knowledge of the distribution of the measurement values and the systematic error contributions is required [91]. In this framework, especially the so-called nonlinearity effect of the TIC, related to the relationship between the reference frequency's zero crossing and the 1 PPS signals, has to be studied in detail. The expected distribution function of the error contributions is used to calculate weights for each of the uncertainty contribution.

## 7. Summary and Outlook

In this work the principles of the GPS technology for time and frequency comparisons and the relevant models for the correction of physical influences have been explained. The improvement of the short term instability due to the usage of correction data calculated from a worldwide network of reference stations, namely the IGS network, within a data analysis strategy called precise point positioning (PPP) has been pointed out.

A highly precise mobile frequency reference based on a passive hydrogen maser and a state-of-the-art time and frequency transfer GPS receiver was described. The local evaluation of the equipment and the remote comparison of the passive maser to PTB's active masers has shown that the maser can be referenced to PTB's primary standards at an averaging time of  $10^4$  s using the PPP method.

The PPP method was subject of detailed research by comparing different software packages with each other. A correlation was found between the clock offset estimation and the position estimates. Furthermore, the accuracy of the position estimates was also found to be related to the instability of the reference frequency connected to the GPS receivers. This should be examined specifically in a future analysis, by connecting a GPS receiver to different reference sources with different short and medium term instability characteristics. A similar effect was not found in the troposphere estimates. This correction seems more to be related to the geographic location of the antenna. Also here future examinations are necessary.

By using only the carrier-phase measurements and a fixed position of the antenna frequency transfer on different baselines involving different reference frequency sources was established. The influence of the troposphere model and the solid Earth tide correction was thus studied in detail. It was found that on relatively short baselines the Earth tides can be neglected. This is also valid on European baselines, if the instability is limited by the noise of a commercial caesium clock. In case of a very long intercontinental baseline the modeling of the Earth tides is essential for frequency comparisons at the instability level of an active hydrogen maser. Surprisingly, a relative simple model for the troposphere is sufficient in all cases. Future research should verify this and examine the influences of the models on shorter continental baselines by involving clocks with better instability (masers).

Different receivers were analyzed in view of long and short term stability. Thereby the requirements on the equipment for time and frequency transfer were outlined. For time and frequency comparisons receivers which are capable to operate con-

tinuously without interruptions and which are decoupled from the environmental temperature are needed. New concepts for future improvements were proposed.

The first GPS common-clock measurement between two remote sites is shown. The local clocks were canceled out by comparing the GPS data to the measurements of an optical fiber operated for frequency transfer between the institutes PTB and IQO at the LUH. The measurement period was relatively short and the receiver operations were affected by effects which have caused variations at the 200 ps level. In future experiments a longer measurement period is desirable. Additionally, all effects which could influence the measurement should be detected, analyzed, and removed as far as possible in advance.

The calibration of the operational time links between METAS and PTB and USNO and PTB by means of a traveling GPS receiver was shown. These two links were of particular interest, because calibrated TWSTFT links were operated in parallel in both cases. An uncertainty at the nanosecond level at the moment of calibration was achieved in both calibration campaigns. With a new traveling calibration set-up, based on a GPS receiver and a time interval counter, systematic effects in the local UTC reference point determination were canceled out. It has also been demonstrated that relative GPS calibrations are a good alternative for cost and labor intensive TWSTFT calibration campaigns. For further reduction of the uncertainty an update of the calibration set-up is planned. Campaigns involving the National Physical Laboratory (NPL) in Teddington, GB, the NICT, and the National Institute of Metrology (NIM) in Beijing, China, are planned.



# Appendix

## A. Mathematical Description of the Coordinate Systems

The transformation between a vector  $\vec{V}_{ECI}$  in the ECI system and a vector  $\vec{V}_{ECEF}$  in the ECEF system is given by

$$\vec{V}_{ECEF} = R_M R_S R_N R_P \vec{V}_{ECI} . \quad (\text{A.1})$$

Reading from left to right the matrices describe the polar motion, the nutation, the Earth rotation, and the precession, respectively. Details can be found in the references [5, 92].

The ECEF system can be expressed with the geodetic coordinates  $\varphi$ ,  $\theta$  and  $h$ , representing the geodetic latitude, longitude and height, respectively, taking into account the flattening of the Earth (Figure A.1).

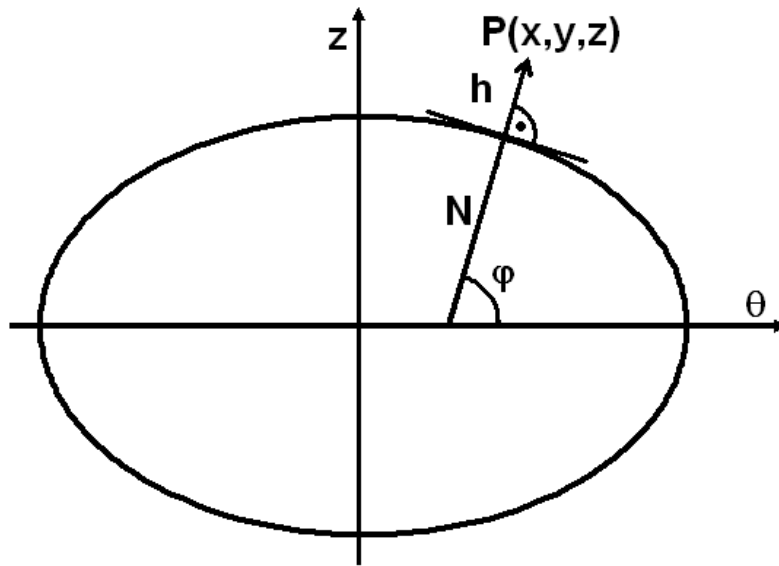


Figure A.1.: Geometry of the curvature of the Earth ellipsoid.

The transformation between the cartesian coordinates and the geodetic coordinates is given by

$$\begin{aligned} x &= (N + h) \cos(\varphi) \cos(\theta), \\ y &= (N + h) \cos(\varphi) \sin(\theta), \\ z &= [N(1 - e_E^2) + h] \sin(\varphi), \end{aligned} \quad (\text{A.2})$$

and the inverse transformation reads

$$\begin{aligned} \theta &= \arctan\left(\frac{y}{x}\right), \\ \varphi &= \arctan\left(\frac{z}{\sqrt{x^2 + y^2} \left(1 - e_E^2 \frac{N}{N+h}\right)}\right), \\ h &= \frac{\sqrt{x^2 + y^2}}{\cos(\varphi)} - N. \end{aligned} \quad (\text{A.3})$$

In (A.2) and (A.3)  $e_E$  is the eccentricity of the Earth ellipsoid and the radius of the curvature can be expressed as

$$N = \frac{a_E}{\sqrt{1 - e_E^2 \sin^2(\varphi)}}, \quad (\text{A.4})$$

with  $a_E$  the semi-major axis of the Earth ellipsoid. The transformation (A.3) has to be solved by iteration, because latitude and height are not independent from each other.

Different realizations of the ECEF system with different parameters  $a_E$  and  $e_E$  are possible and in use. The ECEF reference frame used by the GPS control segment to predict the ephemeris data broadcasted with the navigation message is the World Geodetic System 1984 (WGS 84), while the frame of the GLONASS is the PZ-90 system [4]. To improve the precision ephemeris data provided by a different source are often employed in post-processing applications. The reference frames of this ephemeris data can differ from the reference frames broadcasted by the satellites, e.g. the frame used by the International GNSS Service (IGS) is the International Terrestrial Reference Frame (ITRF) which is in agreement with the conventions of the International Earth Rotation Service (IERS).

The general coordinate transformation between reference frames (e.g. WGS84, PZ-90, ITRF) is given by [93]

$$\vec{r}_1 = T_{1,2} + \Psi_{1,2} R_{1,2} \vec{r}_2, \quad (\text{A.5})$$

where  $r_1$  and  $r_2$  are the coordinates in a reference frame 1 and 2, respectively.  $T_{1,2}$  is a translation matrix,  $\Psi_{1,2}$  is a scale factor, and  $R_{1,2}$  is a rotation matrix.

To calculate the azimuth and the elevation of a satellite a transformation to the local coordinates  $(x_L, y_L, z_L)$  is needed.

The  $x_L$ -axis is pointing to the north and the  $y_L$ -axis is pointing to the east. The transformation from the ECEF coordinates to the local coordinates is therefore realized by one reflection and two rotations:  $R_L(\varphi, \theta) = S_x R_y(\pi/2 - \varphi) R_z(\theta)$ . The matrices are given by

$$\begin{aligned} R_y(\pi/2 - \varphi) &= \begin{pmatrix} \cos(\pi/2 - \varphi) & 0 & -\sin(\pi/2 - \varphi) \\ 0 & 1 & 0 \\ \sin(\pi/2 - \varphi) & 0 & \cos(\pi/2 - \varphi) \end{pmatrix}, \\ S_x &= \begin{pmatrix} -1 & 0 & 0 \\ 0 & 1 & 0 \\ 0 & 0 & 1 \end{pmatrix}, \quad R_z(\theta) = \begin{pmatrix} \cos(\theta) & \sin(\theta) & 0 \\ -\sin(\theta) & \cos(\theta) & 0 \\ 0 & 0 & 1 \end{pmatrix}. \end{aligned} \quad (\text{A.6})$$

Now any vector  $\vec{V}_{ECEF}$  in the ECEF coordinate system can be transformed to the receiver antenna's local coordinates using  $\vec{V}_L = R_L \vec{V}_{ECEF}$ .

The vector pointing from the antenna to one satellite  $s$  in the ECEF system at the time of signal emission  $t_s$  and the receiver's antenna at the time of signal reception  $t_r$  is

$$\vec{\rho}_s = (x_s(t_s) - x_r(t_r), y_s(t_s) - y_r(t_r), z_s(t_s) - z_r(t_r)) , \quad (\text{A.7})$$

with the satellite's coordinates  $(x_s, y_s, z_s)$  and the receiver antenna's coordinates  $(x_r, y_r, z_r)$ . After transforming (A.7) to the local coordinates the azimuth and elevation angles are calculated by

$$az = \arctan\left(\frac{\rho_{L,y}}{\rho_{L,x}}\right), \quad el = \arctan\left(\frac{\rho_{L,z}}{\sqrt{\rho_{L,y}^2 + \rho_{L,x}^2}}\right). \quad (\text{A.8})$$

## B. Mathematical Description of the Satellite Motion

A short mathematical description of the satellite motion in the orbital planes is necessary to understand the derivation of relativistic effects (Section 2.4.2) which have to be applied to the measurements in order to get correct results.

In each orbital plane the satellites are orbiting in the Newtonian potential  $V$  on an ellipse with one focus being the center of mass of the Earth. The two dimensional instantaneous position within the orbital plane can be described by Cartesian coordinates  $(p, q)$  with the origin at the center of mass of the Earth:

$$p = r_s \cos(\nu), \quad q = r_s \sin(\nu). \quad (\text{B.9})$$

The angle  $\nu$  is measured from the perigee along the orbit to the satellite's position [38]. The radius  $r_s$  is given by

$$r_s = \frac{a(1 - e^2)}{1 + e \cos(\nu)}, \quad (\text{B.10})$$

where  $a$  is the semi-major axis of the ellipse and  $e$  is the orbit eccentricity. Due to the conservation of the total energy the velocity  $v_s$  can be expressed as

$$v_s = \sqrt{GM_E \left( \frac{2}{r_s} - \frac{1}{a} \right)}. \quad (\text{B.11})$$

$G$  is the constant of gravitation and  $M_E$  is the mass of the Earth.

The radius  $r_s$  and the angle  $\nu$  are connected via equation (B.10), but the time dependence of this two variables is unknown. In order to relate the satellite position to a time variable it is useful to define an auxiliary circle with radius  $a$  and its center point coinciding with the center of the ellipse, as depicted in Figure B.2. By a vertical projection of the satellite to the auxiliary circle a new angle  $E$ , called the eccentric anomaly, can be defined [5].

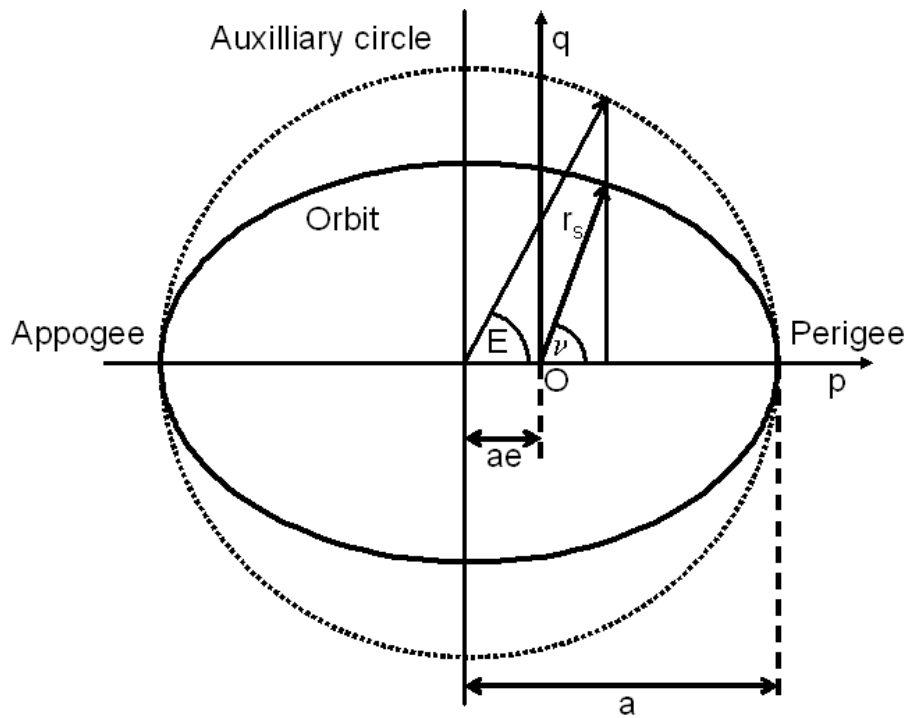


**Figure B.2.:** The definition of the eccentric anomaly.

With this new variable the coordinates  $(p, q)$  and the radius  $r_s$  can be rewritten approximately as

$$p = a \cos(E) - ae, \quad q \approx a\sqrt{1 - e^2} \sin(E), \quad r_s = a(1 - e \cos(E)). \quad (\text{B.12})$$

The equation for  $p$  is a direct consequence of the geometry shown in Figure B.2, while the equation for  $q$  is obtained by substituting the equation for  $p$  in the ellipse

equation  $p^2/a^2 + q^2/b^2 = 1$ , with the semi-minor axis given by  $b = a\sqrt{1 - e^2}$ . Small terms containing  $e$  have been neglected, because  $e \ll 1$  for a GNSS satellite.

The components of the velocity vector are given as the time derivative of (B.12)

$$\dot{p} = \frac{dp}{dt} = -a \sin(E) \frac{dE}{dt}, \quad \dot{q} = \frac{dq}{dt} = a\sqrt{1 - e^2} \cos(E) \frac{dE}{dt}. \quad (\text{B.13})$$

With the help of the equations (B.12) and (B.13) and the conservation of the angular momentum the Keplerian equation

$$E - e \sin(E) = \sqrt{\frac{GM_E}{a^3}} (t - t_p) \quad (\text{B.14})$$

can be derived [5,38]. The integration constant  $t_p$  is chosen as the time at which the satellite is at perigee ( $E(t_p) = 0$ ). The eccentric anomaly is now associated with the coordinate time  $t$ . Differentiating both sides of equation (B.14) with respect to the time yields

$$\frac{dE}{dt} = \sqrt{\frac{GM_E}{a^3}} \frac{1}{1 - e \cos(E)}, \quad (\text{B.15})$$

which can be used in equation (B.13).

The position of the satellite in the orbital plane can be transformed to the ECI coordinates by three succeeded three-dimensional rotations using the so-called Keplerian elements, which are angles related to the inclination, the orientation of the angular momentum, and the direction of the perigee. A detailed description is given in the reference [5].

## C. CGGTTS Data

Below a cutout of a typical CGGTTS file C/A-code file is shown. The header includes the fixed position which is manually entered to the processing software that generates the file. INT DLY, CAB DLY, and REF DLY represent the antenna's signal delay inside the receiver, the antenna cable delay, and the delay of the 1 PPS reference signal, respectively. In case of a P3 CGGTTS file the internal delays for P1 and P2 are listed separately. The relevant column is REFGPS, representing the offset of the reference timescale with respect to the GPST for each satellite tracked at a particular epoch.

```
GGTTS GPS DATA FORMAT VERSION = 01
REV DATE = 2009-06-08
RCVR = GTR50 0806091 1.6.1
CH = 20
IMS = GTR50 0806091 1.6.1
LAB = PTB
X = +3844056.75 m
Y = +709664.09 m
Z = +5023131.73 m
FRAME = ITRF2000
COMMENTS = NO COMMENTS
```

INT DLY = -32.2 ns  
 CAB DLY = 211.4 ns  
 REF DLY = 45.1 ns  
 REF = UTC(PTB)  
 CKSUM = 42

PRN	CL	MJD	STTIME	TRKL	ELV	AZTH	REFSV	SRSV	REFGPS	SRGPS	DSG	IOE	MDTR	SMDT	MDIO	SMDI	MSIO	SMSI	ISG	CK
			hhmmss	s	.1dg	.1dg	.1ns	.1ps/s	.1ns	.1ps/s	.1ns	.1ns	.1ns	1ps/s	.1ns	1ps/s	.1ns	1ps/s	.1ns	
3	FF	55038	000200	780	286	1658	-4249420	-55	+133	-3	9	057	169	+40	91	+14	65	-17	22	2A
11	FF	55038	000200	780	512	2813	+122052	+20	+190	+3	6	077	104	-11	62	-6	30	-18	21	E0
14	FF	55038	000200	780	404	930	+746559	-59	+184	-4	10	112	124	-7	73	-3	49	-7	34	F0
19	FF	55038	000200	780	581	1742	-176682	+10	+219	-5	6	023	95	+8	57	+5	39	+62	18	F8
22	FF	55038	000200	780	317	588	-1947103	+4	+134	-5	8	065	154	+29	86	+11	19	-119	48	2C
32	FF	55038	000200	780	397	2154	-2260066	+76	+211	+14	9	035	126	-21	74	-10	69	-6	29	30
3	FF	55038	001800	780	216	1661	-4249488	-75	+115	-24	11	057	220	+70	105	+16	64	+37	28	5A
11	FF	55038	001800	780	582	2810	+122079	+26	+201	+9	8	077	95	-8	57	-4	26	-8	24	E3
14	FF	55038	001800	780	421	833	+746507	-62	+185	-6	7	112	120	-2	71	-1	48	+5	29	D6
19	FF	55038	001800	780	504	1723	-176675	+21	+212	+6	7	023	105	+12	63	+7	57	-15	26	07
22	FF	55038	001800	780	252	588	-1947102	-7	+127	-17	10	065	189	+46	98	+14	35	-4	25	32
32	FF	55038	001800	780	473	2179	-2259998	+71	+218	+9	7	035	110	-14	65	-8	47	-3	29	2E
11	FF	55038	003400	780	653	2783	+122091	+20	+197	+3	6	077	89	-5	54	-3	42	-4	22	D7
14	FF	55038	003400	780	421	735	+746448	-58	+180	-2	7	112	120	+2	71	+1	45	-10	27	DA
19	FF	55038	003400	780	427	1715	-176664	+14	+208	-1	7	023	119	+18	70	+9	58	-72	35	1B
20	FF	55038	003400	780	293	2335	-763698	+7	+208	-3	10	002	165	-36	90	-13	63	+30	41	1A
32	FF	55038	003400	780	550	2205	-2259940	+63	+216	+0	7	035	99	-10	59	-5	59	-1	29	04
11	FF	55038	005000	780	719	2705	+122103	+14	+192	-3	5	077	85	-3	52	-1	30	+0	15	BA
14	FF	55038	005000	780	403	643	+746393	-52	+178	+4	7	112	125	+7	73	+3	23	-65	27	EA
19	FF	55038	005000	780	351	1713	-176659	+12	+199	-3	10	023	141	+27	80	+12	58	-19	39	35
20	FF	55038	005000	780	362	2368	-763694	+22	+202	+12	10	002	137	-23	78	-10	40	-18	27	31
32	FF	55038	005000	780	627	2231	-2259876	+61	+220	-2	5	035	91	-7	55	-4	55	-11	16	FB
11	FF	55038	010600	780	773	2514	+122113	+20	+186	+3	4	077	83	-1	51	-1	45	+21	17	CE
14	FF	55038	010600	780	370	564	+746327	-69	+166	-13	10	112	134	+13	77	+6	50	+7	35	0C
19	FF	55038	010600	780	276	1713	-176660	+3	+185	-11	10	023	174	+44	93	+14	41	-27	35	2D
20	FF	55038	010600	780	432	2403	-763687	-10	+199	-20	7	002	118	-16	70	-8	48	+23	22	1B
32	FF	55038	010600	780	704	2257	-2259820	+46	+216	-17	4	035	86	-4	52	-2	47	-42	20	0F
11	FF	55038	012200	780	789	2158	+122127	+21	+184	+4	6	077	82	+0	51	+0	45	+24	20	D4

...

## D. RINEX Data

Below a cutout of a typical 30 s RINEX file is shown. The header contains an approximate position estimated by the receiver using the C/A-code. Each data block represents all measurements made at a particular epoch. The initiatory line gives the year, the month, the day, the hour, and the minute in two digits, followed by the second. 0.1 microsecond data spacing would be possible in terms of this standard. The next entry is zero at almost all epochs, except in case of error events, like loosing the track to all satellites, or power failure, etc. Then the number of satellites is indicated, followed by the PRN numbers of each tracked satellite. The measurements are listed one below the other for each satellite. The sequence of the data is according to the header line "# / TYPES OF OBSERV". L1 and L2 are the carrier-phase measurements in cycles of the frequency, C1 is the C/A-code pseudorange, and P1 and P2 are the P-code pseudoranges.

2.10	OBSERVATION DATA	RINEX VERSION / TYPE
GTR50	PTB	2010-05-31 00:48:44 PGM / RUN BY / DATE
		COMMENT
MARKER		MARKER NAME
MARKER #		MARKER NUMBER
OBSERVER	PTB	OBSERVER / AGENCY
0708522	GTR50	REC # / TYPE / VERS
NAE07020087	Novatel GPS-702	ANT # / TYPE

3844055.5780	709663.0059	5023130.2924					APPROX POSITION XYZ
0.0000	0.0000	0.0000					ANTENNA: DELTA H/E/N
1	1						WAVELENGTH FACT L1/2
5	L1	L2	C1	P1	P2		# / TYPES OF OBSERV
30.000							INTERVAL
2010	5	30	0	0	0.0000000	GPS	TIME OF FIRST OBS
2010	5	30	23	59	30.0000019	GPS	TIME OF LAST OBS
15							LEAP SECONDS
30							# OF SATELLITES
							END OF HEADER
10	5	30	0	0	0.0000000	0	8 16 22 6 24 18 21 3 19
112790530.218	4	87888725.756	4	21463321.661	8	21463321.376	4 21463321.163 4
116637477.760	2	90886354.698	2	22195369.704	7	22195369.854	2 22195367.807 2
107203546.114	4	83535239.961	4	20400148.157	8	20400147.674	4 20400147.881 4
106115706.578	5	82687546.484	5	20193136.504	9	20193137.194	5 20193137.122 5
114193837.721	3	88982224.944	3	21730359.433	8	21730359.562	3 21730358.390 3
114011278.705	3	88839977.115	3	21695621.495	8	21695620.818	3 21695620.527 3
107782948.848	4	83986714.067	4	20510407.817	8	20510407.862	4 20510408.072 4
120201453.898	2	93663466.142	2	22873574.163	7	22873573.971	2 22873571.285 2
10	5	30	0	0	30.0000000	0	8 16 22 6 24 18 21 3 19
112859370.721	4	87942367.687	4	21476421.591	8	21476421.504	4 21476420.146 4
116557613.020	2	90824122.442	2	22180172.006	7	22180172.141	2 22180169.374 2
107174219.830	4	83512388.321	4	20394567.440	9	20394567.841	4 20394567.149 4
106128742.083	5	82697704.017	5	20195617.104	9	20195617.385	5 20195617.481 5
114173693.748	3	88966528.323	3	21726526.563	8	21726525.669	3 21726524.872 3
114070053.305	4	88885775.492	4	21706806.315	8	21706805.974	4 21706804.816 4
107728906.660	4	83944603.260	4	20500124.040	8	20500124.274	4 20500124.232 4
120113220.193	2	93594712.635	2	22856783.811	6	22856783.304	2 22856780.762 2
10	5	30	0	1	0.0000000	0	8 16 22 6 24 18 21 3 19
112928641.658	4	87996345.052	4	21489603.279	8	21489603.489	4 21489602.401 4
116478093.697	2	90762159.337	2	22165040.200	7	22165040.221	2 22165038.261 2
107145246.545	4	83489811.752	4	20389054.069	8	20389054.753	4 20389053.332 4
106142218.019	5	82708204.753	5	20198181.511	8	20198181.304	5 20198181.949 5
114154059.827	3	88951229.181	3	21722790.269	8	21722789.741	3 21722788.275 3
114129098.347	4	88931784.607	3	21718041.712	8	21718042.075	4 21718040.666 3
107675252.493	4	83902794.845	4	20489913.792	8	20489913.483	4 20489914.092 4
120025130.044	2	93526070.987	2	22840019.974	6	22840019.696	2 22840017.768 2
10	5	30	0	1	30.0000000	0	8 16 22 6 24 18 21 3 19
112998369.188	4	88050678.180	4	21502871.866	8	21502871.665	4 21502871.887 4
116398950.641	2	90700489.447	2	22149979.384	7	22149979.779	2 22149977.720 2
107116655.310	4	83467532.861	4	20383613.597	8	20383613.729	4 20383613.199 4
106156161.786	5	82719070.035	5	20200834.664	9	20200835.261	5 20200835.177 5
114134964.979	3	88936350.115	3	21719156.067	8	21719155.891	3 21719155.390 3
114188440.452	3	88978025.206	3	21729333.971	8	21729334.334	3 21729332.493 3
107622016.178	4	83861311.987	4	20479783.502	8	20479783.151	4 20479783.718 4
119937212.768	2	93457564.026	2	22823289.601	7	22823289.718	2 22823288.390 2
10	5	30	0	2	0.0000000	0	8 16 22 6 24 18 21 3 19

...

## E. P3 linear combination

The ionosphere is a dispersive medium, group velocity  $v_g$  and phase velocity  $v_p$  of a modulated signal are different and two different refractivities  $n_g$  and  $n_p$  exist which fulfill the conditions  $v_g n_g = c$  and  $v_p n_p = c$  ( $c$  is the speed of light in vacuum).

The relationship between  $n_g$  and  $n_p$  is given by [5]

$$n_g = n_p \left( 1 - f \frac{dn_p}{df} / n_p \right)^{-1}, \quad (\text{E.16})$$

with  $f$  being the frequency. In first order this can be expressed as

$$n_g = n_p + f \frac{dn_p}{df}, \quad (\text{E.17})$$

using the approximation formula

$$(1 - X)^{-1} = 1 + X - X^2 - \dots \quad (\text{E.18})$$

The phase refractivity can be represented in first order by

$$n_p = 1 + \frac{a_1}{f^2}. \quad (\text{E.19})$$

$a_1$  is related to the total electronic content (TEC) by  $a_1 = -40.3 \text{ TEC}$  [5]. Inserting (E.19) into (E.17) yields

$$n_g = 1 - \frac{a_1}{f^2}. \quad (\text{E.20})$$

Together with equation (2.8) one gets

$$\begin{aligned} \delta_{\text{ion,p}} = \text{Ion}_p &= \int (n_p - 1) ds = \int \frac{a_1}{f^2} ds = \frac{\int a_1 ds}{f^2} = \frac{A_1}{f^2}, \\ \delta_{\text{ion,g}} = \text{Ion}_g &= \int (n_g - 1) ds = \int -\frac{a_1}{f^2} ds = -\frac{\int a_1 ds}{f^2} = -\frac{A_1}{f^2}, \end{aligned} \quad (\text{E.21})$$

and thus  $\text{Ion}_p = -\text{Ion}_g$ .

In case of a single frequency reception (C/A-code on  $f_1$ ) the electron density  $N_e$  can be estimated using a model, and the ionospheric zenith path delay has to be mapped to the received signal path direction, as in the case of the troposphere.

By using both frequencies  $f_1$  and  $f_2$  the ionospheric error can be removed from the observation equations in first order. Two linear combinations consisting of the square of the two frequencies and the phase and group ionospheric delays (E.21) can be formed:

$$\begin{aligned} f_1^2 \text{Ion}_p(f_1) - f_2^2 \text{Ion}_p(f_2) &= f_1^2 \frac{A_1}{f_1^2} - f_2^2 \frac{A_1}{f_2^2} = 0, \\ f_1^2 \text{Ion}_g(f_1) - f_2^2 \text{Ion}_g(f_2) &= -f_1^2 \frac{A_1}{f_1^2} + f_2^2 \frac{A_1}{f_2^2} = 0. \end{aligned} \quad (\text{E.22})$$



Now a combination of the P1 and P2 code measurements with respect to the satellite  $s$  according to equation (2.4) can be constructed

$$f_1^2 P1_s - f_2^2 P2_s = (f_1^2 - f_2^2) [\rho_s(t_s, t_r) - (\delta t_r - \delta t_s)] + f_1^2 \Delta_{P1} + f_2^2 \Delta_{P2} , \quad (\text{E.23})$$

where the ionosphere error vanishes in first order. It is obvious that a scaling with  $1/(f_1^2 - f_2^2)$  yields a pseudorange formed by the measurements on the two frequencies

$$P3 = \frac{f_1^2 P1 - f_2^2 P2}{f_1^2 - f_2^2} . \quad (\text{E.24})$$

In the above equation the satellite index  $s$  has been omitted.

## F. Brief Derivation of Relativistic Corrections

The proper time increment  $d\tau_s$  of a satellite in the Newton gravitational potential

$$V = -GM_E/r_s \quad (\text{F.25})$$

is approximately given by [38]

$$-(cd\tau_s)^2 = - \left( 1 + \frac{2(V - \Phi_0)}{c^2} \right) (cdt)^2 + \left( 1 - \frac{2V}{c^2} \right) (dr_s^2 + r_s^2 d\vartheta_s^2 + r_s^2 \sin^2(\vartheta_s) d\phi_s^2) . \quad (\text{F.26})$$

$c$  denotes the speed of light.  $(r_s, \vartheta_s, \varphi_s)$  are the spherical polar coordinates of the satellite in the ECI reference frame. The coordinate time  $t$  is measured on the Earth geoid. Thus, the potential  $V - \Phi_0$  is the effective potential on the rotating geoid, with  $\Phi_0$  including a term related to the angular velocity of the Earth. It can be derived from a metric given in rotating ECI coordinates. This is extensively explained in reference [38].

The square of the satellite's velocity can be written as

$$v_s^2 = \frac{dr_s^2 + r_s^2 d\vartheta_s^2 + r_s^2 \sin^2(\vartheta_s) d\phi_s^2}{dt^2} . \quad (\text{F.27})$$

Equation (F.26) can be written as

$$d\tau_s^2 = \left[ 1 + \frac{2(V - \Phi_0)}{c^2} - \left( 1 - \frac{2V}{c^2} \right) \frac{v_s^2}{c^2} \right] dt^2 \approx \left[ 1 + \frac{2(V - \Phi_0)}{c^2} - \frac{v_s^2}{c^2} \right] dt^2 . \quad (\text{F.28})$$

The very small term including  $1/c^4$  can be neglected and the square root can be taken approximately with the help of the binomial expansion  $(A + X)^n = A^n + nA^{n-1}X + \dots$ , where the constant  $A = 1$ , the variable  $X = 2(V - \Phi_o)/c^2 - v_s^2/c^2$ , and  $n = 1/2$ , since the gravitational potential and the square of the satellite's velocity are small compared to the square of the speed of light:

$$d\tau_s = \left[ 1 + \frac{V - \Phi_0}{c^2} - \frac{v_s^2}{2c^2} \right] dt . \quad (\text{F.29})$$

To solve for the coordinate time increment the approximation formula (E.18) is used:

$$dt = \left[ 1 - \frac{V - \Phi_0}{c^2} + \frac{v_s^2}{2c^2} \right] d\tau_s . \quad (\text{F.30})$$

By assuming Keplerian orbits, equation (B.11) can be used for the velocity. After applying (F.25) and using  $3GM_E/2ac^2 - 4GM_E/2ac^2 = -GM_E/2ac^2$ , equation (F.30) reads

$$dt = \left[ 1 - \frac{3GM_E}{2ac^2} + \frac{\Phi_0}{c^2} - \frac{2GM_E}{c^2} \left( \frac{1}{a} - \frac{1}{r_s} \right) \right] d\tau_s . \quad (\text{F.31})$$

To get the correction that has to be applied to the satellite clock by a user on the Earth this has to be integrated along the path of the satellite parameterized with its proper time  $\tau_s$ . The first, the second, and the third term on the right hand side are constants and  $3GM_E/2ac^2 - \Phi_0/c^2 = -4.467 \cdot 10^{-10}$  [38].

The last term is related to the eccentricity of the orbit. It can be seen by using the radius from equation (B.12):

$$\Delta t_e = \frac{2GM_E}{c^2} \int_{\text{Path}} \left( \frac{1}{r_s} - \frac{1}{a} \right) d\tau_s = \frac{2GM_E}{c^2} \int_{\text{Path}} \frac{e \cos(E)}{1 - e \cos(E)} d\tau_s . \quad (\text{F.32})$$

The integration can be done by taking into account that the proper time and the coordinate time are approximately equal in the Newtonian limit:  $d\tau_s \approx dt$  [38]. The result of the integration is

$$\Delta t_e = \frac{2\sqrt{GM_E a}}{c^2} e \sin(E) + \text{const} . \quad (\text{F.33})$$

The integration constant can be neglected, because it is a just constant clock offset which can be removed by the clock steering of the master control station. With the help of the equations (B.12), (B.13), and (B.15) the product of the position and the velocity vector of the satellite can be written as

$$\vec{r}_s \cdot \vec{v}_s = p\dot{p} + q\dot{q} = \sqrt{GM_E a} e \sin(E) , \quad (\text{F.34})$$

and the eccentricity correction can be expressed as [4,38]

$$\Delta t_e = \frac{2}{c^2} \vec{r}_s \cdot \vec{v}_s . \quad (\text{F.35})$$

It can reach a maximum of 70 ns [4].

A second effect that has to be corrected by the user is the so-called Sagnac effect. It is related to the rotation of the Earth. The signal propagation time is given by  $\Delta t = t_R - t_T$ , with the reception time  $t_R$  and the transmitting time  $t_T$ . During this interval the displacement of the receiver due to the Earth rotation is  $\vec{v}\Delta t$ , with  $\vec{v}$  related to the angular velocity of the Earth. Neglecting all previously discussed effects, the signal propagation time is given by [94]

$$c^2 (\Delta t)^2 = (\vec{r}_R + \vec{v}\Delta t - \vec{r}_T)^2 , \quad (\text{F.36})$$

with  $\vec{r}_R$  and  $\vec{r}_T$  the receiver's and satellite's position at reception and transmission time, respectively. After defining  $\vec{R} = \vec{r}_R - \vec{r}_T$  and neglecting terms that are quadratic in  $\vec{v}/c$  is becomes

$$c^2 (\Delta t)^2 \approx \vec{R}^2 + 2\vec{v} \cdot \vec{R}\Delta t . \quad (\text{F.37})$$

The square root can be approximately solved by

$$c (\Delta t) \approx R + \frac{\vec{v} \cdot \vec{R}\Delta t}{R} , \quad (\text{F.38})$$

with  $R$  being the absolute value of  $\vec{R}$ . An approximate solution for  $\Delta t$  leads to

$$\Delta t \approx \frac{R}{c} + \frac{\vec{v} \cdot \vec{R}}{c^2} . \quad (\text{F.39})$$

With the angular velocity vector of the Earth  $\vec{\omega}_E$  and  $\vec{v} = \vec{\omega}_E \times \vec{r}_R$  the final Sagnac correction is given by [94]

$$\Delta t_S = \frac{1}{c^2} \vec{\omega}_E \cdot \vec{r}_R \times \vec{R} . \quad (\text{F.40})$$

Although it does not look like a relativistic effect at first sight, it can also be derived from a metric in a rotating reference frame [38].

## G. Estimation of the Ephemerides of Sun and Moon

The positions of the Moon and the Sun in their orbital planes are calculated with the help of equation (B.14). Also the Sun is treated as a body orbiting the Earth

in two dimensional coordinates according to the equations (B.12) and (B.13) [5]. Equation (B.14) can be rewritten as

$$E - e \sin(E) = M . \quad (\text{G.41})$$

$M$  is called the mean anomaly. According to IERS conventions [5] the mean anomaly of the Moon can be estimated by

$$\begin{aligned} M_{\text{Moon}} = & 134.96340251^\circ + 1717915923.2178'' \cdot T \\ & + 31.8792'' \cdot T^2 + 0.051635'' \cdot T^3 + 0.0002447'' \cdot T^4 . \end{aligned} \quad (\text{G.42})$$

It is given in angular dimensions. The time  $T$  is measured dimensionless in Julian centuries with the origin at the noon of January 1st 2000. Each Julian century consists of 36525 days. The relationship between  $T$  and MJD is

$$T = \frac{\text{MJD} - 51544.5}{36525} . \quad (\text{G.43})$$

The mean anomaly of the Sun is also approximated with a polynomial of order four:

$$\begin{aligned} M_{\text{Sun}} = & 357.52910918^\circ + 129596581.0481'' \cdot T \\ & + 0.5532'' \cdot T^2 + 0.000136'' \cdot T^3 + 0.0001149'' \cdot T^4 . \end{aligned} \quad (\text{G.44})$$

Equation G.41 has to be solved by iteration in order to get the eccentric anomaly  $E$  at each epoch. This can be done e.g. by starting with  $E_0 = M$  and inserting this into the next step  $E_1 = M + e \sin(E_0)$ .  $E_1$  is then used as the function value of the sinus function in the next step. In general, the iteration reads  $E_{n+1} = M + e \sin(E_n)$ , with  $n$  being the numbers of previous iterations. This is repeated until the difference  $|E_{n+1} - E_n|$  reaches a lower bound or until  $E$  is solved with sufficient numerical precision. The eccentricity of the Moon has to be set as  $e_{\text{Moon}} = 0.05490$  and the eccentricity of the Sun is given by

$$e_{\text{Sun}} = 0.016709114 - 0.000042052 \cdot T . \quad (\text{G.45})$$

The eccentric anomalies of the Moon and the Sun,  $E_{\text{Moon}}$  and  $E_{\text{Sun}}$ , are used to calculate the coordinates of these bodies in their orbital plane (B.12). The semimajor axis of the Moon and the Sun are  $a_{\text{Moon}} = 384401$  km and  $a_{\text{Sun}} = 1.495979005 \cdot 10^8$  km, respectively.

Subsequently, the position vectors of the Moon  $\vec{r}_{\text{Moon}} = (p_{x,\text{Moon}}, q_{y,\text{Moon}}, 0)$  and the Sun  $\vec{r}_{\text{Sun}} = (p_{x,\text{Sun}}, q_{y,\text{Sun}}, 0)$  are transformed to the ECI coordinates with the help of so-called Keplerian elements

$$\vec{r}_{\text{ECI}} = R_x(-\kappa)R_z(-\Omega_{\text{Moon}})R_x(-\zeta_{\text{Moon}})R_z(-\eta)\vec{r} . \quad (\text{G.46})$$

$R_x$  and  $R_z$  are rotation matrices around the  $x$ -axis and the  $z$ -axis, respectively.  $\kappa$  is the angle between the ecliptic plane and the equatorial plane and can be estimated in angular dimensions by

$$\kappa = 84381.448'' - 46.815 \cdot T - 0.00059 \cdot T^2 + 0.001813 \cdot T^3 . \quad (\text{G.47})$$

$\Omega$  is called the mean longitude of the ascending node of the Moon. The approximation formula reads

$$\begin{aligned} \Omega_{\text{Moon}} &= 125.04455501^\circ + 6962890.2665'' \cdot T \\ &+ 7.4722'' \cdot T^2 + 0.007702'' \cdot T^3 + 0.00005939'' \cdot T^4 . \end{aligned} \quad (\text{G.48})$$

Since the Sun is "orbiting" in the ecliptic plane,  $\Omega_{\text{Sun}}$  is zero. The inclination of the Moon is  $\zeta_{\text{Moon}} = 5.145396^\circ$ . For the Sun it is also zero.  $\eta$  is called argument of perigee. For the Moon it is calculated from the relation

$$\eta_{\text{Moon}} = \arctan\left(\frac{\tan(F_{\text{Moon}})}{\zeta_{\text{Moon}}}\right) - \nu_{\text{Moon}} , \quad (\text{G.49})$$

where  $F_{\text{Moon}}$  is called mean longitude of the Moon and given by

$$\begin{aligned} F_{\text{Moon}} &= 93.27209062^\circ + 173952762.8478'' \cdot T \\ &+ 12.7512'' \cdot T^2 + 0.001037'' \cdot T^3 + 0.00000417'' \cdot T^4 , \end{aligned} \quad (\text{G.50})$$

and the angle  $\nu_{\text{Moon}}$  is calculated by comparing the equations (B.9) and (B.12). The argument of perigee of the Sun is calculated from

$$\eta_{\text{Sun}} = \nu_{\text{Sun}} - F_{\text{Moon}} - \Omega_{\text{Moon}} + D , \quad (\text{G.51})$$

with the coefficient

$$\begin{aligned} D &= 297.85019547^\circ + 1602961601.209'' \cdot T \\ &+ 6.3706'' \cdot T^2 + 0.006593'' \cdot T^3 + 0.00003169'' \cdot T^4 . \end{aligned} \quad (\text{G.52})$$

The transformation of (G.46) to the ECEF coordinates is done according to equation (A.1). In this work, nutation and polar motion were neglected. The precession matrix consists of three rotations

$$R_P = R_z(\alpha)R_y(\chi)R_z(\beta) . \quad (\text{G.53})$$

The angles are approximated by

$$\begin{aligned} \alpha &= 2306.2181'' \cdot T + 1.09468'' \cdot T^2 + 0.018203'' \cdot T^3 , \\ \chi &= 2004.3109'' \cdot T - 0.42665'' \cdot T^2 - 0.041833'' \cdot T^3 , \\ \beta &= 2306.2181'' \cdot T + 0.30188'' \cdot T^2 + 0.017998'' \cdot T^3 . \end{aligned} \quad (\text{G.54})$$

The Earth rotation matrix is a rotation around the  $z$ -axis

$$R_S = R_z(\xi) , \tag{G.55}$$

with the angle

$$\begin{aligned} \xi = & 280.46061837^\circ + 360.98564736629^\circ \cdot 36525 \cdot T \\ & + \frac{0.0000387933^\circ}{38710000} \cdot T^4 . \end{aligned} \tag{G.56}$$

## H. BIPM's Circular T

In the following a cutouts of the first section of one of BIPM's Circular T are shown. After the header information, on the left hand side the time laboratories and their locations are given. The next five columns represent the UTC-UTC(k) values. The last three columns are the statistical uncertainty "uA", the systematic uncertainty "uB", and the overall uncertainty "u".

CIRCULAR T 273  
2010 OCTOBER 11, 12h UTC

ISSN 1143-1393

BUREAU INTERNATIONAL DES POIDS ET MESURES  
ORGANISATION INTERGOUVERNEMENTALE DE LA CONVENTION DU METRE  
PAVILLON DE BRETEUIL F-92312 SEVRES CEDEX TEL. +33 1 45 07 70 70 FAX. +33 1 45 34 20 21 tai@bipm.org

1 - Coordinated Universal Time UTC and its local realizations UTC(k). Computed values of [UTC-UTC(k)] and uncertainties valid for the period of this Circular.  
From 2009 January 1, 0h UTC, TAI-UTC = 34 s.

Date 2010	0h UTC	AUG 31	SEP 5	SEP 10	SEP 15	SEP 20	SEP 25	SEP 30	Uncertainty/ns			Notes
MJD		55439	55444	55449	55454	55459	55464	55469	uA	uB	u	
Laboratory k		[UTC-UTC(k)]/ns										
AOS (Borowiec)		10.4	8.0	8.5	8.1	7.6	5.5	2.6	0.5	5.2	5.2	
APL (Laurel)		5.3	-4.9	-	-	-	-8.8	-8.3	1.5	5.2	5.4	
AUS (Sydney)		80.1	95.1	106.8	117.7	118.3	126.4	146.3	0.4	5.1	5.1	
BEV (Wien)		11.7	8.3	12.2	5.0	3.0	-0.1	-0.6	1.5	3.2	3.6	
BIM (Sofiya)		-6594.3	-6583.0	-6576.8	-6564.9	-6558.5	-6542.4	-6540.6	2.0	7.1	7.4	
BIRM (Beijing)		-11355.3	-11396.1	-11437.0	-11482.7	-11526.1	-11563.6	-11601.2	2.0	20.0	20.1	
BY (Minsk)		51.4	54.5	60.6	65.8	-33.7	-29.9	-27.8	2.0	7.1	7.4	(1)
CAO (Cagliari)		-4596.0	-4598.4	-4601.9	-4615.7	-4625.7	-4643.0	-4660.6	1.5	7.1	7.2	
CH (Bern)		13.5	12.0	9.2	9.1	9.0	9.4	7.5	0.6	1.6	1.7	
CNM (Queretaro)		-3.7	4.5	11.7	20.3	18.1	15.0	16.9	2.5	5.1	5.7	
• • •												
PL (Warszawa)		25.7	17.4	18.0	11.3	-5.1	-3.8	-12.6	1.5	5.1	5.3	
PTB (Braunschweig)		2.1	0.9	2.0	1.2	0.5	-0.5	-2.3	0.2	1.2	1.3	
ROA (San Fernando)		-10.9	-6.5	-0.8	3.9	8.4	13.7	17.3	0.6	5.1	5.1	
SCL (Hong Kong)		-5.5	-3.1	-3.4	8.2	4.9	14.5	24.9	3.0	10.1	10.5	
SG (Singapore)		21.3	12.2	5.5	-0.4	9.6	20.9	31.0	0.4	5.2	5.2	
SIQ (Ljubljana)		-189.7	-196.9	-222.1	-256.1	-238.8	-207.0	-231.6	5.0	20.0	20.6	
SMD (Bruxelles)		-2.8	-2.6	3.3	5.8	5.2	7.5	5.7	1.5	19.8	19.8	
SMU (Bratislava)		-188.9	-178.5	-165.8	-157.5	-145.9	-148.2	-139.5	1.5	20.0	20.1	
SP (Boras)		15.6	18.7	20.8	17.1	11.6	5.3	-2.6	0.6	1.6	1.7	
SU (Moskva)		4.5	1.3	2.0	0.4	-0.7	-2.7	-6.2	1.5	5.0	5.3	
• • •												

After the UTC-UTC(k) section information about the offset of GPS and GLONASS with respect to UTC and the steering corrections derived from the primary frequency standards are given.

In the last section of the Circular T, the links, their uncertainties, the type of calibration, and the date of calibration are listed:

The calibration type of the link is indicated as: GPS EC for GPS equipment calibration; TW EC for two-way equipment calibration; LC (technique) for a link calibrated using 'technique'; BC (technique) for a link calibrated using 'technique' to transfer a past equipment calibration through a discontinuity of link operation. DIC is used for direct internal calibration.

• • •

The calibration dates indicate: the most recent calibration results for the two laboratories in the case of EC and the most recent calibration of the link in the case of LC and BC, NA stands for not available, in this case estimated values are provided

Link	Type	uA/ns	uB/ns	Calibration Type	Calibration Dates
AOS /PTB	TWSTFT	0.5	5.0	BC(GPS MC)	2008 May
APL /PTB	GPS MC	1.5	5.0	GPS EC/GPS EC	2003 Dec/2006 Sep
AUS /PTB	GPSPPP	0.3	5.0	LC(GPS MC)	2009 Nov
BEV /PTB	GPS MC	1.5	3.0	BC(TWSTFT)	2008 Jan
BIM /PTB	GPS MC	2.0	7.0	GPS EC/GPS EC	2007 Nov
BIRM/PTB	GPS MC	2.0	20.0	NA /GPS EC	NA /2006 Sep
BY /PTB	GPS MC	2.0	7.0	GPS EC/GPS EC	2008 Jun/2006 Sep
CAO /PTB	GPS MC	1.5	7.0	GPS EC/GPS EC	2004 Nov/2006 Sep
CH /PTB	TWSTFT	0.6	1.0	LC(TWSTFT)/BC(GPS PPP)	2008 Sep/2009 Aug
CNM /PTB	GPS MC	2.5	5.0	BC(GPS SC)	2008 May
CNMP/PTB	GPS MC	3.0	5.0	GPS EC/GPS EC	2004 May/2006 Sep
DLR /PTB	GPSPPP	0.3	5.0	GPS EC/GPS EC	2007 Feb/2004 Aug
DMDM/PTB	GPS MC	2.0	7.0	GPS EC/GPS EC	2007 Jan/2006 Sep
DTAG/PTB	GPSPPP	0.3	10.0	LC(GPS MC)	2009 Jul
EIM /PTB	GPS MC	3.5	5.0	GPS EC/GPS EC	2007 May/2003 Aug
HKO /PTB	GPS MC	2.5	5.0	GPS EC/GPS EC	2004 Sep/2006 Sep
IFAG/PTB	GPSPPP	0.3	5.0	GPS EC/GPS EC	2003 Jun/2004 Aug
IGNA/PTB	NA				
INPL/PTB	NA				
INTI/PTB	GPS MC	4.0	20.0	NA /GPS EC	NA /2006 Sep

# Bibliography

- [1] F. Riehle. *Frequency standards: Basics and Applications*. Wiley-VCH, Weinheim, 2005.
- [2] F. Arias and A. Bauch. *Metrology of Time and Frequency*. Handbook of Metrology, Wiley-VCH, Weinheim, 2010.
- [3] J. Levine. Introduction to time and frequency metrology. *Review of Scientific Instruments*, 70(6):2567–2596, 1999.
- [4] E. D. Kaplan. *Understanding GPS Principles and Applications*. Artech House, Norwood, MA, 1996.
- [5] G. Xu. *GPS Theory, Algorithms and Applications*. Springer, New York, 2003.
- [6] A. Bauch and T. Heindorff. Die SI-Basiseinheit "Sekunde". *PTB-Mitteilungen*, 112:291–298, 2003.
- [7] A. Bauch, P. Hetzel, and D. Piester. Zeit- und Frequenzverbreitung mit DCF77: 1959-2009 und darüber hinaus. *PTB-Mitteilungen*, 119(3):11–34, 2009.
- [8] A. Bauch. Caesium atomic clocks: function, performance and applications. *Measurement Science and Technology*, 14:1159–1173, 2003.
- [9] D. W. Allan. Picosecond Time Difference Measurement System. In *Proc. 29<sup>th</sup> Annu. Symp. on Freq. Contrl.*, pages 404–411, May 1975.
- [10] T. J. Quinn. The BIPM and the accurate measurement of time. *Proceedings of the IEEE*, 79(7):894–905, 1991.
- [11] H. Hellwig, D. W. Allan, S. R. Stein, and K. A. Prichard. Transcontinental and Intercontinental Portable Clock Time Comparisons. *IEEE Transactions on Measurement and Instrumentation*, 27(1):65–68, 1978.
- [12] K. Horiai. Accuracy of time comparison derived from reception of LORAN-C and Global Positioning System time signals. *Radio Science*, 27(5):545–551, 1992.



- [13] Yu. A. Fedorov and S. B. Pushkin. Comparing the national standards of time and frequency of the USSR, Czechoslovakia, and East Germany. *Measurement Techniques*, 22(10):1193–1195, 1979.
- [14] J. Levine. Time and frequency distribution using satellites. *Rep. Prog. Phys.*, 65:1119–1164, 2002.
- [15] J. Kouba and P. Heroux. Precise Point Positioning Using IGS Orbit and Clock Products. *GPS Solutions*, 5(2):12–28, 2002.
- [16] H. Schnatz, O. Terra, K. Predehl, T. Feldmann, T. Legero, B. Lipphardt, U. Sterr, G. Grosche, T. W. Hänsch, R. Holzwarth, T. Udem, Z. Lu, L. Wang, W. Ertmer, J. Friebe, A. Pape, E. M. Rasel, M. Riedmann, and T. Wübbena. Phase-coherent frequency comparison of optical clocks using a telecommunication fiber link. *IEEE Transactions on Ultrasonics, Ferroelectrics, and Frequency Control*, 57(1):175–181, 2010.
- [17] H. Esteban, J. Palacio, F.J. Galindo, T. Feldmann, A. Bauch, and D. Piester. Improved GPS based time link calibration involving ROA and PTB. *IEEE Transactions on Ultrasonics, Ferroelectrics, and Frequency Control*, 57(3):714–720, 2010.
- [18] D. B. Sullivan, D. W. Allan, D. A. Howe, and F. L. Walls. NIST Technical Note 1337, Characterization of Clocks and Oscillators, March 1990, online at [http://www.pfcosc.com/appnotes/Characterization of clocks and oscillators.pdf](http://www.pfcosc.com/appnotes/Characterization_of_clocks_and_oscillators.pdf).
- [19] W. Riley. Handbook of Frequency Stability Analysis, NIST Special Publication 1065, online at [tf.nist.gov/general/pdf/2220.pdf](http://tf.nist.gov/general/pdf/2220.pdf), as of November 2010.
- [20] D. W. Allan. The statistics of Atomic Frequency Standards. *Proc. IEEE*, 45(2):221–230, 1966.
- [21] M. A. Weiss, G. Petit, and Z. Jiang. A comparison of GPS common-view time transfer to all-in-view. In *Proc. Joint IEEE Intl. Freq. Control Symposium and PTTI Systems and Applications Meeting*, pages 324–328, Vancouver, Canada, August 2005.
- [22] T. Gotoh. Improvement GPS Time Links in Asia with All in View. In *Proc. Joint IEEE Intl. Freq. Control Symposium and PTTI Systems and Applications Meeting*, pages 707–711, Vancouver, Canada, August 2005.
- [23] M. Rost, A. Bauch, J. Becker, T. Feldmann, D. Piester, T. Polewka, D. Sibold, and E. Staliuniene. PTB’s Time and Frequency Activities in 2008 and 2009.

- In *Proc. 41<sup>th</sup> PTTI Systems and Applications Meeting*, pages 197–213, Santa Ana Pueblo, New Mexico, USA, November 16-19 2009.
- [24] D. Piester, M. Fujieda, M. Rost, and A. Bauch. Time Transfer Through Optical Fibers (TTTOF): First Results of Calibrated Clock Comparison. In *Proc. 41<sup>th</sup> PTTI Systems and Applications Meeting*, pages 89–99, Santa Ana Pueblo, New Mexico, USA, November 16-19 2009.
- [25] Global Positioning System Standard Positioning Service Signal Specification, 2nd Edition, June 1995, online at <http://www.pnt.gov/public/docs/1995/signalspec1995.pdf>.
- [26] R. J. Meinhold and N. D. Singpurwalla. Understanding the Kalman Filter. *The American Statistician*, 37(2):123–127, 1983.
- [27] P. Defraigne, P. Uhrich, G. Petit, and W. Aerts. Requirements on GNSS receivers from the perspective of timing applications. In *Proc. EFTF*, Noordwijk, NL, April 13-16 2010.
- [28] J. Levine. Time transfer using multi-channel GPS receivers. *IEEE Transactions on Ultrasonics, Ferroelectrics, and Frequency Control*, 46(2):392–398, 1999.
- [29] D. W. Allan and C. Thomas. Technical Directives for Standardization of GPS Time Receiver Software. *Metrologia*, 31:69–79, 1994.
- [30] W. Gurtner. RINEX The Receiver Independent Exchange Format, Version 2.10. Astronomical Institute University of Berne, 2010.
- [31] P. Defraigne and G. Petit. Time transfer to TAI using geodetic receivers. *Metrologia*, 40:184–188, 2003.
- [32] J. Saastamoinen. Atmospheric corrections for the troposphere and stratosphere in radio ranging. *Geophysical Monograph*, 15:247–251, 1972.
- [33] H. S. Hopfield. Improvements in the tropospheric refraction for range measurements. *Phil. Trans. R. Soc.*, 194:341–352, 1979.
- [34] ASEN 5090 Error Models  
[http://www.colorado.edu/ASEN/asen5090/assignments/ASEN5090\\_ErrorProject2010.pdf](http://www.colorado.edu/ASEN/asen5090/assignments/ASEN5090_ErrorProject2010.pdf).
- [35] W. Lewandowski, J. Azoubib, A. G. Gevorkyan, P. P. Bogdanov, W. J. Klepanski, M. Miranian, J. Danaher, N. B. Koshelyaevsky, and D. W. Allan. A Contribution to the Standardization of GPS and GLONASS Time Transfers. In *Proc. 28<sup>th</sup> PTTI Systems and Applications Meeting*, pages 367–386, Reston, VA, USA, December 03-05 1996.

- [36] S. Pireaux, P. Defraigne, L. Wauters, N. Bergeot, Q. Baire, and C. Bruyninx. Higher-order ionospheric effects in GPS time and frequency transfer. *GPS Solutions*, 14:267–277, 2010.
- [37] P. Panek. private communication.
- [38] N. Ashby. Relativity in the Global Positioning System. *Living Reviews in Relativity*, 6(1), 2003.
- [39] M. A. Lombardi and A. N. Novick. Effects of the rooftop environment on GPS time transfer. In *Proc. 38<sup>th</sup> PTTI Systems and Applications Meeting*, pages 449–466, Reston, VA, USA, December 07-09 2006.
- [40] A. J. van Dierendonck, P. Fenton, and T. Ford. Theory and Performance of Narrow Correlator Spacing in a GPS Receiver. *Navigation*, 39(3):265–283, 1992.
- [41] N. Penna, M. Bos, T. Baker, and H.-G. Scherneck. Assessing the accuracy of predicted ocean tide loading displacement values. *Journal of Geodesy*, 82:893–907, 2008.
- [42] R. D. Ray. A global ocean tide model from topex/poseidon altimetry: Got99.2. *NASA Technical Memorandum*, 209478, 1999.
- [43] <http://www.oso.chalmers.se/~loading>.
- [44] R. Píríz, G. Cerretto, A. Perrucca, and P. Tavella. Evaluation of the Time and Frequency Transfer Capabilities of a Network of GNSS Receivers located in Timing Laboratories. In *Proc. 41<sup>th</sup> PTTI Systems and Applications Meeting*, pages 559–574, Santa Ana Pueblo, New Mexico, USA, November 16-19 2009.
- [45] G. Beutler, M. Rothacher, S. Schaer, T. A. Springer, J. Kouba, and R. E. Neilan. The International GPS Service (IGS): An interdisciplinary service in support of Earth sciences. *Advances in Space Research*, 23(4):631 – 653, 1999.
- [46] <http://igs.cb.jpl.nasa.gov/network/netindex.html>.
- [47] J. Kouba. A Guide to using International GNSS Service (IGS) Products, online at <http://igs.cb.jpl.nasa.gov/components/usage.html>, as of May 2009.
- [48] <http://igs.cb.jpl.nasa.gov/organization/centers.html>.
- [49] <http://igs.cb.jpl.nasa.gov/components/formats.html>.
- [50] J. Ray and K. Senior. Geodetic techniques for time and frequency comparisons using GPS phase and code measurements. *Metrologia*, 42:215–232, 2005.

- [51] W. Lewandowski, D. Matsakis, G. Panfilo, and P. Tavella. The evaluation of uncertainties in [UTC-UTC(k)]. *Metrologia*, 43:278–286, 2006.
- [52] W. Lewandowski and Z. Jiang. Use of GLONASS at the BIPM. In *Proc. 41<sup>th</sup> PTTI Systems and Applications Meeting*, pages 197–213, Santa Ana Pueblo, New Mexico, USA, November 16-19 2009.
- [53] Z. Jiang and G. Petit. Combination of TWSTFT and GNSS for accurate UTC time transfer. *Metrologia*, 46:305–314, 2009.
- [54] G. Panfilo and E. Arias. Algorithms for International Atomic Time. *IEEE Transactions on Ultrasonics, Ferroelectrics, and Frequency Control*, 57(1):140–150, 2010.
- [55] C. Thomas and J. Azoubib. TAI computation: study of an alternative choice for implementing an upper limit of clock weights. *Metrologia*, 33:227–240, 1996.
- [56] D. Piester, A. Bauch, L. Breakiron, D. Matsakis, B. Blanzano, and O. Koudelka. Time transfer with nanosecond accuracy for the realization of International Atomic Time. *Metrologia*, 45(2):185–198, 2008.
- [57] W. Lewandowski and L. Tisserand. Relative characterization of GPS time equipment delays at the OP, PTB, AOS, USNO and IT, online at <http://www.bipm.org/utis/common/pdf/rapportBIPM/2010/03.pdf>, March 2010.
- [58] Vremya-Ch. Passive Hydrogen Maser Frequency and Time Standard VCH-1006 Maintenance and service manual.
- [59] Dicom. GTR50 Time & Frequency Transfer Receiver, Operating Instructions.
- [60] P. Panek and I. Prochazka. Time interval measurement device based on surface acoustic wave filter excitation, providing 1 ps precision and stability. *Review of Scientific Instruments*, 78(094701), 2007.
- [61] J. Friebe, A. Pape, M. Riedmann, K. Moldenhauer, T. Mehlstäubler, N. Reibin, C. Lisdat, E. M. Rasel, W. Ertmer, H. Schnatz, B. Lipphardt, and G. Grosche. Absolute frequency measurement of the magnesium intercombination transition  $^1S_0 \rightarrow ^3P_1$ . *Phys. Rev. A*, 78(3):033830, September 2008.
- [62] S. Diddams. Optical frequency combs: Introduction, sources and applications. In *Frequency Control Symposium, 2009 Joint with the 22nd European Frequency and Time forum. IEEE International*, page xv, April 2009.

- [63] T. Gotoh, M. Fujieda, and J. Amagai. Comparison Study of GPS Carrier Phase and Two-Way Satellite Time and Frequency Transfer. In *Frequency Control Symposium, 2007 Joint with the 21st European Frequency and Time Forum. IEEE International*, pages 1188–1193, Geneva, Switzerland, May 29 - June 1 2007.
- [64] G. Petit. The TAIPPP pilot experiment. In *Proc. EFTF - IEEE IFCS Joint Conference*, pages 116–119, Besançon, France, April 20-24 2009.
- [65] T. Feldmann, D. Piester, A. Bauch, and T. Gotoh. GPS carrier phase time and frequency transfer with different versions of precise point positioning software. In *Proc. 40<sup>th</sup> PTTI Systems and Applications Meeting*, pages 403–414, Reston, VA, USA, December 01-04 2008.
- [66] T. Feldmann, D. Piester, H. Esteban, J. Palacio, F. J. Galindo, T. Gotoh, H. Maeno, U. Weinbach, and S. Schön. GPS carrier phase and precise point positioning timescale comparisons using different software packages. In *Proc. EFTF - IEEE IFCS Joint Conference*, pages 120–125, Besançon, France, April 20-24, 2009.
- [67] R. Dach, U. Hugentobler, T. Schildknecht, L.-G. Bernier, and G. Dudle. Precise continuous time and frequency transfer using GPS carrier phases. In *Proc. Joint IEEE Intl. Freq. Control Symposium and PTTI Systems and Applications Meeting*, pages 329–336, Vancouver, Canada, August 2005.
- [68] T. Gotoh, T. Hobiger, R. Ichikawa, T. Feldmann, and D. Piester. Application of ray-traced troposphere delays to GPS time transfer. In *Proc. 52nd Meeting of the Japan Society for Aeronautical and Space Sciences*, pages 1322–1326, Hyogo, Japan, November 05-07 2008.
- [69] F. Lahaye. private communication.
- [70] F. Webb and J. Zumberge. An introduction to GIPSY/OASIS-II, Precision Software for the Analysis of Data from the Global Positioning System, Jet Propulsion Laboratory, Pasadena, CA, JPL D-11088, July 1997.
- [71] R. Dach, U. Hugentobler, P. Fridez, and M. Meindl. Bernese GPS Software Version 5.0, <http://www.bernese.unibe.ch/docs/D0CU50.pdf>.
- [72] U. Weinbach and S. Schön. On the Correlation of Tropospheric Zenith Path Delay and Station Clock Estimates in Geodetic GNSS Frequency Transfer. In *Proc. EFTF*, Noordwijk, NL, April 13-16 2010.
- [73] U. Weinbach and S. Schön. Stability analysis of the hardware delays of geodetic GPS receivers for clock comparisons. In *2ndnd International Colloquium -*

- Scientific and Fundamental Aspects of the Galileo Programme*, Padova, Italy, October 14-16 2010.
- [74] H. Esteban, J. Palacio, F.J. Galindo, and J. Garate. GPS receiver performance test at ROA. In *Proc. 40<sup>th</sup> PTTI Systems and Applications Meeting*, pages 403–414, Reston, VA, USA, December 01-04 2008.
- [75] T. Feldmann, A. Bauch, D. Piester, A. Stefanov, L.-G. Bernier, C. Schlunegger, and K. Liang. On improved GPS based link calibration of the time links between METAS and PTB. In *Proc. EFTF*, Noordwijk, NL, April 13-16 2010.
- [76] G. Petit and Z. Jiang. GPS All in View time transfer for TAI computation. *Metrologia*, 45(1):35–45, 2008.
- [77] G. Wübbena, M. Schmitz, G. Boettcher, and C. Schumann. Absolute GNSS antenna calibration with a robot: repeatability of phase variations, calibration of GLONASS and determination of carrier-to-noise pattern. In *IGS 2006 Workshop Proceedings, IGS Central Bureau*, 2008.
- [78] Stanford Research Systems (SRS). SR620 Operating Manual and Programming Reference.
- [79] W. Lewandowski and C. Thomas. GPS Time transfer. *Proceedings of the IEEE*, 79(7):991–1000, 1991.
- [80] I. Prochazka and P. Panek. Nonlinear effects in the time measurement device based on surface acoustic wave filter excitation. *Review of Scientific Instruments*, 80(7):076102–076102–3, July 2009.
- [81] J. R. Ray and K. Senior. Temperature Sensitivity of Timing Measurements Using Dorne Margolin Antennas. *GPS Solutions*, 5:24–30, 2001.
- [82] D. Matsakis, K. Senior, and P. Cook. Comparison of continuously filtered GPS carrier-phase time and frequency transfer with independent daily GPS carrier-phase solutions and with two-way satellite time transfer. In *Proc. 33<sup>th</sup> PTTI Systems and Applications Meeting*, pages 63–88, Long Beach, CA, USA, November 27-29 2001.
- [83] G. Petit, C. Thomas, Z. Jiang, P. Urich, and F. Taris. Use of GPS ASHTECH Z12T receivers for accurate time and frequency comparisons. *IEEE Transactions on Ultrasonics, Ferroelectrics, and Frequency Control*, 46(4):941–949, 1999.
- [84] [http://www.bipm.org/utils/common/TimeCalibrations/GPS\\_P3/P3\\_calib\\_PTB.pdf](http://www.bipm.org/utils/common/TimeCalibrations/GPS_P3/P3_calib_PTB.pdf).

- [85] [http://www.bipm.org/utils/common/TimeCalibrations/GPS\\_P3/P3\\_calib\\_CH.pdf](http://www.bipm.org/utils/common/TimeCalibrations/GPS_P3/P3_calib_CH.pdf).
- [86] J. Plumb, K. M. Larson, J. White, and E. Powers. Absolute calibration of a geodetic time transfer system. *IEEE Transactions on Ultrasonics, Ferroelectrics, and Frequency Control*, 52(11):1904–1911, 2005.
- [87] A. Bauch, D. Piester, P. Whibberley, B. Blanzano, O. Koudelka, J. Achkar, D. Rovera, E. Kroon, E. Dierikx, L. Lorini, F. Cordara, and C. Schlunegger. Results of the 2008 TWSTFT calibration of seven european stations. In *Frequency Control Symposium, 2009 Joint with the 22nd European Frequency and Time forum. IEEE International*, pages 1209–1215, april 2009.
- [88] R. Stecher. *Messung von Zeit und Frequenz*. Verlag Technik, Berlin, 1990.
- [89] D. Piester, T. Feldmann, A. Bauch, M. Fujieda, and T. Gotoh. Concept for an Accurate Calibration of Long Baseline Two-Way Satellite Time and Frequency Transfer (TWSTFT) Links via Two Separated Transponders on One Telecommunication Satellite. In *Proc. EFTF - IEEE IFCS Joint Conference*, pages 1076–1081, Besançon, France, April 20-24, 2009.
- [90] Evaluation of measurement data - Guide to the expression of uncertainty in measurement, 2008, online at [http://www.bipm.org/utils/common/documents/jcgm/JCGM\\_100\\_2008\\_E.pdf](http://www.bipm.org/utils/common/documents/jcgm/JCGM_100_2008_E.pdf).
- [91] B. Pesch. *Bestimmung der Messunsicherheit nach GUM*. Books on Demand, Alamogordo, New Mexico, USA, 2003.
- [92] IERS Conventions Centre, <http://tai.bipm.org/iers/>.
- [93] C. Boucher and Z. Altamimi. ITRS, PZ-90 and WGS 84: current realizations and the related transformation parameters. *Journal of Geodesy*, 75:613–619, 2001.
- [94] N. Ashby. The Sagnac Effect in the Global Positioning System, online at <http://digilander.libero.it/solciclos/>, as of October 2010.





# Acknowledgements

Primarily I wish to thank Ekkehard Peik (PTB) for supervising this work, and Andreas Bauch (PTB) and Steffen Schön (IfE) for giving me the opportunity to work in the field of time and frequency. All three are thanked for valuable suggestions related to the present work. I am also grateful to my other colleagues in the time and frequency department at PTB for their support and the good working atmosphere, namely Dirk Piester, Michael Rost, Jürgen Becker, Thomas Polewka, and Egle Staliuniene. Special thanks go to Thomas Leder and Hans-Albert Kremling for their help in constructing the mobile frequency reference, and to Christof Richter and Sven Krenauer for help in constructing the calibration set-up.

André Stefanov (METAS), Laurent-Guy Bernier (METAS), Christian Schlunegger (METAS), Héctor Esteban (ROA), Liang Kun (NIM), and Demetrios Matsakis (USNO) and his team are acknowledged for their cooperation in the field of international time link calibrations. I also wish to thank Temmo Wübbena (IQO), Ulrich Weinbach (IfE), and Tadahiro Gotoh (NICT) for their cooperation and for providing equipment on loan.

I would like to thank Petr Panek and Alex Kuna from UFE for collaboration in case of initial problems with the GTR50s and for continuously updating the firmware.

I am grateful to Harald Schnatz (PTB) and his team in the length department for supporting the use of the optical fiber between PTB and IQO.

This work was supported by the Centre for Quantum Engineering and Space-Time Research (QUEST), Leibniz Universität Hannover.



# Curriculum Vitae

Name: Thorsten Feldmann  
Date of birth: 11th July 1977  
Place of birth: Duisburg, Germany

1984 – 1988 Städt. Grundschule Hebbelstraße in Duisburg

1988 – 1998 Steinbart-Gymnasium in Duisburg  
School leaving certificate: Abitur

1998 – 1999 Mandatory military service

1999 – 2005 Universität Duisburg-Essen  
University degree: Diplom-Physiker

Nov. 2007 – Research assistant at the Physikalisch-Technische Bundesanstalt in Braunschweig



# Publications

- T. Feldmann, D. Piester, A. Bauch, and T. Gotoh. GPS carrier phase time and frequency transfer with different versions of precise point positioning software. In *Proceedings of the 40<sup>th</sup> PTTI Systems and Applications Meeting*, pages 403-414, Reston, VA, USA, December 01-04, 2008.
- T. Gotoh, T. Hobiger, R. Ichikawa, T. Feldmann, and D. Piester. Application of ray-traced troposphere delays to GPS time transfer. In *Proceedings of the 52<sup>nd</sup> Meeting of the Japan Society for Aeronautical and Space Sciences*, pages 1322-1326, Hyogo, Japan, November 05-07, 2008.
- T. Feldmann, D. Piester, H. Esteban, J. Palacio, F. J. Galindo, T. Gotoh, H. Maeno, U. Weinbach, and S. Schön. GPS carrier phase and precise point positioning timescale comparisons using different software packages. In *Proceedings of the EFTF - IEEE IFCS Joint Conference*, pages 120-125, Besançon, France, April 20-24, 2009.
- U. Weinbach, S. Schön, and T. Feldmann. Evaluation of state-of-the-art geodetic GPS receivers for frequency comparisons. In *Proceedings of the EFTF - IEEE IFCS Joint Conference*, pages 263-268, Besançon, France, April 20-24, 2009.
- H. Esteban, J. Palacio, F.J. Galindo, T. Feldmann, A. Bauch, and D. Piester. A GPS calibration trip experience between ROA and PTB. In *Proceedings of the EFTF - IEEE IFCS Joint Conference*, pages 274-279, Besançon, France, April 20-24, 2009.
- H. Schnatz, O. Terra, K. Predehl, T. Feldmann, T. Legero, B. Lipphardt, U. Sterr, G. Grosche, T. W. Hänsch, R. Holzwarth, T. Udem, Z. Lu, L. Wang, W. Ertmer, J. Friebe, A. Pape, E. M. Rasel, M. Riedmann, and T. Wübbena. Phase-coherent frequency comparison of optical clocks using a telecommunication fiber link. In *Proceedings of the EFTF - IEEE IFCS Joint Conference*, pages 807-812, Besançon, France, April 20-24, 2009.
- D. Piester, T. Feldmann, A. Bauch, M. Fujieda, and T. Gotoh. Concept for an Accurate Calibration of Long Baseline Two-Way Satellite Time and Frequency Transfer (TWSTFT) Links via Two Separated Transponders on

One Telecommunication Satellite. In *Proceedings of the EFTF - IEEE IFCS Joint Conference*, pages 1076-1081, Besançon, France, April 20-24, 2009.

- T. Feldmann, A. Bauch, and D. Piester. GPS Carrier-Phase Time and Frequency Comparisons: Applications and Uncertainty Estimation. In *Proceedings of the 2<sup>nd</sup> International Colloquium - Scientific and Fundamental Aspects of the Galileo Programme*, Padova, Italy, October 14-16, 2009.
- M. Rost, A. Bauch, J. Becker, T. Feldmann, D. Piester, T. Polewka, D. Sibold, and E. Staliuniene. PTB's Time and Frequency Activities in 2008 and 2009. In *Proceedings of the 41<sup>th</sup> PTTI Systems and Applications Meeting*, pages 197-213, Santa Ana Pueblo, New Mexico, USA, November 16-19, 2009.
- T. Feldmann, A. Bauch, D. Piester, A. Stefanov, L.-G. Bernier, C. Schlunegger, and K. Liang. On improved GPS based link calibration of the time links between METAS and PTB. In *Proceedings of the EFTF*, Noordwijk, NL, April 13-16, 2010.
- K. Liang, T. Feldmann, A. Bauch, D. Piester, A. Zhang, and X. Gao. Performance evaluation of NIM GPS receivers in use for time transfer with PTB. In *Proceedings of the EFTF*, Noordwijk, NL, April 13-16, 2010.
- H. Schnatz, O. Terra, K. Predehl, T. Feldmann, T. Legero, B. Lipphardt, U. Sterr, G. Grosche, T. W. Hänsch, R. Holzwarth, T. Udem, Z. Lu, L. Wang, W. Ertmer, J. Friebe, A. Pape, E. M. Rasel, M. Riedmann, and T. Wübbena. Phase-coherent frequency comparison of optical clocks using a telecommunication fiber link. *IEEE Transactions on Ultrasonics, Ferroelectrics, and Frequency Control*, 57(1):175-181, 2010.
- H. Esteban, J. Palacio, F.J. Galindo, T. Feldmann, A. Bauch, and D. Piester. Improved GPS based time link calibration involving ROA and PTB. *IEEE Transactions on Ultrasonics, Ferroelectrics, and Frequency Control*, 57(3):714-720, 2010.
- T. Feldmann, A. Bauch, D. Piester, M. Rost, E. Goldberg, S. Mitchell, and B. Fonville. Advanced GPS Based Time Link Calibration with PTB's New Calibration Set-Up. To be published in *Proceedings of the 42<sup>th</sup> PTTI Systems and Applications Meeting*, Reston, VA, USA, 2010.
- D. Piester, M. Rost, M. Fujieda, T. Feldmann, and A. Bauch. Remote atomic clock synchronization via satellites and optical fibers. *Advances in Radio Science*, 9:1-7, 2011.